Universidade de São Paulo
Instituto de Física

Explorando o diagrama de fase do Plasma de Quarks e Glúons com flutuações no número líquido de prótons no Beam Energy Scan

Renan Nobuyuki Hirayama

Orientadora: Profa. Dra. Frédérique M. B. S. Grassi

Dissertação de mestrado apresentada ao Instituto de Física da Universidade de São Paulo, como requisito parcial para a obtenção do título de Mestre(a) em Ciências.

Banca Examinadora:
Profa. Dra. Frédérique Grassi - Supervisora (IF-USP)
Profa. Dra. Jacquelyn Noronha-Hostler (UIUC)
Prof. Dr. Wei-Liang Qian (EEL-USP)

São Paulo
2021

14/04/21
F. Grassi

FICHA CATALOGRÁFICA
Preparada pelo Serviço de Biblioteca e Informação
do Instituto de Física da Universidade de São Paulo

Hirayama, Renan Nobuyuki

Explorando o diagrama de fase do plasma de quarks e glúons com flutuações no número líquido de prótons no Beam Energy Scan. São Paulo, 2021.

Dissertação (Mestrado) – Universidade de São Paulo, Instituto de Física, Depto. de Física Matemática.

Orientador: Profa. Dra. Frédérique Marie-Brigitte Sylvie Grassi

Área de Concentração: Física de Alta Energia

Unitermos: 1. Colisões de íons pesados relativísticos; 2. Hidrodinâmica; 3. Física de Alta Energia.

USP/IF/SBI-018/2021

University of São Paulo
Physics Institute

Exploring the phase diagram of the Quark-Gluon Plasma with fluctuations on the net amount of protons on the Beam Energy Scan

Renan Nobuyuki Hirayama

Supervisor: Prof. Dr. Frédérique M. B. S. Grassi

Dissertation submitted to the Physics Institute of the University of São Paulo in partial fulfillment of the requirements for the degree of Master of Science.

Examining Committee:

Prof. Dr. Frédérique Grassi - Supervisor (IF-USP)

Prof. Dr. Jacquelyn Noronha-Hostler (UIUC)

Prof. Dr. Wei-Liang Qian (EEL-USP)

São Paulo

2021

Acknowledgments

The opportunity of a M.Sc. education is a privilege, and I would not be where I am if it wasn't for the daily sacrifice of my mother, Andrea Góes de Almeida; I will be eternally grateful for her love, patience and support. I am also very thankful for the wise teachings of my grandmother, Eveli Góes de Almeida, the first of which was basic multiplication, and the last one so far was to never stop enjoying my youth. Moreover, thanks to all my family in Sorocaba, who helped me both morally and financially in times of need.

This work would not have been possible without the aid of my supervisor, Dr. Frédérique Grassi, whose knowledge and dedication taught me more than she knows; her kind-hearted words set much of my academic views. I am very grateful to Dr. Jean-Yves Ollitrault for our conversations which were the basis of this thesis. Thanks to Dr. Fernando Gardim, for the life advices and discussions about the NeXSPheRIO code. Thanks to Dr. Marina Nielsen and Dr. Fernando Navarra, for the amusing conversations and all of the wine.

I acknowledge the support of the secretaries at DFMA, the CPG-IFUSP personnel and the HPC resources made available by STI-USP, and managed by Dr. Francisco Ribacionka.

Science cannot be done alone, and I appreciate the general support provided by my esteemed research group: thanks to Dr. André Veiga Giannini for his incredible memory for bibliography; to Dr. José Carlos Jiménez Apaza for the very helpful comments about the state-of-art physics at low temperatures; to PhD candidate Pedro Ishida for his thorough knowledge about NeXSPheRIO and programming, and for the discussions about pre-hydro yields; to PhD candidate Leonardo Barbosa for his insightful comments on NeXSPheRIO and the phase diagram, and of course all the memes. I also thank Alexandra Elbakyan for the accessibility.

Finally, I thank all the friends that helped, supported and cared for me throughout the years. In particular, I hold dearest André Fellipe Vieira dos Santos, Isabella Danhoni, Luiz Vinícius de Moraes Furtado, Gabriel Nogueira Teixeira and Leandro Souza Nowacki; but I extend my deep gratitude and to the members of BPM, Appa Hip-Hip, TdP, Gartic?, IFurmigueiro, Wiladores, Grupo Certo, Elite Secreta do Açaí and Aerobonde. Each and every one of them was important for my personal and academic growth.

I acknowledge FAPESP for the financial support of this work and the thematic project I am a part of, and also INCT-FNA for its importance to the field of nuclear physics in Brazil. Grant #2018/14479-0, São Paulo Research Foundation (FAPESP).

The journey so far has been hard, but bright, and there is still a long road ahead.

Abstract

This work consists in the development and study of a new method to compute cumulants of conserved quantities in heavy-ion collision simulations. Such cumulants are sensitive to the presence of the Critical End Point (CP) of Quantum Chromodynamics (QCD), and therefore serve as key observables in the ongoing attempt to experimentally scan the QCD phase diagram and locate the CP, in experiments as the *Beam Energy Scan*, in event-by-event analysis which require a large statistic. The significant computational cost of 3+1 dimensional hydrodynamical simulations hinders the obtaining of such statistics in a reasonable time, being one of the reasons for the low amount or nonexistence of publications on these cumulants that use full hydrodynamics. The data-driven method developed in this work has the objective of circumventing this problem, diminishing the number of events needed for a good precision. To do so, the NeXSPheRIO code is used, and preliminary results are compared to data from STAR, with the higher-order cumulants showing promise.

Keywods: Quark-gluon plasma; Critical Point; Relativistic hydrodynamics; Heavy-ion collisions; Fluctuations of conserved charges;

Resumo

Este trabalho consiste na elaboração e estudo de um novo método para o cálculo de cumulantes de quantidades conservadas em simulações hidrodinâmicas de colisões de íons pesados. Tais cumulantes são sensíveis à presença do ponto crítico (CP) da cromodinâmica quântica (QCD), e portanto servem como observáveis cruciais no esforço atual de escanear o diagrama de fases da QCD experimentalmente e localizar o CP, em experimentos como o *Beam Energy Scan*, em análises evento-por-evento, que necessitam de muita estatística. O grande custo computacional de simulações em hidrodinâmica em 3+1 dimensões obstrui a obtenção de tal estatística em um tempo razoável, sendo um dos motivos para a pouca ou não-existência de publicações sobre esses cumulantes que usem hidrodinâmica completa. O método desenvolvido neste trabalho tem como objetivo contornar este problema, diminuindo o número de eventos necessários para uma boa precisão. Para tal, o código NeXSPheRIO é usado, e resultados preliminares são comparados com dados de STAR, com os cumulantes de ordem alta se mostrando promissores.

Palavras-chave: Plasma de quarks e glúons; Ponto crítico; Hidrodinâmica relativística; Colisões de íons pesados; Flutuações de cargas conservadas;

Summary

1. The search for the QCD Critical Point **6**
- 1.1 Heavy-Ion Collisions . . . 7
- 1.2 The Phase Diagram . . . 9
  - 1.2.1 The Critical End-Point . . . 11
- 1.3 Outline . . . 15

2. Theoretical Ingredients **16**
- 2.1 Initial Conditions . . . 16
  - 2.1.1 The NeXus model . . . 17
  - 2.1.2 Initial profiles . . . 19
- 2.2 Hydrodynamic Evolution . . . 20
  - 2.2.1 Equations of Motion . . . 21
  - 2.2.2 Equation of State . . . 22
- 2.3 Freeze-out . . . 26
  - 2.3.1 The Cooper-Frye prescription . . . 27

3. NeXSPheRIO **30**
- 3.1 Code structure . . . 30
- 3.2 Initialization . . . 33
- 3.3 Smoothed hydrodynamics . . . 33
  - 3.3.1 Equations of Motion . . . 36
  - 3.3.2 Cooper-Frye in SPH . . . 37
- 3.4 Decays . . . 38

4. Cumulants in Hydro **39**
- 4.1 Cumulants . . . 39
- 4.2 The problem . . . 41
- 4.3 The workaround . . . 42
  - 4.3.1 An example . . . 43
  - 4.3.2 Number of Freeze-Outs . . . 44
  - 4.3.3 Effect of decays . . . 45
  - 4.3.4 Acceptance cuts . . . 46
- 4.4 Some remarks . . . 48

5. Results for STAR cumulants **49**
- 5.1 Calibration . . . 49
  - 5.1.1 Centrality selection . . . 50
  - 5.1.2 Energy loss correction . . . 52
  - 5.1.3 Freeze-out Temperature . . . 53

5.2 Proton number 55
5.2.1 Rescaling 58
5.3 Net-charge 61
6. Discussion **62**
A. Statistical Mechanics **63**
A.1 Equations of State 63
A.1.1 Hadron Resonance Gas 65
A.1.2 MIT Bag Model 66
A.2 From χ_n to C_n 67
B. Relativistic Hydrodynamics **69**
B.1 Ideal equations of motion 69
B.2 The Action principle 72
B.2.1 Minimization 73

Chapter 1

The search for the QCD Critical Point

Physicists have been trying to answer childlike questions such as *"What was there at the beginning of the Universe?"* and *"What will I see if I look at this very, very closely?"* for a long time. Although conceptually simple, these are questions about observations inaccessible in the usual human experience. An attempt to answer them lies in the theory called Quantum Chromodynamics (QCD), the description of strong interactions between *quarks and gluons*, the basic constituents of composite hadrons such as protons, neutrons and pions [1]. At extremely high temperatures ($\sim 10^{12}$ K), QCD is necessary to describe the hot and dense matter formed instants after the Big Bang, at the early stages of the Universe.

The theory receives its name from the *color charge* carried by the quarks and gluons, as an allusion of there being three types of charge[1], unlike the electric charge, which has only positives and negatives of a single type of charge. QCD is a non-abelian gauge theory, making it a very complicated theory in which gluons – the gauge bosons – are not neutral and can interact with each other [2].

One main property of QCD is the *color confinement*, the idea that only "white" (that is, color-neutral) particles are observable. At ordinary thermodynamical conditions these are the baryons, composed of three (valence) quarks, and the mesons, composed of a quark-antiquark pair. Although the mechanisms are not completely understood,

[1] Conventionally named "red", "green" and "blue", with the negatives "cyan", "magenta"‘ and "yellow", respectively.

the confinement is well established by experiment, and what happens is generally agreed upon: as quarks separate, the gluon field between them forms color flux tubes, which eventually break apart creating the colorless hadrons [3, 4].

Another remarkable property exhibited by QCD is the *asymptotic freedom*, which states that as the energy scale increases, the intensity of interactions between color charges decrease. This was discovered and proven by the 2004 Nobel Prize winners Gross, Wilczek [5] and Politzer [6]. A logical consequence of these two properties is that ordinary matter suffers transition into a new phase at high enough energy densities, when quarks and gluons are liberated and become the relevant degrees of freedom. This new phase is the so-called *Quark-Gluon Plasma* (QGP).

1.1 Heavy-Ion Collisions

The task of studying the QGP is a great experimental effort, and the systematic way to do so is in experiments of *heavy-ion collisions* (HIC), where beams of heavy nuclei are accelerated to relativistic velocities towards another beam or a fixed target, in facilities such as RHIC-BNL, in the USA; FAIR, under construction in Germany; LHC, in the EU; and (in the future) J-PARC, in Japan.

The high complexity of QCD hinders attempts at analytical solutions, and so far there is no single formalism capable of fully describing the process of a HIC [4]. Then, the collision is modularized in stages, each described separately by phenomenology or first-principle calculations. Fig. 1.1 depicts the usual stages of the HIC.

Before the collision, the nuclei are highly Lorentz-contracted, with the shape of thin disks in the center-of-mass frame. At top RHIC values, the energy in the center of mass of two nucleons is $\sqrt{s_{NN}} = 200$ GeV, corresponding to a Lorentz factor of $\gamma \approx 100$, so each nucleus is effectively a "pancake" with thickness equal to 1% of the diameter [8]. Then, right as they collide at $\tau = 0$, all of the energy is concentrated in a small volume of approximately the size of two nuclei; a rough estimate of the energy density, using gold nuclei overlapping perfectly (Au, mass number $A = 197$), peaks[2] at $\epsilon \sim 3000$ GeV/fm^3, far exceeding that of a typical hadron, $\epsilon \sim 0.5$ GeV/fm^3 [9].

Such high energy density makes the interactions between quarks and gluons weak,

[2]The total energy is $E = 200A$ GeV, and the volume occupied by two gold nuclei in this frame is $V = \frac{4\pi}{3}\frac{R}{100}R^2$, with radius $R = 1.2A^{1/3} \sim 7$ fm.

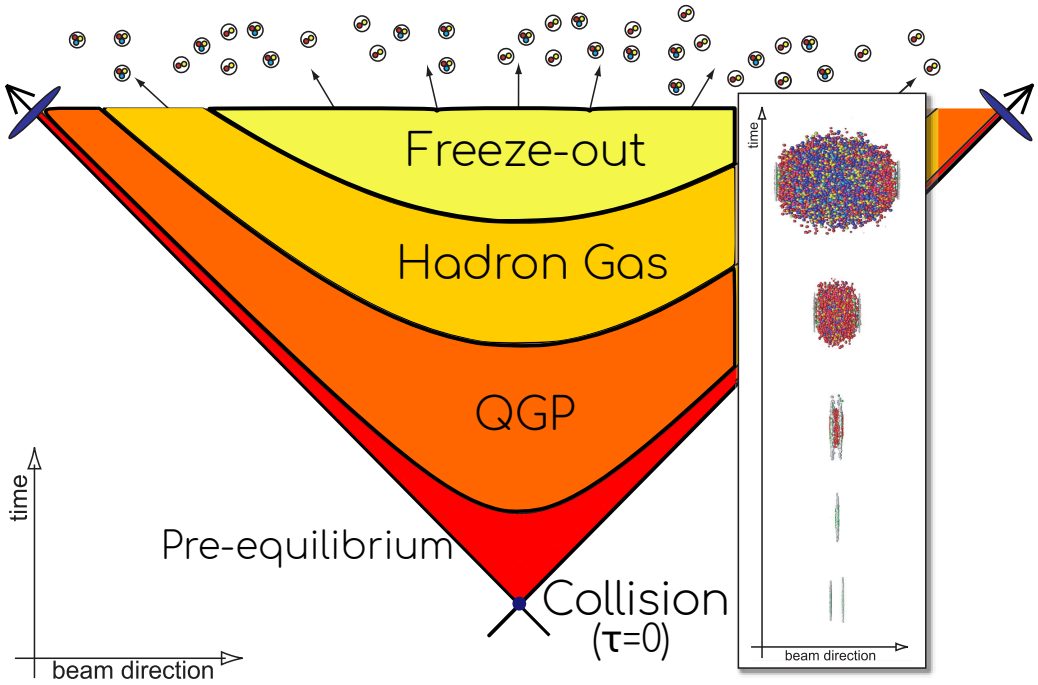

Figure 1.1: Schematic spacetime diagram of a HIC, from the collision vertex at $\tau = 0$ until freeze-out. The inset depicts the longitudinal evolution of two nuclei colliding head-on. Adapted from [7].

due to asymptotic freedom, to the point where the coupling is small enough to apply perturbative QCD (pQCD). In hard scatterings – interactions with a large momentum exchange –, phenomena like jets of particles can be computed with pQCD. In fact, an experimental confirmation of QCD and the discovery of gluons came from detection of three-jet events [10].

However, the nuclei are not homogeneous solid spheres. The QCD fields fluctuate inside the nucleons, so right after the collision the system is far from local thermal equilibrium and the distributions of energy is not smooth, which makes this stage very difficult to describe. Some attempts use the asymptotic freedom to describe this early stage as a free streaming particles until thermalization [11], others use kinetic theory to propagate the energy-momentum tensor into the next stage [12]. On the other hand, phenomenological techniques are often applied to obtain the spatial distributions of an already thermalized system, "skipping" over the pre-equilibrium evolution.

Even though the precise dynamics is not known, the generic behavior is simple, the compressed system expands. In the meantime, two important things happen: (i) the increase in volume disperses energy in space – lowering the energy density to around

$\epsilon \sim 2$ GeV/fm^3 [9], no longer in the range of asymptotic freedom[3] –, so the quarks and gluons become strongly coupled; (ii) the thermal discontinuities are smoothed into "hot-spots" [14] when thermalization sets, so the thermodynamic fields[4] are continuous in space. Together, these two facts allow for a *relativistic hydrodynamic* description of the system, and the aforementioned thermodynamic fields play the role of initial conditions for the evolution [4]. However, the time it takes for hydrodynamics to be applicable is still an open problem [8].

The system keeps expanding and cooling, with a behavior dependent on the *equation of state* (EoS). This goes on until the confinement enters into effect and clumps quarks together into neutral-color hadrons, transforming the plasma into a hadron gas (HG), which expands further. The hydrodynamic expansion and the quark-hadron transition are a main topic of this thesis, explained in greater detail later.

Eventually, the fluid has expanded enough so that the particles rarely interact and the hydrodynamic description is no longer valid. When this happens, the picture is switched to a system composed of essentially free streaming particles, each with "frozen" abundance and momentum, giving the *freeze-out* name (*decoupling* is also used) to this stage. Realistically, the inelastic interactions between the hadrons in the HG are more likely to cease before the elastic ones [4, 15], so the freeze-out can be separated into two: the chemical freeze-out, when the abundances of particles are fixed; and the kinetic freeze-out, when the particles stop colliding elastically with one another, fixing their momenta.

Some particles that leave the fluid during freeze-out may be heavy and unstable resonances, which decay into lighter and stable particles before reaching the detectors. This creates a correlation between the offspring particles and contributes substantially to some of the detected multiplicities.

1.2 The Phase Diagram

The hydrodynamic evolution, and in particular the transition between the deconfined phase (QGP) to hadron matter (HG), depends on the QCD equation of state, a relation between thermodynamic fields that must hold in equilibrium. A graphic representation

[3] LQCD results at $\mu_B = 0$ (see e.g. [13]) show that the asymptotic limit is beyond $T = 400$ MeV, which corresponds to $\epsilon/T^4 \sim 14$, that is, $\epsilon = 47$ GeV/fm^3.

[4] Energy density, baryon number density, temperature, pressure, and so on.

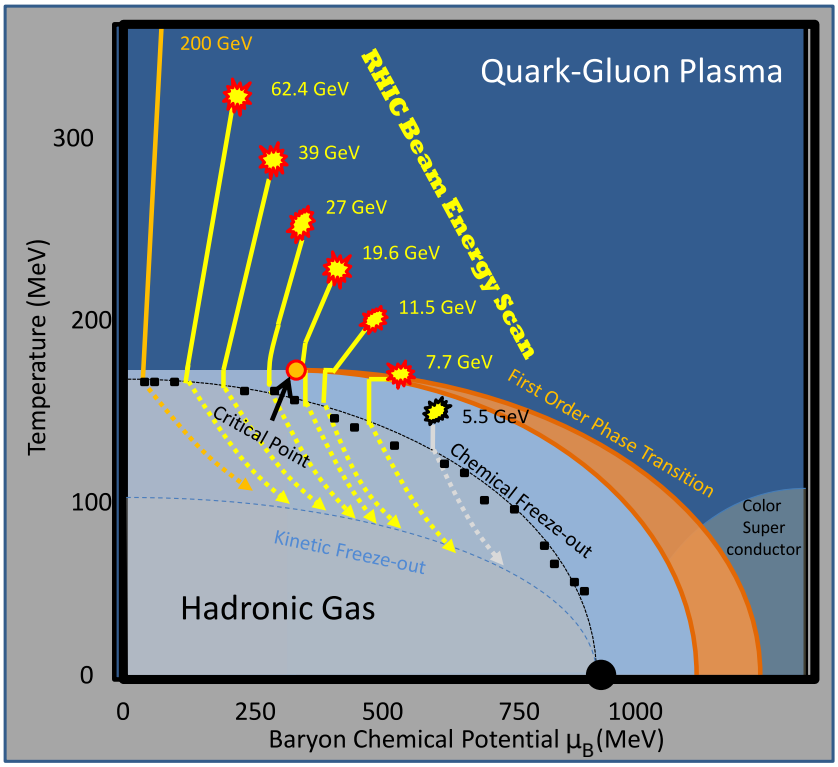

Figure 1.2: Cartoon of the QCD phase diagram, showing the QGP and HG phase as well as the conjectured superconducting phase. An orange line (with some width to represent uncertainty) divides the two known phases with a first-order phase transition starting in the $T = 0$ axis up to the critical end-point. Also shown are the two freeze-outs, with black dots from measurements of multiplicity ratios, and in yellow the expected trajectories (cf. §2.2) of an element of fluid in an HIC of the Beam Energy Scan experiment, in the selected energies. Taken from [16].

of the EoS is given by a *phase diagram*, a plot in the space of thermodynamic parameters where lines or regions of specific behavior can be delineated. In particular, it separates the different phases in which the system can be. For QGP and hadronic matter, it is more convenient to plot the phase diagram using the plane[5] of temperature T by baryon chemical potential μ_B.

Although the QCD equation of state is not known exactly, the generic behavior must follow the description above: at high energy densities, quarks and gluons are asymptotically free; at low energy densities, they clump inside neutral-color hadrons. In the (T, μ_B) phase diagram this is represented as in Fig. 1.2. Other than the QGP and HG phases, this diagram also shows a *superconducting phase* (also called color-flavor locked), which is expected to happen in dense cold quark matter, when quarks near the Fermi surface condense in Cooper pairs, in analogy to superconducting metals [17, 18]. This phase has not

[5]When necessary, other or more axes can be used, such as the charge chemical potential or quark mass. If not, usually the former is fixed at zero and the latter is the bare mass.

yet been observed, but is conjectured to appear inside neutron/compact stars (NS) [19].

The evolution of the system is determined by the equations of motion, and can be plotted on the phase diagram in lines called *trajectories*, restricting where a fluid element can be, given the initial condition. For instance, ideal hydrodynamics conserve the entropy per baryon, so the trajectories are lines of constant σ/n_B, plotted on the (T, μ_B) plane using the EoS and represented by the yellow lines in Fig. 1.2.

In the high μ_B region with $T \sim 0$, astronomical observations impose constraints on the EoS. Some NSs with more than 2 solar masses have been observed, which favors stiff EoSs but not necessarily proves a first-order transition [20]. Furthermore, NS mergers may provide particular signatures unambiguously related to a first-order transitions [21]. Also at $T = 0$, several QCD-based phenomenological models indicate that the transition is of first-order (see e.g. [22]).

In the temperature axis ($\mu_B = 0$) the Lattice QCD (LQCD) is well-established as a non-perturbative numerical approach to first principles QCD. It consists in discretizing spacetime into lattice sites with separation a; quarks can be placed on the sites and the gluon fields are defined at the links in-between. The partition function, in the form of a path integral[6] of the probabilities $\exp(-S_E)$, is also discretized in these sites. Then, Monte-Carlo sampling is applied to evaluate it, taking advantage of the fact that a relatively small subset of field configurations have a small action – that is, a sizable $\exp(-S_E)$ – and will contribute significantly [23, 24]. The thermodynamics then follow from derivatives of the partition function. LQCD results show that the transition between confined to deconfined matter at $\mu_B = 0$ is smooth in the thermodynamic variables [25, 26]. This is called a *crossover*.

1.2.1 The Critical End-Point

A logical consequence of the two distinct types of transitions described above is that the line of first-order transitions eventually gives way to the smooth crossover. The point (T, μ_B) where this line ends is called the QCD *Critical End-Point* (CEP or CP). This point has interesting characteristics which make it very desirable to locate, and currently there is great effort to do so from both theoretical and experimental standpoints.

[6] Since the partition function $\mathcal{Z}(T, \mu_B)$ is a sum over eigenstates of the Hamiltonian, it can be expressed as a functional integral over all field configurations, weighted by their probabilities given by the "Gibbs" factor $\exp(-S_E)$, where S_E is the Euclidean action with T in the role of Euclidean time.

The QCD CP is commonly introduced in analogy to a more day-to-day critical point, that of boiling water at $T \approx 647$ K, $P \approx 22$ MPa, shown in Fig. 1.3. At higher pressures and temperatures, the distinction between liquid water and vapor is gone, and the fluid is said to be *supercritical*. In the first-order line, boiling water creates a mixed phase (horizontal segment), where vapor and liquid are coexisting until the relative density is 0, i.e. all the liquid has evaporated, so the plot of $P \times (1/\rho)$ has a constant region at $T = T_c$. Precisely at the CP, the transition is of second order, and the pressure has an inflection point.

In statistical physics, the steps to finding critical points in a system are simple and straightforward: compute the partition function $\mathcal{Z}$ from the corresponding Lagrangian, and find where an inflection point appears (first and second derivatives zero, but not the third). However, it is easier said than done. For QCD, the partition function is an infinite-dimensional integral, as mentioned above, and evaluating it analytically is not possible [24].

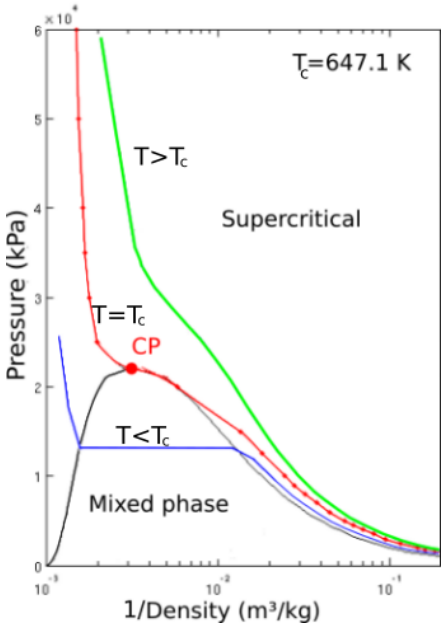

Figure 1.3: A phase diagram of water, with three possible lines near critical temperature $T = 647.1$ K. The green line is smooth in the supercritical region. The blue one goes through the first-order phase transition, with discontinuous concentration. The red one passes through the CP and has a kink. Adapted from [27].

While it is possible to use LQCD to do so, it comes with a serious disadvantage, called the *sign problem*. Essentially, at non-zero μ_B, the Euclidean action gains an imaginary term, so its exponential becomes oscillatory. This is a problem because the probability used in the Monte Carlo sampling of LQCD is proportional to $\exp(-S_E)$, and should not be complex [28].

Effective model calculations are also possible, with many different starting points. Among them are the Nambu-Jona-Lasinio (NJL) Lagrangian, chiral hydrodynamics, bootstrapping and random matrices (see [24] and references therein). However, they are usually tuned to match QCD at $\mu_B = T = 0$, therefore the predictions vary wildly. Fig. 1.4(a) shows the vastly different CP locations predicted by these models.

An important property of a CP is the divergence of the *correlation length* ξ, a measure

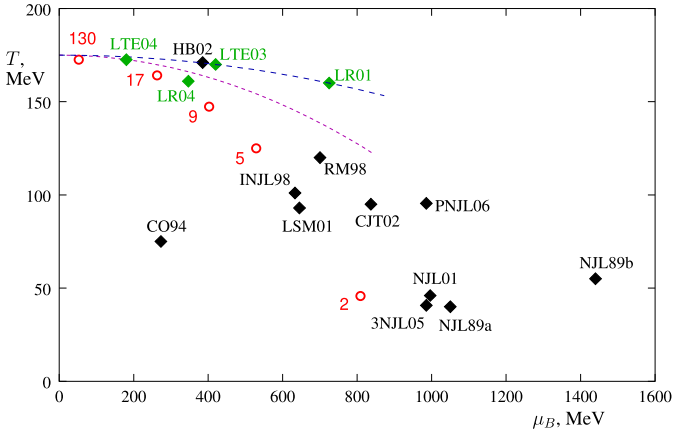

Figure 1.4: (Left) Comparison of predictions for the position of the QCD CP on the phase diagram. Black and green points are predictions from effective models and LQCD, respectively, with the label identifying the specific model or collaboration. The red circles are where the freeze-out happens for HICs at the corresponding $\sqrt{s_{NN}}$ values also in red. Taken from [24]. (Right) Critical opalescence presenting in CO_2, at $P = 7.37$ MPa, $T = 304.13$ K. Taken from [29].

of how distant two particles have to be to become uncorrelated. More precisely, the correlation function $\rho(x, y)$ at a given temperature is defined for two points x and y in space, using the density $n(x)$ of particles at x:

$$\rho(x, y) = \langle n(x)n(y)\rangle - \langle n(x)\rangle \langle n(y)\rangle = \exp\left(-\frac{|x-y|}{\xi}\right), \tag{1.1}$$

where the second equality defines ξ. Intuitively, far away points are usually uncorrelated. However, as the system approaches the CP (from the first-order line), the size of the mixed phase becomes smaller and the amount of matter in each phase fluctuates over larger length scales [30]. Exactly at the CP, $\rho = 1$ everywhere, therefore ξ diverges. What this means is that if a system in the thermodynamic limit (i.e. with an infinite volume) was held at (T_c, μ_c) for an infinite time, ξ would be infinite[7].

Here, an intuitive visualization comes in handy. When approaching the CP in a fluid mixture ξ increases, eventually reaching a size comparable to the wavelength of visible light. This causes light to scatter, turning the fluid opaque. This phenomenon is known as *critical opalescence*, represented in a CO_2 vial in Fig. 1.4(b).

The thermodynamic effect of a diverging ξ is reflected in several quantities such as the heat capacity $c_V = T\,\mathrm{d}\sigma\,/\,\mathrm{d}T$ and, of particular interest, the susceptibilities χ_n of the system, defined as

[7]In practice, there is a non-equilibrium phenomenon called *critical slowing down*, in which the long correlation length near a CP makes it harder for particles to exchange momentum, so ξ does not grow as fast as it would in equilibrium [31].

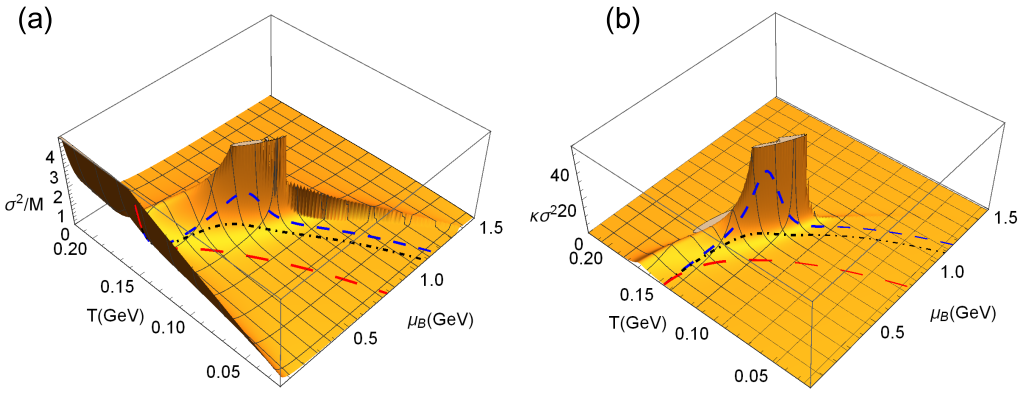

Figure 1.5: A typical behavior of net-baryon fluctuations in the phase diagram, diverging at the CP. Shown here are (left) σ^2/M, equal to χ_2/χ_1; (right) $\kappa\sigma^2$, which corresponds to χ_4^B/χ_2^B. The lines represent possible freeze-out curves, parametrized with parabolas. Taken from [35].

$$\chi_n = \frac{\partial^n (P/T^4)}{\partial(\mu/T)^n}. \tag{1.2}$$

From the σ-field model, in which the effective action is expanded in powers of an order parameter field $\sigma(x)$, it can be shown that the χ_n diverge with ξ, and that higher order susceptibilities depend on higher powers of the correlation length. In particular, $\chi_2 \propto \xi^2$ but $\chi_3 \propto \xi^{4.5}$ and $\chi_4 \propto \xi^7$ [32, 33]. Of course, the system has a limited size so ξ never really grows to infinity, but the higher-order susceptibilities are still more sensitive to the CP and provide clearer signals of criticality.

Then, this high sensitivity to the CP can be used to determine its location experimentally in HICs. The stronger fluctuations increase the non-gaussianity of probability distributions, which can be seen in *event-by-event* measurements of multiplicities. Of course, this relies on the fluctuations not being destroyed during the hydrodynamic evolution after the system has passed through (or near) the CP. Luckily, the QCD CP seems to present the effect of "focusing", where the trajectories of the system are attracted to the CP. This, along with the diverging c_V, means that the system is more likely to stay longer near the CP, so that the freeze-out happens close to it and the signal is not destroyed [34]. Fig. 1.5(b) shows two ratios of susceptibilities (for observational reasons) with some possible freeze-out lines, with the best-case scenario in blue.

Another noteworthy fact is that *how* the correlation length diverges with temperature does not depend on specific microscopic details of the system, only on the degrees of freedom and their symmetries. This idea is called *universality*, where the long-range correlations near the CP give rise to a collective behavior of the system. For instance,

near the CP, ξ can be expressed with a power law

$$\xi(T) \propto |T - T_c|^{-\nu}, \tag{1.3}$$

where ν is a *scaling exponent* [36]. Systems with the same symmetries have equal scaling exponents, and belong to a *universality class*, even if they seem completely unrelated. The modern way to describe criticality is in the context of *renormalization groups*.

In the case of two massless quarks and assuming the axial anomaly at the critical temperature, the relevant symmetry group is $\mathrm{SU}(2)_L \times \mathrm{SU}(2)_R$ which is homomorphic to O(4), so in the massless (chiral) limit QCD is in the 3D O(4) universality class. Since in real life the quarks are massive and have different masses, only the sign-flip symmetry of the order parameter σ remains, that is, QCD is in the 3D $\mathbb{Z}_2$ universality class [37].

This can be useful to study the QCD phase diagram, as it is possible to map its (T, μ_B) coordinates onto the 3D Ising model, since they share symmetries [32]. In turn, this may serve as a basis for the construction of equations of state [38].

1.3 Outline

We have seen above the importance of the event-by-event fluctuations in conserved charges to locate the QCD critical point. In the following, I will concentrate on these quantities. The remainder of this work is divided as follows: chapter 2 describes the main theoretical ideas relevant for the work, namely the NeXus model, the ideal equations of motion and the EoS used, and the Cooper-Frye prescription for the freeze-out. In chapter 3, I briefly overview the NeXSPheRIO code used in this work, and explain the *Smoothed Particle Hydrodynamics* method for hydro evolution. Chapter 4 develops a method to compute cumulants in hydrodynamics that reduces computational cost, and explores some of its subtleties. In chapter 5, I describe the calibration made on NeXSPheRIO, and compare some preliminary results of the method with experimental data. Chapter 6 reviews the work and discusses some possible plans for using the method developed. Appendix A deals with some results from statistical mechanics relevant for this thesis and B provides details of some hydrodynamical calculations.

Chapter 2

Theoretical Ingredients

The current theoretical paradigm of a heavy-ion collision is mainly based on splitting the process in three stages, as pictured in Fig. 1.1: first, a collision model is selected. It must provide the initial conditions (ICs) in the form of relativistic fields. Then, these ICs are fed into some expansion code, usually hydrodynamical. Finally, the evolved fields in the system must transform into detectable particles, with or without a transport model or resonance decays.

Following such modularization, in this chapter I will present chronologically the theoretical components applied in the NeXSPheRIO code, focusing on the aspects most relevant to this work. The implementation and technical details are discussed in Ch. 3.

2.1 Initial Conditions

Just like the Universe in the moments succeeding the Big Bang, the system right after a HIC is a complex hot dense medium. Many complications arise with the non-abelian character of Quantum Chromodynamics (QCD), and so far there is no way to treat nuclear processes strictly within the framework of a field theory based on first principles. As discussed in §1.1, a common procedure in a HIC simulation is to use an effective theory (from [39, 40], in the present case) that is both calculable and consistent with QCD. Furthermore, recently there has also been some new developments in describing the pre-equilibrium (early-time dynamics and thermalization) stage after the impact, with models such as the IP-Glasma [41, 42]. In the NeXSPheRIO code used in this work, the initial conditions correspond to starting from an already thermalized system.

The ICs used in this work come from the NeXus model [39, 40, 43], a parton-based Gribov-Regge theory. In this section, I will briefly describe the model and present the initial profiles, merely sketching a picture; the extensive construction is left for the original paper [39].

2.1.1 The NeXus model

In a highly energetic HIC, Lorentz contraction flattens the longitudinal dimension of the nuclei ($\sim$ 0.1 fm at top RHIC energies), so the interactions between nucleons can be considered instantaneous. This primary vertex creates many partons (quarks and gluons), which interact out-of-equilibrium, until thermalization sets at some $\tau = \tau_0 > 0$. The approach in the NeXus model is to treat these primary interactions as exchanges of phenomenological particles called "pomerons", whose precise nature and internal structure is not known, therefore parametrized by experimental results. Using general rules of field theories, cross sections and particle yields can be expressed in terms of these parameters.

For elastic parton-parton collisions, the model bridges two "ends" of the high-energy spectrum [39], and the possible pomeron diagrams are shown in Fig. 2.1:

1. At very high energies, a collision between valence quarks will have a lot of intermediate partons with large momentum $Q^2 > Q_0^2$, for some reasonable cutoff Q_0 ($\sim 1\text{GeV}^2$). For these partons, perturbative QCD is applicable in a parton cascade fashion [4], allowing for the computation of scattering amplitudes through Feynman diagrams, represented by a parton ladder.

2. At low (not too high) energies, the virtual partons have a low momentum $Q^2 < Q_0^2$, and soft non-perturbative dynamics dominate, so the scattering amplitude has to be parametrized phenomenologically, being represented by a "blob".

3. In the case of sea quarks and gluons, the virtual partons may be slow even at high energies, appearing as a result of non-perturbative parton cascades, where each branch shares a small and similar momentum transfer. At the parton-parton level, they can be included in the soft parametrization, but in inelastic hadronic interactions they must be treated separately in order to account for secondary particle production, due to interference terms. They are computed as a convolution between hard and soft amplitudes, fittingly represented by parton ladders with soft ends.

For consistency's sake, mixed contributions (parton ladders with one soft end) are also taken into account.

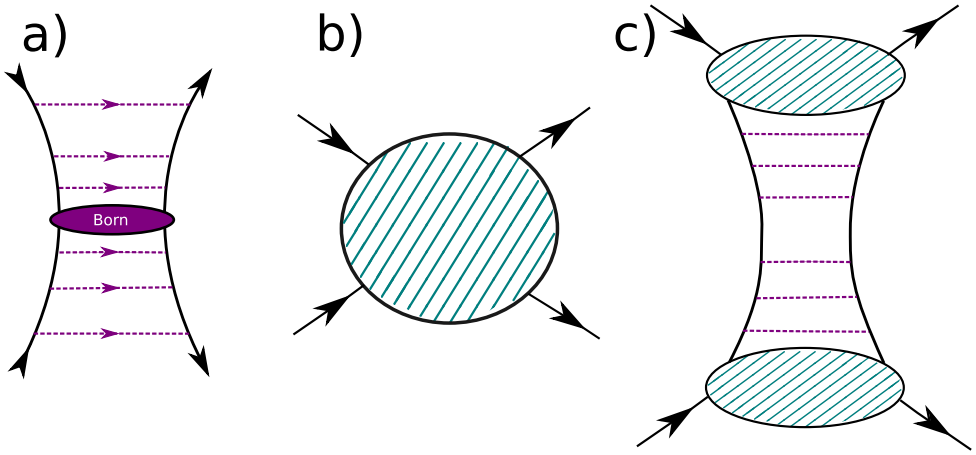

Figure 2.1: Diagrams of pomerons contributing to the elastic two-parton interaction. (a) Hard process from valence quarks, with higher virtual momentum transfers towards the "center" of the ladder. (b) Soft contributions, parametrized phenomenologically. (c) Semi-hard processes (including cascades with only one soft end), that dominate the energies where experiments are performed, computed as a convolution of the previous two.

The $2 \to 2$ elastic parton scattering amplitude $\mathcal{M}_{2\to2} = \mathcal{M}_{\text{hard}} + \mathcal{M}_{\text{soft}} + \mathcal{M}_{\text{sea}}$ has an inelastic counterpart, which corresponds to cutting a pomeron via AGK rules [44]. Then, the amplitude for a *hadron-hadron* collision is simply the sum of multiple (cut and uncut) pomerons from different parton constituents, assuming some momentum share distribution for the valence quarks.

Finally, the scattering amplitude $\mathcal{M}_{AB}(s, b)$ of a collision between two nuclei is simply the appropriate sum of diagrams corresponding to multiple scatterings processes [40], that is, each nucleon can collide many times. The inputs for this are the center-of-mass energy $\sqrt{s}$ and the number N_{part} of participant nucleons, which is obtained from a nuclear form factor in conjunction with the impact parameter b, given the nuclear masses A of the target and B of the projectile.

Then, the total interaction cross-section reads

$$\sigma^{AB}(s) = \int \mathrm{d}^2 b \int \mathrm{d}T_{AB} \, \frac{1}{s} \mathrm{Im}\left[\tilde{\mathcal{M}}_{AB}(s, b)\right], \tag{2.1}$$

where T_{AB} is a shorthand for the nuclear overlap, dependent on the nuclear form factors, and $\tilde{\mathcal{M}}$ is the Fourier transform of the amplitude $\mathcal{M}$. In this work (as well as in most literature) the Woods-Saxon density distribution [9] is used. The output is a 3D particle spectra, sampled from the differential version of (2.1) via Monte-Carlo simulations.

2.1.2 Initial profiles

The NeXus model provides a theoretically consistent way to compute the results of primary interactions, after $\tau_0 = 1$ fm/c, given[1] the number of nucleons A and B in the projectile and target, the impact parameter b, and the energy of collision (either in center-of-mass or laboratory frames) $\sqrt{s}$. But in order to interpret these results as initial conditions, the outgoing particles from the NeXus calculation must be mapped onto fields of macroscopic quantities such as energy and baryon density. This is not trivial, as only the momenta of hard partons are resolvable in a given proper time. The problem is solved using the string model, that treats soft partons implicitly. The description of strings is beyond the scope of this thesis, but can be found in great detail in [40, 43] and references therein.

Examples of typical initial profiles are shown in Fig. 2.2. Their behavior is intuitive: as the center-of-mass energy (that is, the velocities of the nuclei) grows, the energy density follows; the net-baryon density decreases *at mid-rapidity* because the fragmentation regions become farther apart, that is, the nuclei pass through each other more easily, leaving a dip in density at the collision center [9, 45]. This phenomenon is known as *baryon stopping*.

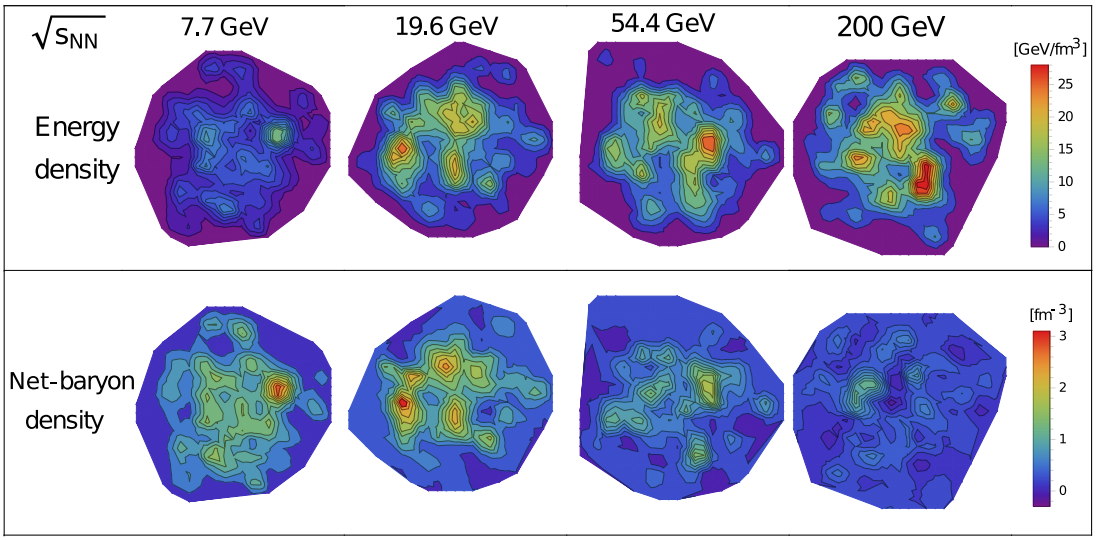

Figure 2.2: Transversal initial profiles from NeXus output with different center-of-mass energies, selected to match the Beam Energy Scan configurations [16], in central ($b = 0$) Au+Au ($A = B = 197$) collisions at mid-rapidity ($y = 0$). The plots span 20fm in each direction.

However, it turns out that these profiles do not correspond to matter in local equilibrium, and therefore a forced thermalization procedure is made to initialize the hydrody-

[1] As discussed, more parameters go into a NeXus simulation, but the others not mentioned, such as the infrared scale $\Lambda_{\mathrm{QCD}} = 200$ MeV and the nuclear surface thickness $a = 0.54$ fm, are fixed.

namic evolution, as described in §3.2. The final rapidity distributions of NeXSPheRIO do not reproduce experimental results accurately, as will be seen in Ch. 5, which may be due to a wrong baryon stopping in the NeXus ICs or the forced thermalization, or both.

2.2 Hydrodynamic Evolution

After a high energy nucleus-nucleus collision, the system will naturally have a vast number of degrees of freedom, so a particle by particle description of its behavior is usually unfeasible. However, these microscopic degrees of freedom usually follow a large, collective motion coupled to small and isotropic movements, the latter being typically much faster than the former. This allows for an effective statistical description where the interest resides on the overall behavior, and the macroscopic properties of the system are taken as the relevant degrees of freedom.

The attempts to describe the outcome of high energy collisions in these lines started with Fermi's statistical model [46,47] in 1950. It described well the multiplicity of particles produced as a function of the collision energy, but failed to correctly determine the angular distribution in "distant" peripheral (large b) collisions. After some heated debate[2], Landau fixed this problem by introducing his hydrodynamical model [48, 49], where he proposed the use of relativistic hydrodynamics, arguing that the high density and strong force would not allow for the system to set on a definite number of particles right after the impact. There should be an expansion so that the strong interaction becomes small enough for the particles to escape freely. The success of this model was great, and it remains as the baseline for our descriptions to this day [4, 9].

Since then, the hydrodynamic description of relativistic nuclear collisions has been well established and the fluid created initially, dubbed Quark Gluon Plasma (QGP), was found to have an extremely low viscosity, the lowest known to man [50], so it has been dubbed "the most perfect liquid". Therefore, it is within reason to describe the system expansion with the ideal fluid model. In this section, I describe the ideal hydrodynamics, and subsequently develop the equation of state (EoS) necessary to complete the system of equations. Explicit calculations are provided in the appendices A.1 and B.

[2]Landau stated that Fermi's reasoning and calculations were "*unconvincing and incorrect at several points*", which some might consider heated.

2.2.1 Equations of Motion

Some time after the collision happens, the system enters local equilibrium and the hydrodynamic evolution takes place. The energy-momentum tensor of a thermalized ideal fluid in an arbitrary frame is

$$T^{\alpha\beta} = (P + \epsilon)u^\alpha u^\beta - P g^{\alpha\beta}, \tag{2.2}$$

whose conservation laws provide the equations of motion

$$\partial_\alpha T^{\alpha\beta} = 0, \tag{2.3}$$

and where u^α is the fluid four-velocity in the frame, and $g^{\alpha\beta} = \mathrm{diag}(+,-,-,-)$ is the Minkowski metric. If conserved charges[3] N_i are present, their densities $n_i \equiv \dfrac{N_i}{V}$ also have an associated equation

$$\partial_\alpha (n_i u^\alpha) = 0. \tag{2.4}$$

In the following, I will simplify things by taking one charge only, namely the net-baryon number $i = B$, but the generalization is straightforward.

Together with thermodynamic considerations, there are two important consequences to the relations above. One of them is the conservation of entropy, whose volume density $\sigma \equiv S/V$ obeys

$$\partial_\alpha (\sigma u^\alpha) = 0, \tag{2.5}$$

The other consequence is that, since the baryon current (2.4) is also conserved, the trajectories of the system in the phase diagram will be given by lines of constant entropy per baryon $\dfrac{\sigma}{n_B}$, sometimes referred to as baryon asymmetry [28]:

$$\frac{\mathrm{d}}{\mathrm{d}\tau}\left(\frac{\sigma}{n_B}\right) = 0. \tag{2.6}$$

So far, the variables at hand are the pressure $P(x^\alpha)$ and energy density $\epsilon(x^\alpha)$ fields, three from the velocity field $\vec{u}(x^\alpha)$, and one from the net-baryon density field $n_B(x^\alpha)$, for a total of 6 degrees of freedom. However, the conservation laws provide us with only 4

[3]Net-baryon number, electric charge and strangeness, in the case of HICs

equations from (2.3) plus one from (2.4), which do not specify anything about the fluid itself. Therefore, in order to close the system of equations, an extra relation is needed, one that characterizes the properties of the matter that composes the fluid, called the *equation of state*.

2.2.2 Equation of State

This equation must relate the thermodynamic state variables, such as $P = P(T, \mu_B)$, without depending on the dynamics, and it is guaranteed to exist from the hypothesis of local equilibrium [51].

As discussed in Ch. 1, the goal is to to describe the strongly interacting QGP at high temperatures and baryonic densities, as well as the hadronic matter that gives rise to the particles that reach the detectors. Furthermore, the EoS also presumably has a crossover region at low μ_B [25] and a first-order phase transition at high μ_B [22,52]. These requirements can be met with the following toy equation of state [14, 53, 54]:

$$\boxed{(P - P_{\rm H})(P - P_{\rm Q}) = \delta(\mu_B) \equiv \delta_0 \exp\left[-\left(\frac{\mu_B}{\mu_c}\right)^2\right]} \tag{2.7}$$

Here, $P = P(T, \mu_B)$ is the pressure of the system; μ_c and δ_0 are parameters of the function $\delta(\mu_B)$ setting the position and sharpness of the CEP. $P_{\rm H}$ and $P_{\rm Q}$ are functions of (T, μ_B) as well, determined by equations of state chosen for the hadronic and quark-gluon phases, respectively. In this section, for illustration, I use a sum of different gases within the Hadron Resonance Gas (HRG) model for $P_{\rm H}$, applying a finite volume correction; and the MIT Bag model for $P_{\rm QGP}$ [9, 14]. These models are described in better detail in Appendix B.

If (2.7) is solved with respect to P, some algebra[4] makes its meaning clearer.

$$P = \zeta P_{\rm H} + (1 - \zeta) P_{\rm Q} + \frac{2\delta}{\sqrt{(P_{\rm H} - P_{\rm Q})^2 + 4\delta}}, \tag{2.8}$$

where I define the parameter

[4] Omitting the dependence on μ_B and T for the sake of readability.

$$\zeta = \zeta(T, \mu_B) \equiv \frac{1}{2}\left[1 + \frac{P_{\rm H} - P_{\rm Q}}{\sqrt{(P_{\rm H} - P_{\rm Q})^2 + 4\delta}}\right]. \tag{2.9}$$

When $\mu_B \gg \mu_c$, the exponential in the r.h.s. of (2.7) vanishes and $\delta(\mu_B) = 0$, so ζ is either 1, when $P_{\rm H} > P_{\rm Q}$, or 0 otherwise. In turn, this means that in (2.8) the system is either in the hadronic form or in the quark-gluon form. When $P_{\rm H} = P_{\rm Q}$, there is a first-order phase transition and a mixed phase. On the other hand, when $\mu_B \ll \mu_c$, δ is non-zero, so ζ is continuous and the transition between both phases is smooth, leading to the crossover. Figs. 2.3 and 2.4(a) illustrate the pressure (2.8) in the phase diagram.

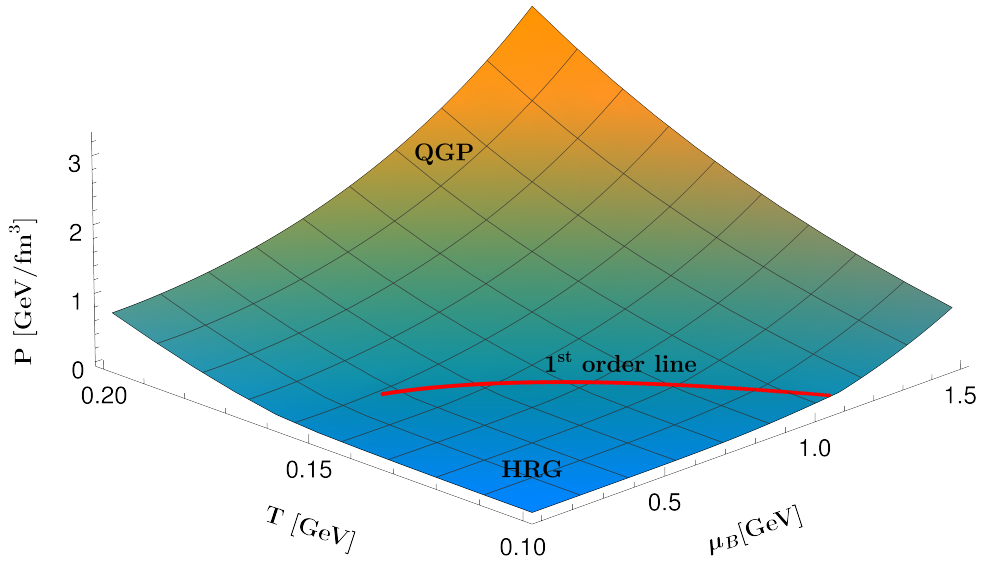

Figure 2.3: Pressure as a function of temperature T and baryon chemical potential μ_B. Red line shows the first-order phase transition.

From the first law of thermodynamics, written as

$$P(T, \mu_B) = T\sigma + \mu_B n_B - \epsilon, \tag{2.10}$$

it is straightforward to determine the other thermodynamical variables:

$$\sigma = \zeta\sigma_{\rm H} + (1-\zeta)\sigma_{\rm Q}; \tag{2.11}$$

$$n_B = \zeta n_{B,{\rm H}} + (1-\zeta)n_{B,{\rm Q}} - \frac{2\delta}{\sqrt{(P_{\rm H} - P_{\rm Q})^2 + 4\delta}}\left(\frac{\mu_B}{\mu_c}\right)^2; \tag{2.12}$$

$$\epsilon = \zeta\epsilon_{\rm H} + (1-\zeta)\epsilon_{\rm Q} - \frac{2\delta}{\sqrt{(P_{\rm H} - P_{\rm Q})^2 + 4\delta}}\left[1 + \left(\frac{\mu_B}{\mu_c}\right)^2\right]. \tag{2.13}$$

The behavior of these quantities is also shown in Fig. 2.4. Since they are derivatives of the pressure, the kinks in the pressure at high values of baryon chemical potential

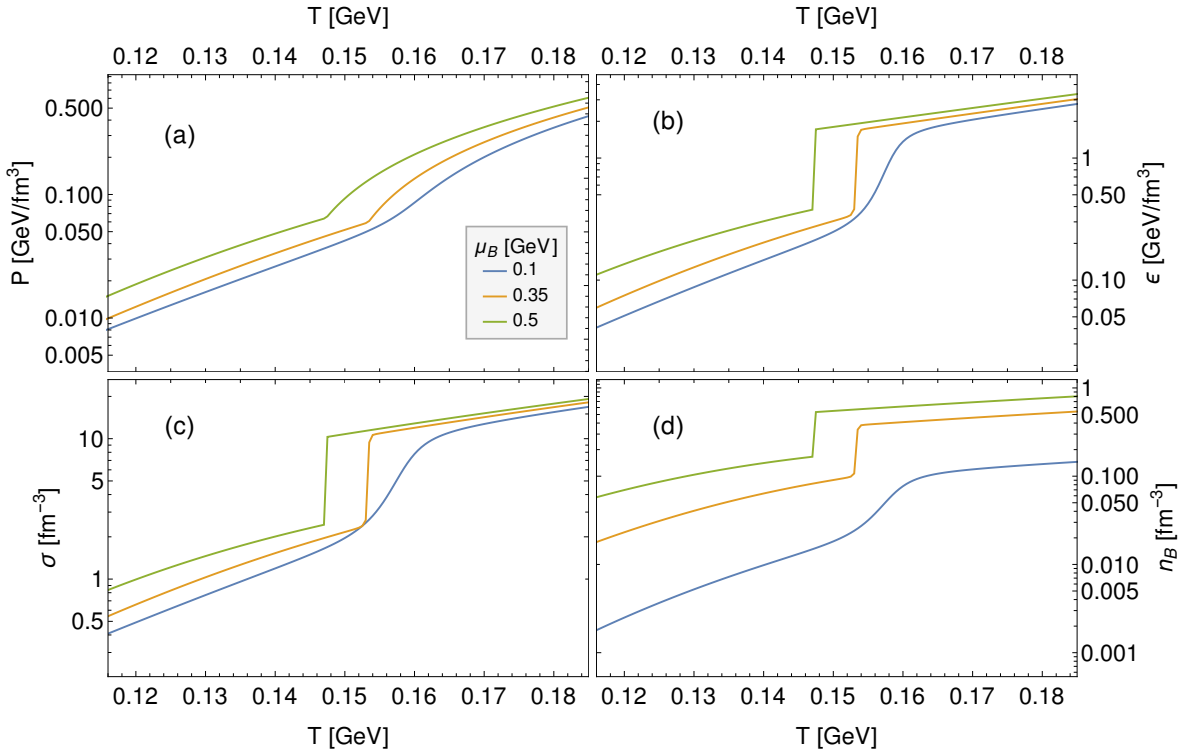

Figure 2.4: Thermodynamical variables (a) pressure P, (b) energy density ϵ, (c) entropy density σ and (d) net-baryon density n_B as functions of temperature T for different values of baryon chemical potential μ_B near the critical region.

are translated into discontinuities. At the CP, when[5] $\mu_B \approx \mu_c = 0.35$ GeV, these first derivatives are continuous functions of T, but change very quickly near $T_c = 0.155$ GeV, where the transition is of second-order. Finally, when μ_B is small, the change from QGP to hadronic matter is smooth, in agreement with Lattice QCD results [25, 34]. Further analysis of this EoS and comparisons to others can be found in [53, 54].

Finally, upon dividing (2.11) by (2.12), the trajectories of baryon asymmetry (2.6) from the equations of motion can be drawn in the phase diagram of this equation of state, as seen in Fig. 2.5 explicitly. These trajectories can be understood as follows.

First of all, the σ/n_B line is fixed at the initial stage, depending on the collision parameters such as the beam energy $\sqrt{s}$ or the centrality $\mathcal{C}$; faster ions or more central collisions shift the baryon asymmetry to higher values[6]. The system starts distributed over a region in the QGP phase, and cools down following the constant σ/n_B lines until

[5]The EoS in NeXSPheRIO uses the values $\mu_B = 0.178$ GeV and $\delta_0 = 0.45$ GeV^4.

[6]This is reflected in the changes in total multiplicity, which are much larger in comparison to the ones suffered by the baryon number.

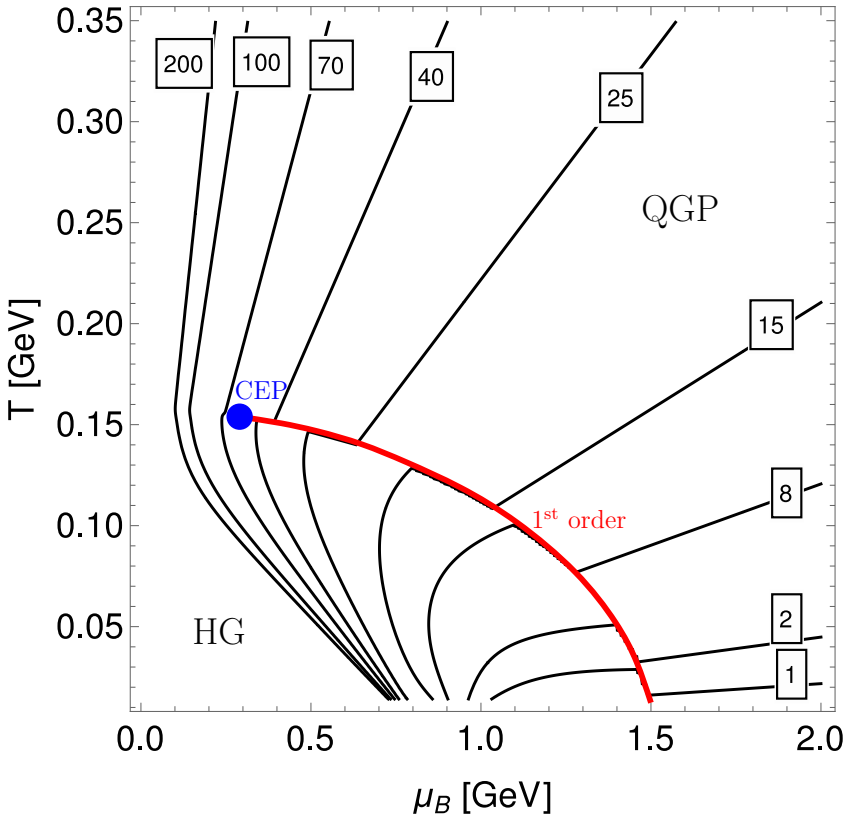

Figure 2.5: Phase diagram of (2.7). Black lines are the trajectories (2.6) of constant entropy per baryon, with the σ/n_B values indicated by the boxed numbers. The red line indicates the first-order phase transition, ending at the blue critical point $(T, \mu_B) = (0.155, 0.35)$GeV, with a radius inversely proportional to δ_0.

changing phase, which can happen in essentially two ways: (i) either the system passes through the crossover region, or (ii) it will meet the 1st order transition line, red in Fig. 2.5. The line is actually a mixed phase region, with the hidden parameter being the volume fraction of the coexisting phases. In this line, as the quarks clump and form the hadrons, latent heat is released, increasing T and decreasing μ_B so as to maintain a constant σ/n_B [28, 34]. In the HG phase, the fluid briefly expands more until freeze-out.

As mentioned in Ch. 1, the thermodynamic quantities of particular interest for this work are the susceptibilities (1.2), defined as derivatives of the scaled pressure, with respect to the reduced chemical potential, written as:

$$\chi_n^B = \frac{\partial^n (P/T^4)}{\partial (\mu/T)^n}. \tag{2.14}$$

The pressure (2.8) can be used to evaluate susceptibilities of orders n for the EoS (2.7); the first two are shown in Fig. 2.6. They do not effectivelly diverge at the transition because these were computed numerically using finite difference, from a table containing

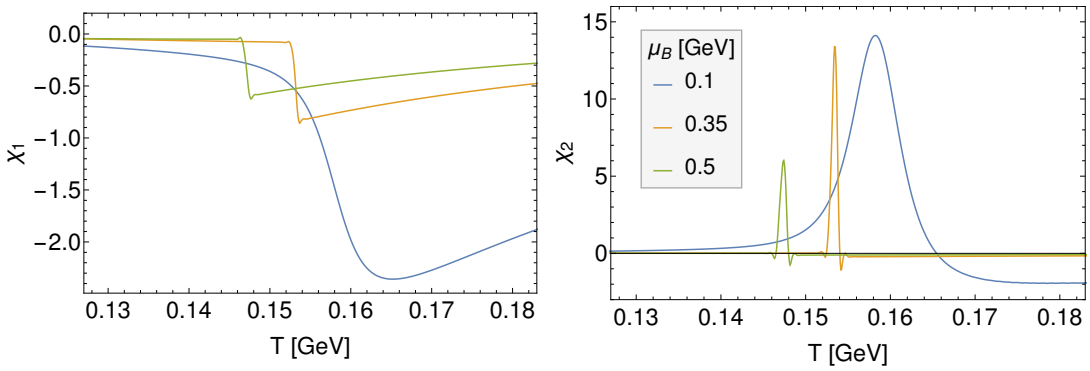

Figure 2.6: First two net-baryon susceptibilities (2.14) as functions of T for different μ_B.

P, μ_B and T, which also gives rise to some quivering near abrupt changes. The observables related to χ_n actually measured in heavy-ion experiments are called *cumulants*, to be discussed in Ch. 4, and the connection is derived in §A.2. Furthermore, direct computation of susceptibilities via the EoS does not give much insight to the results from a HIC simulation, because hydrodynamic washing out and acceptance cuts may be applied, which would introduce non-trivial effects to the measurements of cumulants.

2.3 Freeze-out

As the system expands during the hydrodynamic evolution, it cools down and becomes dilute. Eventually, this causes the Knudsen number to grow too large for hydrodynamics to be applicable [55] and a switch in description from fluid to individual particles must be made. One of the most common ways to do this is via a sudden freeze-out, following the *Cooper-Frye prescription* [56], in which particles are emitted from the fluid once they reach some pre-established condition. These newly born particles are sampled according to the grand-canonical ensemble, with the probabilities for emission determined by the thermodynamics of the fluid element producing them. Of course, this means that global conservation laws are neglected at the stage, because in the grand-canonical picture, quantum numbers, energy and momentum are only conserved on an *average* of events, not on the event-by-event basis [57]. This may pose a challenge to study event-by-event fluctuations of net-charges, since fictitious fluctuations are introduced. However, the method proposed in this work takes care of this.

The decoupling condition in this work is $T(x^\alpha) = T_{FO}$, with a *freeze-out temperature* taken to reproduce the transverse momentum spectra for each collision configuration.

A freeze-out with a single condition may cause some discrepancies in comparisons with experimental data, because in real life the reactions with smaller cross-sections stop earlier than more likely ones with larger cross-sections, but simulating this realistically would require extensive alterations to the hydrodynamic formulation and the equation of state (since the degrees of freedom change). Nonetheless, following [54, 58, 59], this work uses a fixed T_{FO} for the decoupling process in a collision event, and in this section I describe the particle sampling based on the Cooper Frye formula for decoupling. The implementation of the Cooper-Frye prescription in the context of this work is presented in §3.3.2.

2.3.1 The Cooper-Frye prescription

In a sudden freeze-out, after the expansion drops the local temperature of an element of fluid to $T = T_{FO}$, its evolution abruptly stops and the fluid is transformed into individual particles that propagate freely in a hadron gas until "detection". Since this fluid element is assumed to be in local thermodynamic equilibrium, the single-particle probabilities for emission are assigned according to the quantum ideal gas distribution [4]

$$f_\theta(p \cdot u) = \frac{g}{(2\pi)^3} \left[\exp\left(\frac{p \cdot u - \mu}{T} \right) + \theta \right]^{-1}, \tag{2.15}$$

where $\theta = +1(-1)$ corresponds to Fermi-Dirac (Bose-Einstein) statistics and g is the degeneracy factor of the species, and the spatial dependence of the hydrodynamics $T = T(x^\alpha)$, $u^\beta = u^\beta(x^\alpha)$ and $\mu = \mu(x^\alpha)$ is implied.

The function f_θ is the differential distribution $\dfrac{\mathrm{d}N}{\mathrm{d}^3x\,\mathrm{d}^3p}$ on the phase space, so the density $n = \dfrac{\mathrm{d}N}{\mathrm{d}^3x}$ of emitted particles is the integral of (2.15) over all possible momenta, which is made covariant[7] by replacing the density with the particle four-current density given by

$$j^\alpha = \int \mathrm{d}^3p\, f_\theta(p \cdot u) \frac{p^\alpha}{p^0}, \tag{2.16}$$

where $p^0 = E$.

The freeze-out condition $T(x^\alpha) = T_{FO}$ defines a 3-surface $\Sigma = \Sigma(T_{FO})$ in Minkowski space, from where particles are emitted. This hypersurface is divided into many small

[7] The quantity $\dfrac{\mathrm{d}^3p}{E} = 2\delta(p^2 - m^2)\,\mathrm{d}^4p$ is a Lorentz invariant.

cells, characterized by the normal vectors $\mathrm{d}\Sigma_\alpha(x)$ and treated independently. Then, the quantity $p^\alpha\,\mathrm{d}\Sigma_\alpha$ can be thought of as the contribution of momentum p^α to the multiplicity from the fluid element $\mathrm{d}\Sigma$. Usually, this contribution will be positive, with the surface pointing along the preferential direction of fluid motion.

However, some cells may be oriented in a way that the projection of p_α is negative, due to inhomogeneities in the fluid. Fig. 2.7 illustrates these situations in a $(1+1)$D plane. The clear interpretation is that $p_\alpha\,\mathrm{d}\Sigma^\alpha > 0$ means that particles are leaving the fluid, while $p_\alpha\,\mathrm{d}\Sigma^\alpha < 0$ happens when the fluid reabsorbs them, and more matter is moving inward than outward.

In this work, the negative contributions are ignored. This is a standard procedure, but leads to a violation of conservation laws. This problem has been studied before [60], and it might be possible to solve it by switching to a transport code [61], but to my knowledge this has not been accomplished so far.

Furthermore, the average number of particles leaving a cell is simply the flux $\mathrm{d}j^\alpha$ of particles going through the corresponding surface element $\mathrm{d}\Sigma$:

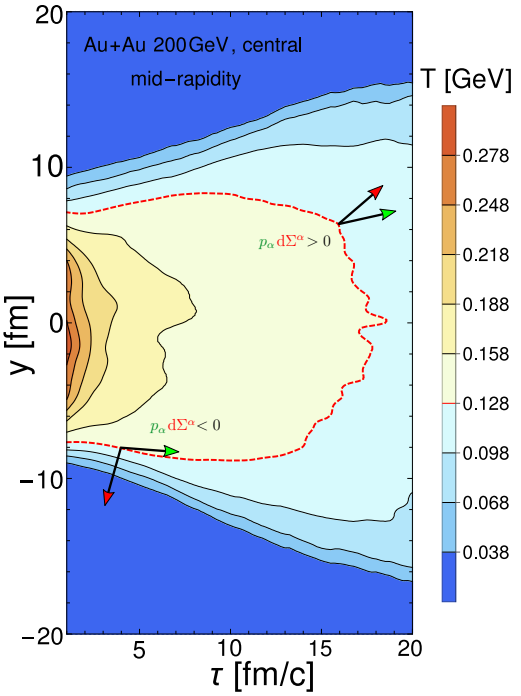

Figure 2.7: Example of $(1+1)$D section of the freeze-out surface. Lines show constant temperatures, with focus in the red $T_{FO} = 0.128$GeV. The red arrowheads show normal vectors to Σ, and the green ones show a possible direction of fluid momentum. Usually the projection is positive (upper right), but sometimes it is not (lower left).

$$\mathrm{d}N = \frac{\mathrm{d}^3p}{E}\,\mathrm{d}\Sigma_\alpha\,p^\alpha f_\theta(p\cdot u). \tag{2.17}$$

Consequently, the spectra of particles of species i produced at freeze-out are given by the well-known Cooper-Frye formula

$$E\frac{\mathrm{d}N_i}{\mathrm{d}^3p} = \frac{g_i}{(2\pi)^3}\int_\Sigma \mathrm{d}\Sigma_\alpha\,p^\alpha\left[\exp\left(\frac{p\cdot u-\mu_i}{T}\right)+\theta_i\right]^{-1} \tag{2.18}$$

Now enters the grand-canonical ensemble (GCE) sampling mentioned earlier. Integration of (2.17) over all possible momenta yields the density $\bar{n}_i$ for each species i, which can be used as the average number of hadrons emitted from the cell, so the multiplicity M of i produced there in a single freeze-out is sampled with the appropriate probability [57]

$$P_\theta(M;\bar{n}_i) = \frac{\bar{n}_i^M}{(1-\theta\bar{n}_i)^{M-\theta}}. \tag{2.19}$$

In practice, though, most species are heavy enough so that this probability is close to a Maxwell-Boltzmann distribution $P_0(M;\bar{n}) = \frac{\bar{n}^M}{M!}e^{-\bar{n}}$, with the notable exception of pions [61]. This implies that these particle species can be considered Poissonic variables at the freeze-out of each fluid element. Since the Poisson distribution is additive, the overall multiplicities or collection of particles – such as baryons, or charged particles– is Poisson-distributed in the full phase space, therefore the net yield (particles minus antiparticles) follows a Skellam distribution, an important observation for the method developed later in this work.

Chapter 3

NeXSPheRIO

The physics of heavy-ion collisions is well known for its great complexity, from both theoretical and experimental standpoints. It is not surprising, then, that a numerical code that tries to simulate such physics will be very intricate. Therefore, a chapter dedicated solely to exploring and explaining it comes in handy.

The code used in this work is called *NeXus+Smoothed Particle Hydrodynamic Evolution of Relativistic heavy-IOn collisions*[1] (NeXSPheRIO). It is a $(3+1)$D hydrodynamical code [59] written in `FORTRAN90`, with good reproducibility of experimental results from RHIC [62] and LHC [63]. A noteworthy strength of NeXSPheRIO is the ability to evolve the system hydrodynamically even for very fluctuating matter [14], such as the initial profiles in Fig. 2.2.

In this chapter, I will describe the general features and structure of the code, present the numerical methods and formulas particularly important for this work and discuss some relevant technical details.

3.1 Code structure

To start deconstructing the code, it is instructive to give an overview of its structure. As discussed in Ch. 2, a HIC is usually separated in three stages: (i) the initial condition, when the nuclei collide and thermalization sets; (ii) the hydrodynamical evolution that expands and cools down the matter; and (iii) the freeze-out, when the fluid is converted

[1] The acronym is written this way to pay homage to the names of the Brazilian home states of the developers of the code, São Paulo (SP) and (RIO) de Janeiro.

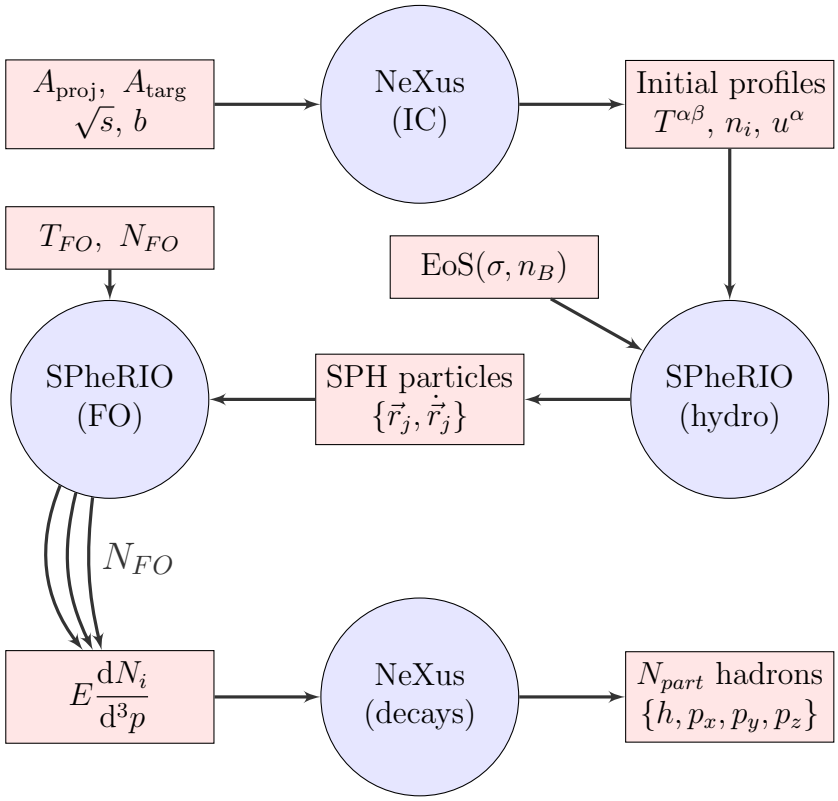

Figure 3.1: Flowchart of a NeXSPheRIO run. Rectangular nodes denote inputs/outputs while circles denote the stages of each code. Inspired by figures in [59, 63].

into particles that arrive at the detector, possibly decaying or interacting in a transport model. The first stage is dealt with by the NeXus code, based on the model of the same name. The other two are done in SPheRIO, a $(3+1)$D hydro code based on a Lagrangian specification[2] of the fluid flow. Then, the freeze-out spectra from SPheRIO is fed to NeXus in order to convert fluid elements into realized hadrons that may decay, depending on chosen settings. The flowchart 3.1 outlines the basic structure of a NeXSPheRIO simulation, detailed below.

First, a `.optns` file containing the collision parameters serves as the input to NeXus. These parameters are the mass number A of the target and projectile ions, the center-of-mass energy $\sqrt{s}$ with which they are colliding, and the range of impact parameter b (which determines the *centrality* of the collision, to be discussed in Ch. 5). This work focuses on Au+Au collisions at $\sqrt{s} = 200$ GeV.

From the allowed impact parameter range, NeXus randomly selects a geometry, and computes the initial distributions at $\tau_0 = 1$ fm. These profiles are the energy-momentum

[2]The observer follows a fluid parcel through space and time, as opposed to an *Eulerian* description, corresponding to looking at fixed locations through which the fluid passes.

tensor $T^{\alpha\beta}$ and the conserved currents $J_i^\alpha = n_i u^\alpha$ $(i = B, Q, S)$, which serve as input for SPheRIO. There, they are converted into SPH particles (defined below) for the hydrodynamic evolution, which uses a tabled equation of state. Here, focus is given to the baryon current J_B^α, with the charge and strangeness densities set to zero.

At every time step, SPheRIO checks for the freeze-out condition $T(x^\alpha) = T_{FO}$, and after every SPH particle crossed this freeze-out hypersurface, the Cooper-Frye prescription is used to sample the particle distribution $E\dfrac{\mathrm{d}N}{\mathrm{d}^3p}$, which can be done N_{FO} times.

These particles go back to the NeXus module, where they may decay with probabilities taken from experiment [64]. The freeze-out and decay configurations are also controlled by commands in the `.optns` file. After that, the final output is a file with N_{FO} lists, each containing N_{part} lines: an ensemble of hadrons where each line has the species h and 3-momentum $\vec{p}$ of a single particle.

Each stage of this simulation may be done separately. For instance, the common procedure is to run some number N_{IC} of initial conditions, which are then classified in centrality windows, and the hydro stage is done only for the windows of interest. In particular, this work focuses on more central collisions. Naturally, each stage takes a different time to run, and Table 3.1 shows the time complexity[3] of each process in a typical central Au+Au 200 GeV collision, with two different processors. Aguia4 is a Linux cluster provided by USP, with `Intel(R) Xeon(R) CPU E7-2870 @ 2.40GHz` processors, and my personal computer (PC) has `Intel(R) Core(TM) i5-5200U CPU @ 2.20GHz` processors.

Process	Aguia4	PC
IC	5 min	6 min
Hydro	90 min	120 min
50 FOs	< 1 min	~ 1 min

Table 3.1: Average running times for a typical event.

As will be discussed in §5.1, centralities are selected based on the number of participating nucleons, which has a spread in the impact parameter value. Then, for example, sometimes a small b does not correspond to a central window, and the IC is discarded. For the 0-5% class, this happens around twice per IC, and the times in Table 3.1 take it into account. Also, the hydro stage will be faster for lower energy and less central events, so these times should be considered a maximum estimate. Furthermore, since each freeze-out is very quick, I measured the average time it took for 50 freeze-out iterations.

[3]The time it takes to run an algorithm.

3.2 Initialization

The energy-momentum tensor $T^{\alpha\beta}$ and the conserved currents J_i^α are output by NeXus to be used as initial conditions for SPheRIO. However, the four-velocities of these currents are usually not consistent, that is, $J_i^\alpha/J_i^0 \neq J_k^\alpha/J_k^0$ for $i \neq k$. Moreover, the Lorentz boost that makes $J_i^\alpha = (n_i, 0, 0, 0)$ does not make $T^{\alpha\beta}$ diagonal. Besides that, the space components in a diagonalized $T^{\alpha\beta}$ are not always equal, corresponding to anisotropic stress [14]. Such inconsistencies happen because the NeXus output matter is not actually in local equilibrium as required for hydrodynamics.

The way NeXSPheRIO circumvents this issue is by solving the eigensystem

$$T^{\alpha\beta}u_\beta = \epsilon u^\alpha, \tag{3.1}$$

using an eigenvector which satisfies $u \cdot u = 1$. This defines the fields of energy density $\epsilon(x^\alpha)$ and the fluid four-velocity $u^\alpha(x^\beta)$. Then, the number densities are determined by

$$n_i = J_i^\alpha u_\alpha. \tag{3.2}$$

With (ϵ, n_B), the other thermodynamic quantities are computed using the EoS. Using this procedure, the system is forcibly thermalized by construction, but it does not conserve energy and momentum [65]. This leads to some error in the spatial distribution of energy (and maybe in baryon density), which is dealt with in §5.1.2.

3.3 Smoothed hydrodynamics

The hydrodynamical evolution at the second step of NeXSPheRIO is carried out using the *Smoothed Particle Hydrodynamics*, or SPH for short. It is a numerical mesh-free method originally developed for astrophysical purposes [66, 67], later adapted to HIC simulations [68], that solves the equations of motion in a Lagrangian description of the flow: a continuous fluid is interpolated through a discrete set of fluid parcels – referred to as SPH particles – that move over time carrying relevant quantities around. Here, I describe the general idea behind the method, the variational procedure that provides the equations of motion (2.3) in SPH form, as well as the Cooper-Frye formula (2.18) within the scheme.

Let A be a thermodynamical extensive variable, such as entropy, baryon number or specific volume. In the space-fixed "lab" frame, its density is a continuous field $a^*(\vec{r},t)$ compactly supported over spacetime, so we can write the spatial identity

$$a^*(\vec{r},t) = \int \mathrm{d}V a^*(\vec{r}',t)\delta^3(\vec{r}-\vec{r}'), \tag{3.3}$$

with integration over primed variables. The *smoothing* part of SPH refers to replacing the Dirac delta distribution with a chosen *kernel* function $W(\vec{r};h)$ that converges to the delta in the limit $h \to 0$:

$$a^*(\vec{r},t) \simeq \int \mathrm{d}V a^*(\vec{r}',t)W(\vec{r}-\vec{r}';h),$$

and the *particle* (discretization) part stands for dividing the fluid in N parcels:

$$a^*(\vec{r},t) \simeq a^*_{\mathrm{SPH}}(\vec{r},t) = \sum_{j=1}^{N} \Delta V_j^*\ a^*(\vec{r}_j,t)W(\vec{r}-\vec{r}_j;h), \tag{3.4}$$

where the j^{th} SPH particle is positioned at $\vec{r}_j$ and occupies a (small) volume ΔV_j^*. Intuitively, the SPH approximation should converge as the number of interpolation points N grows larger, which is guaranteed [69] if the smoothing length h decreases with N, for a well-behaved (positive definite) kernel. Nice symmetric choices of W include a normalized Gaussian or a polynomial spline, illustrated in Fig. 3.2.

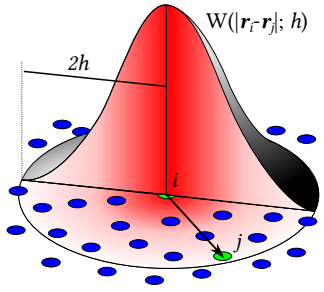

Figure 3.2: Schematics of a symmetric kernel W in a plane. Adapted from [70].

If the system has a conserved extensive quantity – *e.g.* the total entropy in ideal hydro – S, it can be distributed among the SPH particles so that

$$S = \sum_{j=1}^{N} \nu_j, \tag{3.5}$$

with ν_j regarded as the S-charge of the j^{th} particle. Then the *reference* density $\sigma_j^* \equiv \sigma^*(\vec{r}_j)$ of S gives a natural volume ΔV_j^* for the particle (in the space-fixed frame), since

$$\sigma^*(\vec{r}) = \frac{\mathrm{d}S}{\mathrm{d}V} \Longrightarrow \Delta V_j^* = \frac{\nu_j}{\sigma_j^*}. \tag{3.6}$$

It is important to note that the ν's are constant throughout the evolution, and can

be interpreted as the S-charge in the corresponding particle, whereas the σ^*'s change with time. Replacing (3.6) in (3.4) gives the so-called SPH approximation, used in most literature and in this work:

$$\boxed{a^*_{\mathrm{SPH}}(\vec{r},t) = \sum_{j=1}^{N} \nu_j \frac{a^*(\vec{r}_j,t)}{\sigma^*_j} W(\vec{r}-\vec{r}_j;h)} \tag{3.7}$$

This sum is used to compute most hydrodynamical quantities of interest, and a^*_{SPH} is said to be the *smoothed* version of a^*. In the following, I will drop the "SPH" label of smoothed quantities for convenience. In particular, the densities $a^*_i \equiv a^*(\vec{r}_i,t)$ at the SPH particles are also updated at every time step using (3.7):

$$a^*_i = \sum_{j=1}^{N} \nu_j \frac{a^*_j}{\sigma^*_j} W(\vec{r}-\vec{r}_j;h), \tag{3.8}$$

which makes the computation of conserved densities σ^*_j convenient, by replacing a^*_j:

$$\sigma^*_i = \sum_{j=1}^{N} \nu_j W(\vec{r_i}-\vec{r}_j;h). \tag{3.9}$$

Among the possible choices of conserved density, entropy never vanishes in the interesting regions of the QCD phase diagram [14], justifying its use as the reference density in this work. Another reasonable choice is the energy density, which is in fact implemented in NeXSPheRIO. Nevertheless, every conserved quantity has a charge similar to ν carried around by the SPH particles, and the density is computed in the same fashion as (3.9). For instance, each particle j carries a baryon charge b_j, and the baryon density is computed as

$$n^*_B(\vec{r},t) = \sum_{j=1}^{N} b_j W(\vec{r}-\vec{r}_j;h), \tag{3.10}$$

One main strength of SPH is that the dependence on $\vec{r}$ in the r.h.s. of (3.7) is only on the argument of W, so spatial derivatives are translated into analytic derivatives of the kernel. Another advantage is that global conservation is automatic, since each SPH particle carries a constant portion of the conserved quantities throughout the evolution.

3.3.1 Equations of Motion

The relativistic hydrodynamic equations (2.3) and (B.9) are applied to thermodynamical fields, which amount to relatively few degrees of freedom. Even with the SPH approximation (3.7), it is not entirely clear how to directly translate them into equations of motion for SPH particles [68], so a systematic approach is needed. Such translation can be provided by the variational principle, finding a suitable action that generates the thermodynamical EoMs when minimized. This approach works because the corresponding Lagrangian density could then be directly approximated by (3.7).

It turns out [71] that the energy density ϵ is an appropriate Lagrangian density, so the Lagrangian corresponding to the system of SPH particles $\{\vec{r}_j, \dot{\vec{r}}_j\}$ in the space-fixed frame can be written as

$$L(\{\vec{r}_j, \dot{\vec{r}}_j\}) = -\sum_{j=1}^{N} \nu_j \sqrt{-g_j} \left[\frac{\epsilon(x_j^\alpha)}{\sigma_j^*}\right] = -\sum_{j=1}^{N} \left(\frac{E_j}{\gamma_j}\right), \tag{3.11}$$

where $\sqrt{-g}$ is the Jacobian determinant of the coordinate system, $E_j = \epsilon_j \Delta V_j = \epsilon_j \nu_j / \sigma_j$ is the "rest energy" of particle j, and $\sigma^* = \sqrt{-g}\gamma\sigma$. In Milne coordinates $x^\alpha = (\tau, \vec{r}_T, \eta)$, with invariant volume $\sqrt{-g}\,\mathrm{d}^4x = \tau\,\mathrm{d}\tau\,\mathrm{d}^2r_T\,\mathrm{d}\eta$, the corresponding action (see Appendix §B.2) is

$$I = -\int \mathrm{d}\tau \sum_{j=1}^{N} \left(\frac{E_j}{\gamma_j}\right). \tag{3.12}$$

Minimization of this action leads to the equations of motion for the SPH particle i

$$\frac{\mathrm{d}\vec{r}_i}{\mathrm{d}\tau} = \vec{v}_i, \tag{3.13}$$

$$\frac{\mathrm{d}\vec{\pi}_i}{\mathrm{d}\tau} = -\tau \sum_{j=1}^{N} \nu_i \nu_j \left[\frac{P_i}{(\sigma_i^*)^2} + \frac{P_j}{(\sigma_j^*)^2}\right] \nabla_i W_{ij}, \tag{3.14}$$

where the relativistic 3-momentum[4] $\vec{\pi} = (\vec{\pi}_T, \pi_\eta)$ has the transversal component related to the velocity $\vec{v}_T = \dot{\vec{r}}_T$ by

$$\vec{\pi}_T = \nu\gamma^2 \left(\frac{P+\epsilon}{\sigma^*}\right) \vec{v}_T, \tag{3.15}$$

[4]Omitting the particle label i for readability.

and the longitudinal component is

$$\pi_\eta = \nu\tau\gamma^2 \left(\frac{P+\epsilon}{\sigma^*}\right) v_\eta. \tag{3.16}$$

The equations above constitute a system of coupled ODEs that are numerically solved in SPheRIO using the 2$^{\text{nd}}$-order Runge-Kutta (RK2) method [72]. A single time step is outlined below:

At a given proper time τ, the system is in a configuration of particles $\{\vec{r}_j, \dot{\vec{r}}_j\}$. The baryon and entropy densities $(\sigma^*, n_B^*)_i$ are calculated for each particle i using (3.9), and then converted to the proper frame multiplying by γ_i. With $(\sigma, n_B)_i$, the other thermodynamic variables (in particular ϵ_i and P_i) are extracted from the equation of state table, and used to compute the variation in 3-momentum, the r.h.s of (3.14). Then, $\vec{\pi}_i$ is updated in RK2 and new velocities $\dot{\vec{r}}_i$ are computed using (3.15) and (3.16). Finally, RK2 updates the positions $\vec{r}_i$ with (3.13) and the time step is complete.

3.3.2 Cooper-Frye in SPH

As described in section §2.3, the final stage of a HIC consists in the decoupling of detectable hadrons from the expanded fluid, sampled according to the Cooper-Frye prescription, with the spectra (2.18), rewritten here as

$$E\frac{\mathrm{d}N}{\mathrm{d}^3p} = \int_\Sigma \mathrm{d}\Sigma_\alpha\, p^\alpha f_\theta(p\cdot u), \tag{3.17}$$

with the distribution (2.15). Since in NeXSPheRIO the fluid is represented by the set of SPH particles, the Cooper-Frye formula must be carefully expressed within the SPH formalism. Similarly to (3.4) and (3.11), the integral over an isotherm Σ is approximated by the sum

$$E\frac{\mathrm{d}N}{\mathrm{d}^3p} = \sum_{j=1}^{N} (\Delta\Sigma_\alpha)_j\, p^\alpha f_\theta(p\cdot u_j), \tag{3.18}$$

where each SPH particle j occupies its own oriented hypersurface element $(\Delta\Sigma_\alpha)_j$, which can be computed in the following way: in the proper frame R, it contains only a non-zero time component, so the identification $|(\mathrm{d}\Sigma_j)_R| = |(\mathrm{d}\Sigma_j^0)_R| = \Delta V_j$ with the proper volume

(3.6) is immediate [58, 63]. Through a Lorentz transformation (B.1),

$$\Delta\Sigma_j^\alpha = (\Lambda_\beta^\alpha \, \mathrm{d}\Sigma_R^\beta)_j = (\Lambda_0^\alpha \, \mathrm{d}\Sigma_R^0)_j = (u^\alpha \, \mathrm{d}\Sigma_R^0)_j.$$

Contraction with $(u_\alpha)_j$ yields $(\mathrm{d}\Sigma_j^0)_R = u_j \cdot \Delta\Sigma_j$. Furthermore, the hypersurface element is perpendicular to the constant temperature surface, so it is proportional to the normal[5] vector $(n_\alpha)_j \equiv \dfrac{\partial_\alpha T(x_j)}{\sqrt{\partial T \cdot \partial T}}$. Hence, writing $\Delta\Sigma_j^\alpha = |\Delta\Sigma_j| n_j^\alpha$,

$$\Delta V_j = |(\mathrm{d}\Sigma_j^0)_R| = |u_j \cdot n_j||\Delta\Sigma_j| \Rightarrow |\Delta\Sigma_j| = \frac{\Delta V_j}{|u_j \cdot n_j|}. \tag{3.19}$$

Finally, the spectra (3.18) is written as

$$\boxed{E\frac{\mathrm{d}N}{\mathrm{d}^3p} = \sum_{j=1}^{N} \frac{\nu_j}{\sigma_j} \frac{p \cdot n_j}{|u_j \cdot n_j|} f_\theta(p \cdot u_j),} \tag{3.20}$$

using the volume element (3.6) with $V = \sqrt{-g}\gamma V^* = \nu_j/\sigma_j$. This distribution is then used as input of a conventional Monte-Carlo sampling algorithm for the realization of hadrons. It is important to stress that this process is done only over the isotherm hypersurface, so the SPH sum in (3.20) only counts the particles when they have the freeze-out temperature T_{FO}, fixed in f_θ at input. Moreover, as mentioned in §2.3, the negative contributions with $p^\alpha \, \mathrm{d}\Sigma_\alpha < 0$ are neglected. Here, this means that only the terms with positive $p_j \cdot n_j > 0$ enter the sum.

3.4 Decays

After the freeze-out sampling described above, the SPheRIO code returns in the form of a list of hadrons to NeXus, which handles the resonance decays with probabilities equal to the decay rates provided by the Particle Data Group [64].

In the `.optns` file, it is possible to switch off some decays. This is useful for comparisons with experimental data, which is often presented after reconstruction of tracks [73,74] with some efficiency. Section §4.3.3 discusses the effects of decays for this work.

[5] Here, *normal* means both "perpendicular to" and "absolute value of one". Just a language curiosity.

Chapter 4

Cumulants in Hydro

As discussed in the Ch. 1, some of the promising signs in the search for the location of the QCD Critical End Point (CEP) are the event-by-event fluctuations of conserved quantities such as net-baryon number and electric charge. Theoretically, these fluctuations are related to thermodynamical susceptibilities, defined in (1.2). Experimentally, they appear as the cumulants of the distributions of said conserved quantities [29].

In this chapter, I will present how to translate the susceptibilities into cumulants, discuss the problems with computing them in a hydrodynamical simulation, and propose a statistics-based method to workaround these problems, discussing some important elements and assumptions.

4.1 Cumulants

The critical end-point lies at the end of the 1^{st}-order transition line, as seen in Fig. 2.5. A model independent feature of QCD is that, near the CEP, the conserved charge susceptibilities (1.2) such as Fig. 1.5 have the profile of a sharp mountain [35] in the phase diagram, because the correlation length diverges at any critical point. Although they can be easily extracted from the equation of state, comparison to data is not trivial, because the thermodynamical variables are not directly measurable, since the experiment can only access the final state of the system at or after freeze-out [16, 29]. Then, to map the phase diagram, a "scan" over control parameters is made[1], since the center-of-mass

[1] This gives the name to the *Beam Energy Scan* experiments.

energy $\sqrt{s}$ and the centrality $\mathcal{C}$ correlate well with μ_B. Scanning in the former yields a large variation in baryon potential, while the latter can provide fine-tuning [34].

Provided that the freeze-out happens soon after the transition, the emitted particles do not interact much, so their momenta are (aptly) frozen. If that is the case, the spikes in susceptibilities χ_n of a particular species X (whose antiparticle is denoted by $\bar{X}$) will be reflected in the shape of distributions of the corresponding particles via the relation (see Appendix A.2)

$$C_n = VT^3\chi_n, \tag{4.1}$$

where V and T are the volume and temperature of the system and C_n is the n^{th} cumulant of the probability distribution [29], defined as a Maclaurin coefficient in the *Cumulant Generating Function*

$$\text{CGF}_X(z) \equiv \ln\langle\exp(zX)\rangle = \sum_{n=0}^{\infty} C_n \frac{z^n}{n!}. \tag{4.2}$$

That is, the cumulant of order n is the n^{th} derivative of $\text{CGF}(z)$ computed at $z = 0$. For example, $C_1^X = \langle X\rangle$ is the mean value M, $C_2^X = \langle X^2\rangle - \langle X\rangle^2$ is the variance σ^2, an so on, where X inside brackets denotes the number of X particles counted for a single collision in a small acceptance window of rapidity and transverse momenta, depending on the detector specificities.

So as to eliminate the dependence on volume and temperature in (4.1), ratios of different cumulants are constructed, which allows for comparison between theory and experiment. A problem with higher-order cumulants is that they are very sensitive to one another: a small shift in the variance C_2 will greatly impact C_4. Then, the normalized quantities[2] of skewness S and kurtosis κ are defined as

$$S = \frac{C_3}{C_2^{3/2}} \quad \text{and} \quad \kappa = \frac{C_4}{C_2^2}. \tag{4.3}$$

In the following, S and κ will be implicit whenever mentioning cumulants, unless specified otherwise.

[2] Also called standardized moments of the distribution, but there is no need to add another name.

4.2 The problem

The analysis of fluctuations depends on event-by-event measurements of particle multiplicities. Therefore, a higher-order cumulant will be more sensitive to the effects of limited statistics. Unsurprisingly, a very large sample is needed for acceptable confidence intervals. For central Au+Au collisions at 200 GeV, a 5% deviation from the true value of net-proton C_4 requires a sample size of around 10^6 in baseline estimates [75], about the same number STAR uses in cumulant analysis [74, 76, 77]. Using one node of Aguia4, the runtimes from Table 3.1 indicate that one million NeXSPheRIO simulations in this event configuration **would take around 180 years!** Using the 40 Aguia4 nodes uninterruptedly, this corresponds to 4 and a half years. On top of that, checking the effects of deviations from ideal hydrodynamics – for example, baryon diffusion and viscosity – would demand an even larger statistic. Even with a lot of potent computers and a very efficient code, the time complexity of full $(3+1)$D hydrodynamics is simply too high, which may be one reason that – to my knowledge – no work on hydro-based cumulants has been published so far.

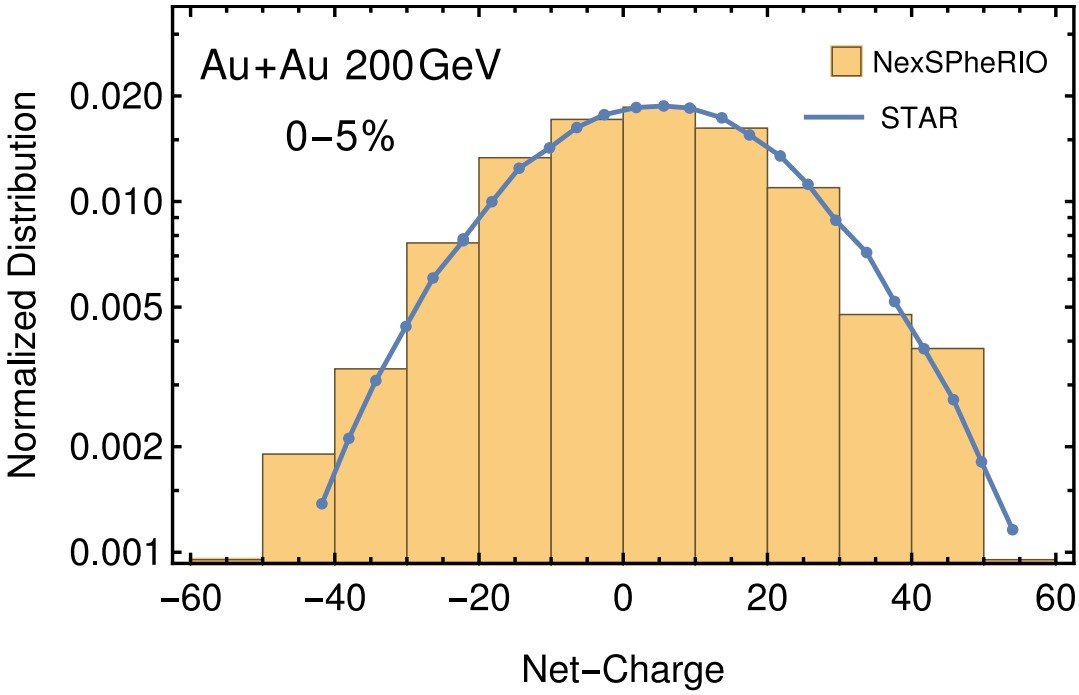

Figure 4.1: Event-by-event distribution of net-electric charge at midrapidity ($|y| < 0.5$) for central Au+Au collisions at 200 GeV, with transverse momentum cut $0.2 < p_T < 2$ GeV/c. The histogram is for 5000 NeXSPheRIO simulations with one freeze-out and the blue line is STAR data [76].

Cumulant	STAR	NeXSPheRIO
M	4.49 ± 0.01	2.8 ± 0.2
$\sqrt{\sigma^2}$	18.95 ± 0.02	20.2 ± 1.3
S	-0.001 ± 0.006	-0.1 ± 0.5
κ	0.007 ± 0.017	0.3 ± 0.6

Table 4.1: Comparison between the cumulants of the distributions in Fig. 4.1. Errors for NeXSPheRIO computed with jackknife re-sampling [78]. See footnote 6 in Ch. 5.

To paint a picture of what happens at low statistics, Fig. 4.1 shows the net-charge histogram resulting from 5000 NeXSPheRIO simulations compared to STAR data, whose cumulants are presented in Table 4.1. An event only goes through one freeze-out, as it would in a real-life collision, and the net electric charge is computed for each event, which forms the histogram. Then, the cumulants are computed with the usual expressions [29]. Even though the values of higher-order cumulants are compatible within the error bars, the lack of precision renders these results meaningless. This is the problem I try to solve[3], or at least circumvent, with the method described in the next section.

4.3 The workaround

The fluctuations of particle number in a HIC simulation originate in three separate processes, if the modularization described in Ch. 1 is considered[4]. (I) The initial profiles (of energy and baryon density) change for similar events, *i.e.* events in the same energy and centrality class; (II) the Cooper-Frye sampling results in distinct distributions for the same freeze-out hypersurface, and (III) decays are probabilistic. The hydrodynamic evolution, being comprised of numerical solving of differential equations, is *completely deterministic*. It is also the stage with the largest time complexity, so it would be advantageous to have a method that reduces the amount of hydro simulations needed in order to achieve a reasonable precision.

The event-by-event average in (4.2) is twofold: the average over the N_{FO} freeze-out iterations for each collision (including the decays), denoted by FO; and the average over different initial conditions (or events) in the same centrality class, denoted by IC. Then,

[3]As will be seen in Ch. 5, the discrepancy in the mean value is not due to low statistics, but problems with modelling, which the method alone is not able to correct.

[4]Fluctuations during the hydrodynamic expansion (*thermal noise*) have been studied for example in [79–81]. This seems to be a subdominant effect, compared to the contributions described; nevertheless, they should be studied later.

the CGF of X is divided as

$$\mathrm{CGF}_X(z) = \ln \left\langle \left\langle e^{zX} \right\rangle_{FO} \right\rangle_{IC} . \tag{4.4}$$

Here enters the main idea behind the method: once the freeze-out distribution is known, the inner average can be computed analytically (see below) and the corresponding fluctuations are taken into account. This means that only the effects of varying the initial condition will need to be estimated numerically, consequently reducing the number of hydro events to achieve a reasonable precision.

4.3.1 An example

As discussed in §2.3, the sampling of most particles at freeze-out follows a Poisson distribution, so $X \sim \mathrm{Pois}(\lambda)$ and the FO average of CGF_X is computed as

$$\begin{aligned} \left\langle e^{zX} \right\rangle_{FO} &= \sum_{x=0}^{\infty} e^{zx} \Pr(X = x; \lambda) = \sum_{x=0}^{\infty} e^{zx} \frac{\lambda^x}{x!} e^{-\lambda} = e^{-\lambda} \sum_{x=0}^{\infty} \frac{(\lambda e^z)^x}{x!}, \\ &= \exp[\lambda(e^z - 1)], \end{aligned} \tag{4.5}$$

where $\Pr(X = x; \lambda)$ is the probability of having x particles at freeze-out, with average $\lambda \equiv \langle X \rangle_{FO}$. Furthermore, using a bar to denote the antiparticle $\bar{X}$ and its related quantities, the *net*-particle number $\Delta = X - \bar{X}$ follows a Skellam distribution, with

$$\left\langle e^{z\Delta} \right\rangle_{FO} = \left\langle e^{zX} \right\rangle_{FO} \left\langle e^{-z\bar{X}} \right\rangle_{FO} = \exp\left[\lambda(e^z - 1) + \bar{\lambda}(e^{-z} - 1) \right], \tag{4.6}$$

where the first equality holds if the emission of each particle type is independent. Finally, the event-by-event CGF of Δ for a Poissonic freeze-out is

$$\mathrm{CGF}_\Delta(z) = \ln \left\langle \lambda(e^z - 1) + \bar{\lambda}(e^{-z} - 1) \right\rangle_{IC} . \tag{4.7}$$

Then, the cumulants C_n^Δ can be directly evaluated via (4.2) and (4.7). For example,

$$\begin{aligned} C_1^\Delta &= \frac{\mathrm{d}}{\mathrm{d}z} \mathrm{CGF}_\Delta(z) \Big|_{z=0}, \\ &= \left. \frac{\left\langle \lambda e^z - \bar{\lambda} e^{-z} \right\rangle_{IC}}{\left\langle \lambda(e^z - 1) + \bar{\lambda}(e^{-z} - 1) \right\rangle_{IC}} \right|_{z=0}, \\ &= \left\langle \lambda - \bar{\lambda} \right\rangle_{IC} . \end{aligned} \tag{4.8}$$

The subsequent higher-order cumulants can be derived in the same straightforward manner, which yields

$$C_2^\Delta = \left\langle q^2 \right\rangle_{IC} - \langle q \rangle_{IC}^2 + \langle n \rangle_{IC} \,; \tag{4.9}$$

$$C_3^\Delta = \left\langle q^3 \right\rangle_{IC} + \langle q \rangle_{IC} \left[1 - 3 \left\langle q^2 \right\rangle_{IC}\right] + 2 \langle q \rangle_{IC}^3 + 3 \left[\langle qn \rangle_{IC} - \langle q \rangle_{IC} \langle n \rangle_{IC}\right] ; \tag{4.10}$$

$$\begin{aligned} C_4^\Delta = {} & \left\langle q^4 \right\rangle_{IC} - 3 \left\langle q^2 \right\rangle_{IC} \left[\left\langle q^2 \right\rangle_{IC} - 4 \langle q \rangle_{IC}^2\right] - 4 \left\langle q^3 \right\rangle_{IC} \langle q \rangle_{IC} - 6 \langle q \rangle_{IC}^4 + \\ & + 4 \left[\left\langle q^2 \right\rangle_{IC} - \langle q \rangle_{IC}^2\right] + 3 \left[\left\langle n^2 \right\rangle_{IC} - \langle n \rangle_{IC}^2\right] + \langle n \rangle_{IC} + \\ & + 6 \left[\left\langle nq^2 \right\rangle_{IC} - 2 \langle nq \rangle_{IC} \langle q \rangle_{IC} + 2 \langle n \rangle_{IC} \langle q \rangle_{IC}^2 - \langle n \rangle_{IC} \left\langle q^2 \right\rangle_{IC}\right] ; \end{aligned} \tag{4.11}$$

and so on, defining the freeze-out charge $q \equiv \lambda - \bar{\lambda} = \left\langle X - \bar{X} \right\rangle_{FO}$ and the freeze-out multiplicity $n \equiv \lambda + \bar{\lambda} = \left\langle X + \bar{X} \right\rangle_{FO}$ of each event. To obtain the cumulants of X alone, setting $\bar{\lambda} = 0$ above gives the correct expressions. Furthermore, this can also be applied to a collection of particles, such as baryons or charged particles.

This work analyzes the net-proton number, labeled by $p, \bar{p}$; and the net-electric charge, labeled by $\pm$ and composed of protons, charged pions and charged kaons.

4.3.2 Number of Freeze-Outs

The *averages* λ and $\bar{\lambda}$ are the only values from the freeze-out distribution used in the cumulants, so the number N_{FO} of freeze-out iterations is determined from the error in λ, the relative deviation of the mean, defined as $\delta_\lambda = \tilde{\sigma}_X / (\lambda \sqrt{N_{FO}})$, with the standard deviation $\tilde{\sigma}_X$ of X in the freeze-out. Then, the N_{FO} needed is

$$N_{FO} \geq \left(\frac{\tilde{\sigma}_X}{P\lambda}\right)^2 \tag{4.12}$$

for all particles X of interest, where P is the desired value of δ_λ.

This can be better visualized by plotting δ_λ versus N_{FO}, as in Fig. 4.2, and taking enough freeze-out iterations to guarantee a small δ_λ. With a threshold of 0.01% in relative deviation, $N_{FO} \sim 4000$ freeze-out iterations are required. For the results of this work, I set $N_{FO} = 5000$ just to be sure, since it does not cost much in computation time.

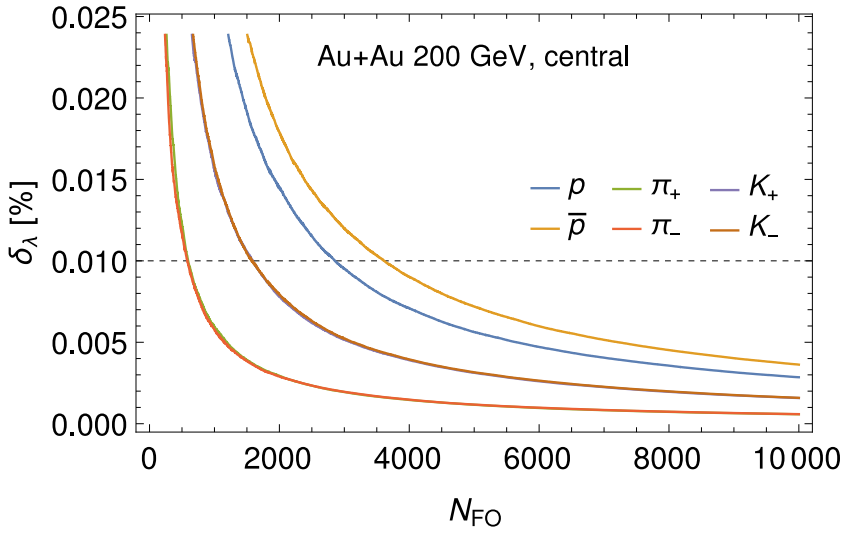

Figure 4.2: Relative deviation of λ for different particle species decreasing with N_{FO} in one central Au+Au 200 GeV collision. Antiprotons $\bar{p}$ have the largest δ_λ, π_+ and K_+ overlap with π_- and K_- respectively.

4.3.3 Effect of decays

Some care must be taken if resonance decays are allowed in the simulation, since they may introduce correlations among siblings, that is, particles resulting from the same decay. An easy way to check this is to compare a Poisson distribution with parameter λ to the histogram of particle number across freeze-out iterations, using different decay configurations, which is exemplified in Fig. 4.3.

The default of NeXSPheRIO, represented by the configuration "*dall*", is to allow all decays with probabilities from PDG [64], but often experimental groups reconstruct the primary vertices [82], which in the simulation amounts to turning off the corresponding decays. As a baseline, configuration "*dnon*" blocks every decay, so it is the closest to an uncorrelated freeze-out.

The last configuration, "*dfer*[5]", prohibits the decay of Λ, $\pi_\pm$, π_0, and K_S, as well as their antiparticles, and all other hadrons may decay. In particular, the protons that come from decays of Λ baryons are not included in the proton count in experiment; decays of K^0_S into $\pi_\pm$ are reconstructed [73]; these charged pions have a long mean lifetime and do not decay during a HIC; and π_0 only decays into photons, which are not useful for this thesis. Therefore, this is the configuration used in the present work, and it does not seem to significant affect the freeze-out distribution.

[5]In tribute to Dr. Fernando Gardim.

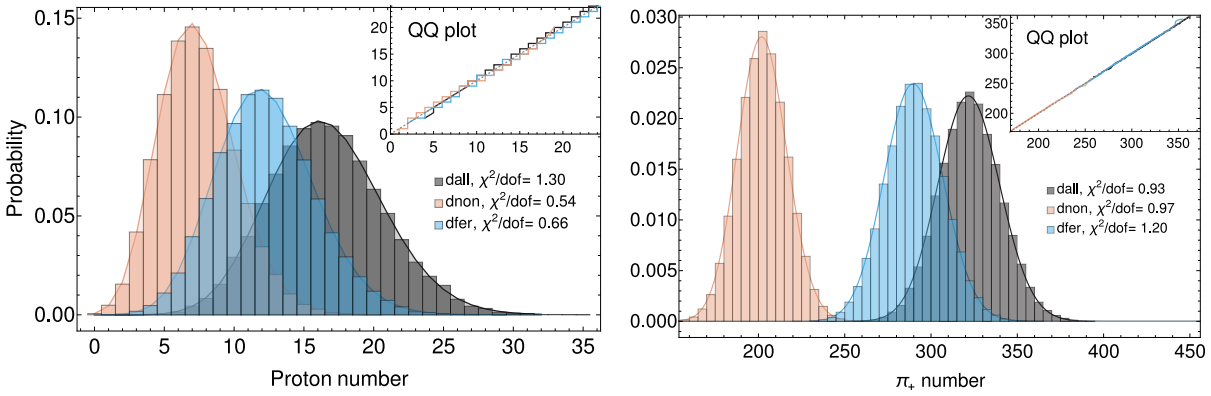

Figure 4.3: Freeze-out histogram of (a) protons and (b) π_+ in different decay configurations, for the same initial condition. Each histogram has an average λ, which is used as the parameter of a Poisson distribution represented by the curves. A quantile-quantile (QQ) plot confirms no tendency and the χ^2-test show the goodness of Poisson fits. The different configurations are defined in the main text.

4.3.4 Acceptance cuts

The cumulants (4.8) through (4.11) were found with the assumption that particles are emitted independently, hence follow a Poisson distribution. This applies when considering the full phase space, but it is not the case in experiments that measure particles in a restricted (y, p_T) window, since global conservation laws generate correlations between particles *inside* the acceptance window with the ones *outside*.

A simple way to take this into account is to replace the Poisson distribution with a binomial, with the following picture in mind: the particle is either inside the acceptance window, with probability p; or outside it, with probability $(1-p)$, which clearly points to a binomial distribution. A good estimate for p is the ratio λ/M of mean particle number λ inside the window by the mean total multiplicity M in the phase space. Then, $X \sim \text{Bin}\left(M, \dfrac{\lambda}{M}\right)$. Fig. 4.4 shows the goodness of a binomial fit in proton and antiproton yield at freeze-out, with the *dfer* decay configuration, in the (y, p_T) window used by STAR cumulants [74, 82]. Similar plots can be made for other species, they all fit a binomial reasonably well.

Such replacement changes the expressions for cumulants, because now the freeze-out average (4.5) reads

$$\begin{aligned}\left\langle e^{zX}\right\rangle_{FO} &= \sum_{x=0}^{\infty} e^{zx}\Pr\left(X=x;M,x\right) = \sum_{x=0}^{\infty} e^{zx}\binom{M}{x}p^x\left(1-p\right)^{M-x}, \\ &= \left(1-p+pe^z\right)^M,\end{aligned} \tag{4.13}$$

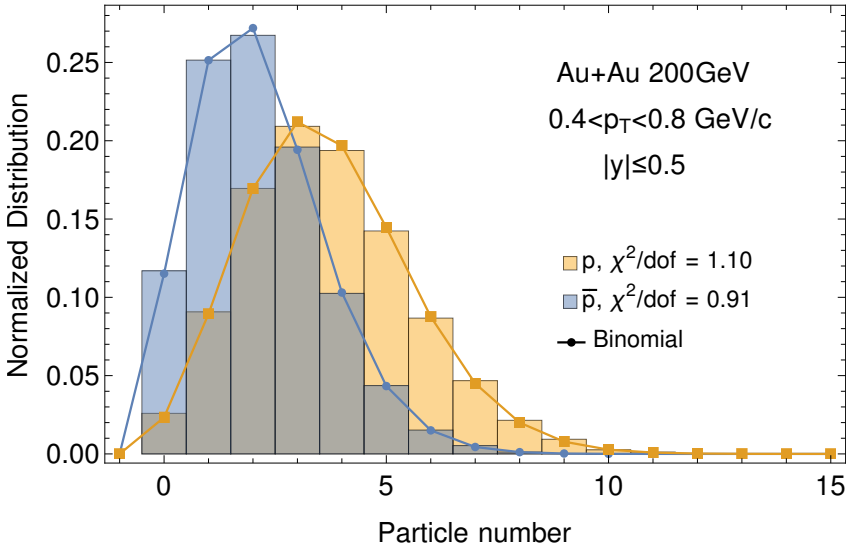

Figure 4.4: Histogram of proton (in orange) and antiproton (in blue) number in the acceptance window $|y| < 0.5$, $0.4 < p_T < 0.8$ GeV/c, compared to the binomial fits with appropriate χ^2.

with $\Pr(X = x; M, p)$ as the probability that, out of M particles, a fraction $p = \dfrac{\lambda}{M}$ is inside an acceptance window. Then, the CGF becomes

$$\mathrm{CGF}_X(z) = \ln \left\langle (1 - p + pe^z)^M \right\rangle_{IC}, \tag{4.14}$$

so the corresponding cumulants for $\Delta = X - \bar{X}$ follow from the definition (4.2) with the first equality in (4.6). Using $q = \lambda - \bar{\lambda}$ and $n = \lambda + \bar{\lambda}$ again,

$$C_1^\Delta = \langle q \rangle ; \tag{4.15}$$

$$C_2^\Delta = \langle q^2 \rangle - \langle q \rangle^2 + \langle n \rangle - \langle s_{1,1}^+ \rangle ; \tag{4.16}$$

$$\begin{aligned} C_3^\Delta = {} & \langle q^3 \rangle + \langle q \rangle - 3 \langle q \rangle \langle q^2 \rangle + 2 \langle q \rangle^3 + 3 \big[\langle qn \rangle - \langle q \rangle \langle n \rangle \big] + \\ & + 3 \langle q \rangle \langle s_{1,1}^+ \rangle + 2 \langle s_{1,2}^- \rangle - 3 \langle s_{2,1}^- + s_{1,1}^- - \lambda\bar{\lambda} s_{0,1}^- \rangle ; \end{aligned} \tag{4.17}$$

$$\begin{aligned} C_4^\Delta = {} & \langle q^4 \rangle + 4 \langle q^2 \rangle - 6 \langle q \rangle^4 + 6 \langle q^2 n \rangle + 3 \langle n^2 \rangle + \langle n \rangle - 4 \langle q \rangle \langle q^3 + q + 3qn \rangle - \\ & - 3 \langle q^2 + n - s_{1,1}^+ \rangle^2 + 12 \langle q^2 + n - s_{1,1}^+ \rangle \langle q \rangle^2 - \\ & - \langle 7 s_{1,1}^+ - 18 s_{2,1}^+ + 12 s_{1,2}^+ \rangle - \langle 11 s_{2,2}^+ - 6 s_{1,3}^+ - 6 s_{3,1}^+ \rangle + \\ & + 4 \langle q \rangle \langle 3 s_{1,1}^- + 3 s_{2,1}^- - 2 s_{1,2}^- - 3\lambda\bar{\lambda} s_{0,1}^- \rangle + \\ & + \langle \lambda\bar{\lambda} \big[6 s_{0,1}^+ - 8 s_{0,2}^+ + 6 p\bar{p} - (\lambda\bar{p} + \bar{\lambda} p) \big] \rangle ; \end{aligned} \tag{4.18}$$

where I defined a shorthand $s_{a,b}^\pm \equiv \lambda^a p^b \pm \bar{\lambda}^a \bar{p}^b$, and the IC label in averages is omitted for readability. The resonance decays also do not affect the goodness of a binomial fit significantly.

4.4 Some remarks

The method I described here assumes a theoretical distribution for the emission at freeze-out, which allows for analytical expressions of cumulants in terms of IC averages such as (4.8) through (4.11) for a Poisson, and (4.15) through (4.18) for a binomial. However, it may not be possible to describe the freeze-out well enough with a known distribution, or even one that yields too extensive calculations. In these cases, the method can still be applied as follows.

In practice, it is not necessary to actually derive expressions for the cumulants. It is possible, in principle, to determine an empirical $\left\langle e^{zX} \right\rangle_{FO}$ and evaluate the $\mathrm{CGF}_X(z)$ in a symbolic math numerical package, such as Mathematica or ScyPy, and then compute the Maclaurin coefficients to the desired order. This may be the case when a transport model is applied, although I have not tested it.

Furthermore, a caveat is that the first equality in (4.6) assumes that the particle and antiparticle yields are uncorrelated, which is true on NeXSPheRIO and Cooper-Frye based samplings but may not be the case for other codes, depending on the decoupling algorithm used.

The results of cumulants from this method are presented in Ch. 5.

Chapter 5

Results for STAR cumulants

In this chapter, I will describe the systematic calibration I made on NeXSPheRIO, and present the results of cumulants from the method I developed in Ch. 4, comparing them to data from the STAR experiment.

5.1 Calibration

The purpose of a HIC simulation is either to compare theory with experiment or make predictions that will be verified by experiment. To do so, the code needs to reproduce some basic quantities dependent on the specific experimental setup of the data used as a reference. In the case of NeXSPheRIO, these are the pseudorapidity distributions $\mathrm{d}N_{ch} / \mathrm{d}\eta$ and the transverse momentum spectra $\mathrm{d}N_{ch} / \mathrm{d}\eta\, \mathrm{d}p_T$ of charged particles.

Then, some parameters need to be adjusted so that these quantities match data, in the following order: the centrality classes are defined, an η-dependent initial energy correction is applied to fix the pseudorapidity distribution, and the freeze-out temperature is determined using the p_T spectra (see below).

This calibration should be redone whenever altering the collision parameters (center-of-mass energy and ion mass) or comparing to data from a different experiment. Mostly, the procedure described in this section is an update of the one described in [59], better suited to the STAR experiment, with some additional adjustments. The parameters I determined are compiled in Table 5.1, and each one is explained below.

As will be seen below, there are other basic quantities not faithfully reproduced by NeXSPheRIO, so this calibration process may include some other steps in the future.

$\mathcal{C}$	N_{part} (range)	A	B	C	T_{FO} [MeV]
0-5%	304 - 394	1.22	0.30	0.020	128.1
5-10%	258 - 304	1.18	0.55	0.022	129.1
10-20%	188 - 258	1.15	0.70	0.020	131.6
20-30%	136 - 188	1.14	1.20	0.025	134.7
30-40%	98 - 136	1.10	1.25	0.028	138.2
40-50%	67 - 98	0.985	1.90	0.039	142.5

Table 5.1: A summary of the calibration parameters used in this thesis for an Au+Au collision at $\sqrt{200}$ GeV in NeXSPheRIO.

5.1.1 Centrality selection

For a given $\sqrt{s_{NN}}$, the amount of matter colliding in a HIC determines where the system lands in the phase diagram 2.5, and consequently most observables depend on it. Geometrically, this is controlled by the impact parameter b, the distance between the centers of the nuclei. The ions may collide head-on, when the event is called *central*; or they may barely graze each other, in a *peripheral* event; or anything in between. These possibilities are denoted the *centrality* $\mathcal{C}$ of the collision [4, 9]. Fig. 5.1(a) shows the geometric distribution of b.

However, b does not tell the whole story, as the nuclei are not homogeneous hard balls. Quantum fluctuations change the distribution of matter inside them, so collisions with the same b can have different outcomes. In experiments, $\mathcal{C}$ may be defined as the percentile of events with higher multiplicity, often using the multiplicity $\mathrm{d}N_{ch}\,/\,\mathrm{d}\eta$ of charged particles in a pseudorapidity window which depends on the observables of interest [76,77]. As being done in experiments, to improve statistics in each data point, the events are divided in centrality *classes* containing a small range of these percentiles.

In the context of NeXSPheRIO, it is impractical to use multiplicity as a centrality probe, since this would require the hydrodynamical evolution of a lot of events that may have to be thrown away. Instead, with the impact parameter randomly selected from the input b range, NeXSPheRIO computes the number of participating nucleons N_{part} consistent with Monte-Carlo Glauber [84] as seen in Fig. 5.1(a). Then, the events are divided in $\mathcal{C}$ classes as in experiment. Intuitively, if there are 100 events, the 5 with highest N_{part} compose the 0-5% class, the next 5 compose the 5-10%, and so on. Moreover, this division is important because, with it, focus can be given to specific centralities, by only evolving initial conditions that fall inside the desired class.

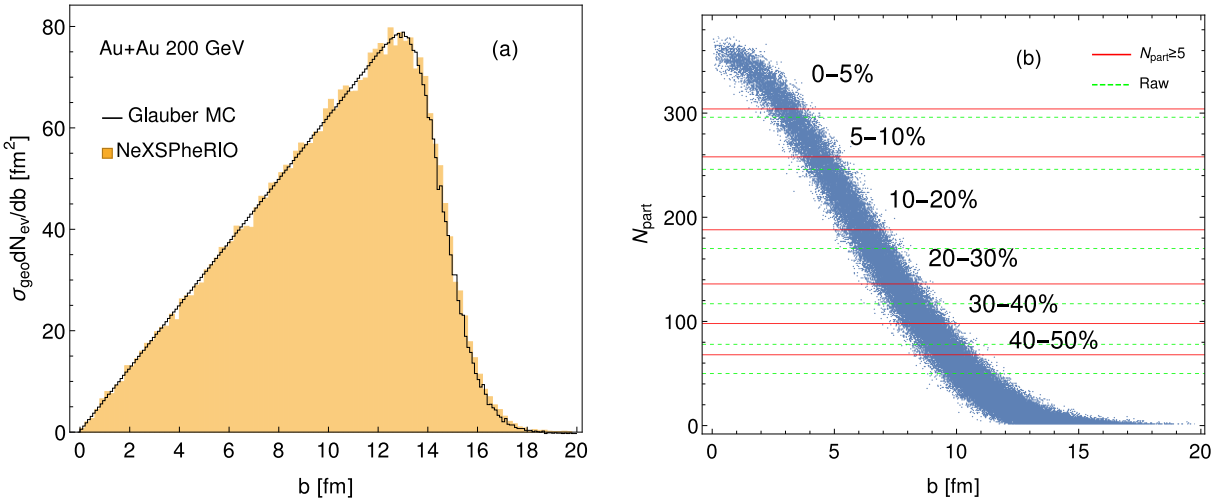

Figure 5.1: (a) The differential geometric cross-section as a function of b. The black line is from Glauber-MC calculations taken from [83] and the histogram is the probability from 5000 NeXus initial conditions, multiplied by the geometric cross-section $\sigma_{geo} = 6847$ mb. (b) The correlation between participant number and impact parameter, with the different centrality classes shown for no trigger ("Raw", in green) and with the $N_{\text{part}} \geq 5$ trigger (in red).

However, the average N_{part} in each class from NeXSPheRIO simulations seems significantly lower than reported by STAR [77], so to reduce this difference I imposed a trigger of $N_{\text{part}} \geq 5$, which eliminates a lot of ultraperipheral events. A possible reasoning for this is that these events have a very low multiplicity, so some end up undetected (in real life as well). Fig. 5.1(b) shows the effect of this trigger in the centrality classes. The classes are shifted up, and particularly, the mean value of participant number increases by ~ 5 in central classes and ~ 20 in the more peripheral ones.

In practice, an input of NeXSPheRIO is the b range, which can be determined for each class using Fig. 5.1(b): for example, the range of 5-10% events is $b \in [1.62, 5.54]$ fm, so this is the input for the `.optns` file described in §3.1. However, there is a spread in the plot and values of b are not one-to-one with N_{part}, for instance, $b = 4$ can correspond to an event in the 0-5%, 5-10% or 10-20% classes. Then, the initial conditions are generated, but only the ones with $N_{\text{part}} \in [258, 304]$ are accepted and used to run the hydrodynamic evolution. A comparison of NeXSPheRIO and STAR [77] centrality classes is shown in Table 5.2. The b ranges are very different, but what matters for the classification is N_{part}, which is consistent for all classes, since the mean values from STAR fall within the ranges from NeXSPheRIO.

$\mathcal{C}$	NeXSPheRIO		STAR	
	N_{part} (range)	b [fm] (range)	N_{part} (mean)	b [fm] (range)
0-5%	304 - 394	0 - 4.8	350.6±2.4	0 - 3.31
5-10%	258 - 304	1.6 - 5.5	298.6±4.1	3.31 - 4.66
10-20%	188 - 258	3.2 - 7.3	234.3±4.6	4.66 - 6.61
20-30%	136 - 188	5.0 - 9.2	167.6 ±5.4	6.61 - 8.10
30-40%	98 - 136	6.1 - 10.2	117.1±5.2	8.10 - 9.33
40-50%	67 - 98	6.9 - 11.4	78.3±5.3	9.33 - 10.5

Table 5.2: Comparison between the participant numbers and impact parameter ranges for NeXSPheRIO and STAR experiment for a 200 GeV Au+Au collision.

5.1.2 Energy loss correction

As mentioned in §3.2, the translation from NeXus out-of-equilibrium output to a diagonal $T^{\mu\nu}$ requires forcing the system into equilibrium. This procedure introduces some errors in the distribution of energy [65], and then must be corrected by hand[1]. Such error is reflected in particle production, as seen in the pseudorapidity distribution of charged particles in Fig. 5.2. Here, the reference experiment STAR only provides $\mathrm{d}N_{ch}\,/\,\mathrm{d}\eta$ at midrapidity ($\eta = 0$), so I used BRAHMS data instead[2].

Independently of the causes of this problem, a phenomenological correction can be made by multiplying the *initial* energy density by an η-dependent function, named the *R-factor*. This dependence comes from observing the uncorrected ("Original") distribution in Fig. 5.2: the shape of $\mathrm{d}N_{ch}\,/\,\mathrm{d}\eta$ is qualitatively similar to the BRAHMS data [86], but higher in forward rapidities and lower at midrapidity. Then, the R-factor can be parametrized with

$$R(\eta) = \frac{A}{\exp\left[10^3(|\eta| - B)\right] + 1} + \frac{A\exp\left[-C(|\eta| - B)^2\right]}{\exp\left[-10^3(|\eta| - B)\right] + 1}, \tag{5.1}$$

where A, B and C are parameters to be determined. Using $A = 1.11$, $B = 0.3$ and $C = 0.02$ yields an appropriate $dN/d\eta$ to compare with BRAHMS data. However, the systematic errors, in the form of differences in detector calibration, make it so that BRAHMS and STAR disagree at midrapidity [77, 86]. Although compatible within error bars, it is best to calibrate NeXSPheRIO to the STAR values, since they will be used for

[1] The $\mathrm{d}N_{ch}\,/\,\mathrm{d}\eta$ extracted directly from NeXus, that is, without a forced thermalization, is in good agreement with experimental data [85].

[2] The distributions by PHOBOS are also consistent with this within systematic uncertainty, but the centrality classes are different, with 0-6%, 6-15% and so on.

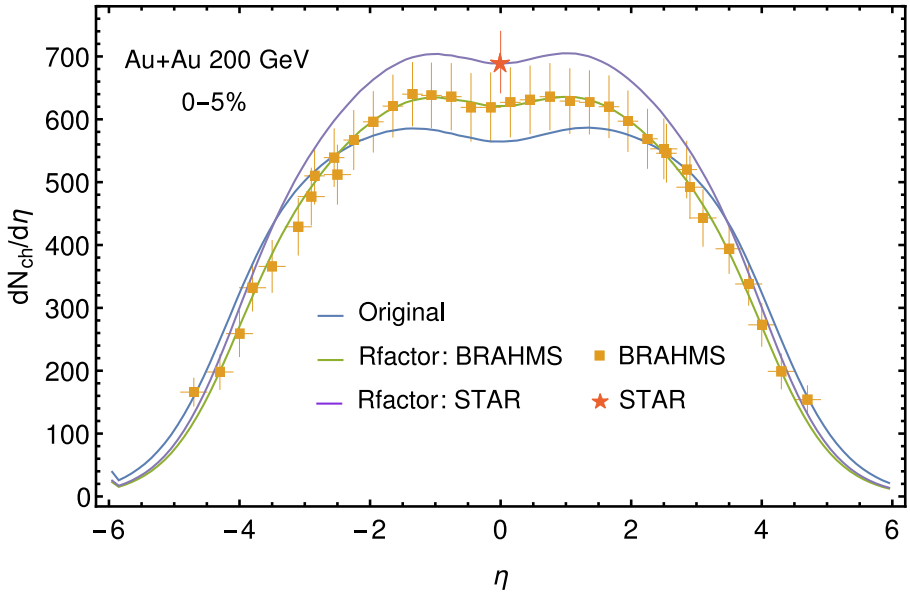

Figure 5.2: Pseudorapidity distributions of charged particles in a central Au+Au collision at 200 GeV. STAR and BRAHMS data are shown with statistical and systematic error bars, along with the uncorrected (Original) output from NeXSPheRIO, the initial conditions modified with the R-factor reproducing BRAHMS data and the STAR point (see text). .

comparisons. Assuming that these systematic errors are only dependent on multiplicity, it seems reasonable to simply shift A so that the value at midrapidity agrees with STAR, but maintaining the values of B and C found for BRAHMS. In this case, it goes to $A = 1.22$, resulting in the purple distribution in Fig. 5.2. Doing so for each centrality class yields the values displayed in Table 5.1, corresponding to the distributions in Fig. 5.3.

It is important to remark that "charged particles" include protons $(p, \bar{p})$, pions $(\pi_{\pm})$ and kaons $(K_{\pm})$. This means that even though the sum of their multiplicities is well-adjusted, their individual contributions may still be off. Indeed, as will be shown in §5.2, the distribution of p and $\bar{p}$ is still off. Then, it may be necessary to include another similar step to correct the initial baryon density, but this has not been done yet.

5.1.3 Freeze-out Temperature

The hydrodynamical evolution ends some time after the system has entered the hadronic phase, at freeze-out, as discussed in Ch. 1, and how long the hydrodynamic expansion lasts depends on the freeze-out temperature T_{FO}. Intuitively, the longer the system stays in the hydrodynamic stage, the more it will be accelerated due to pressure gradients in

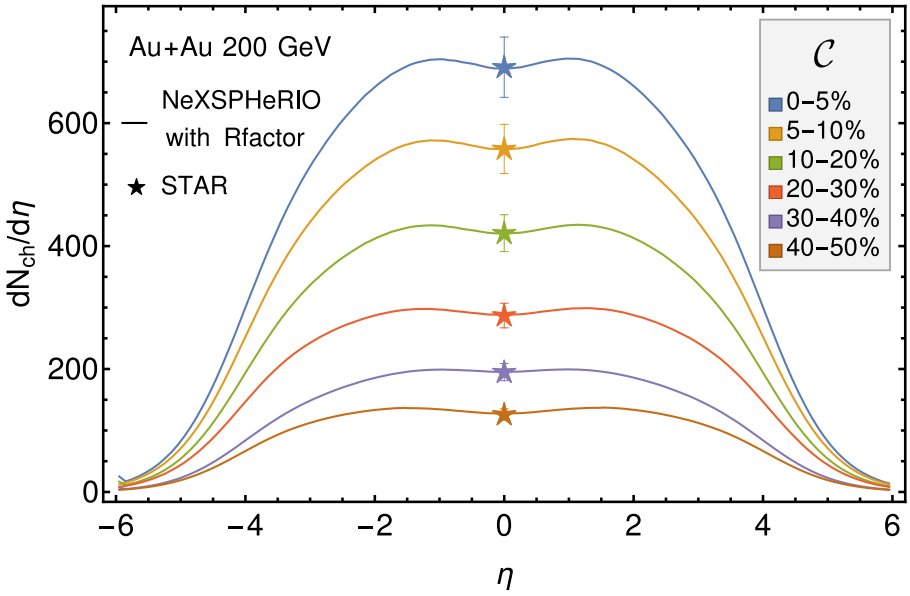

Figure 5.3: Pseudorapidity distributions of charged particles in Au+Au collision at 200 GeV, for several centrality classes. The stars at midrapidity are STAR data; lines are NeXSPheRIO results, using the R-factor described in this section.

the transversal direction, that is, faster particles will be emitted at the freeze-out[3].

Therefore, T_{FO} can be fixed for each centrality class by trial and error, finding the best value to match the transverse momentum spectra of charged particles to experiment [87]. The way I did it is illustrated in Fig. 5.4, using the 5-10% class as an example.

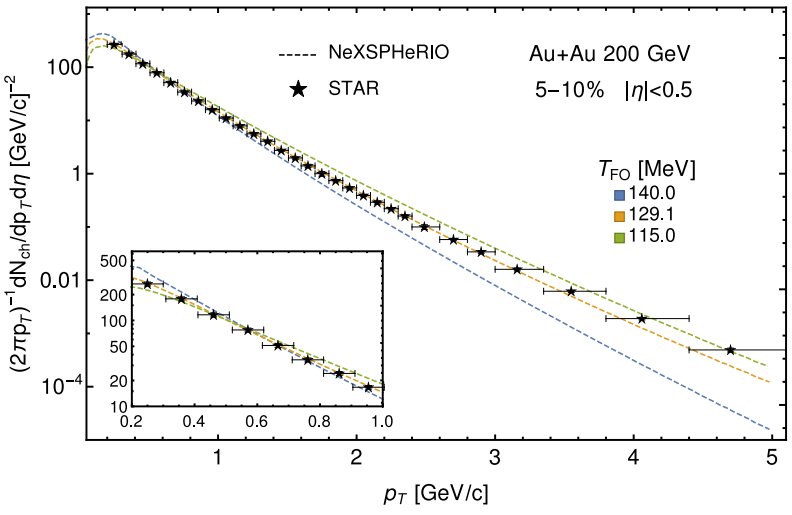

Figure 5.4: Transverse momentum spectra of charged particles from a 5-10% Au+Au collision at 200 GeV, using different values for the freeze-out temperature to match STAR data [87].

Starting with a seemingly reasonable freeze-out temperature, e.g. 140 MeV, run some events in this class – 50 are enough, with few freeze-outs. If the spectrum is lower than

[3]In principle, the particles emitted at lower temperatures have lower thermal velocities and average p_T. This may or may not be compensated by the longer acceleration time, but this seems to be the case.

the experimental data, it means that T_{FO} is too high. Then another temperature should be guessed, say, $T_{FO} = 115$ MeV. This gives a higher distribution than needed (in the lower p_T regions), so the next guess should be between 115 and 140 MeV. This is repeated until the spectrum fits well enough.

The focus is on the low-transverse momentum regions because high-p_T particles are dominated by non-flow processes such as jets, which are not included in NeXSPheRIO.

Doing so for every centrality class yields the values of T_{FO} displayed in Table 5.1, fitting the spectra in Fig. 5.5.

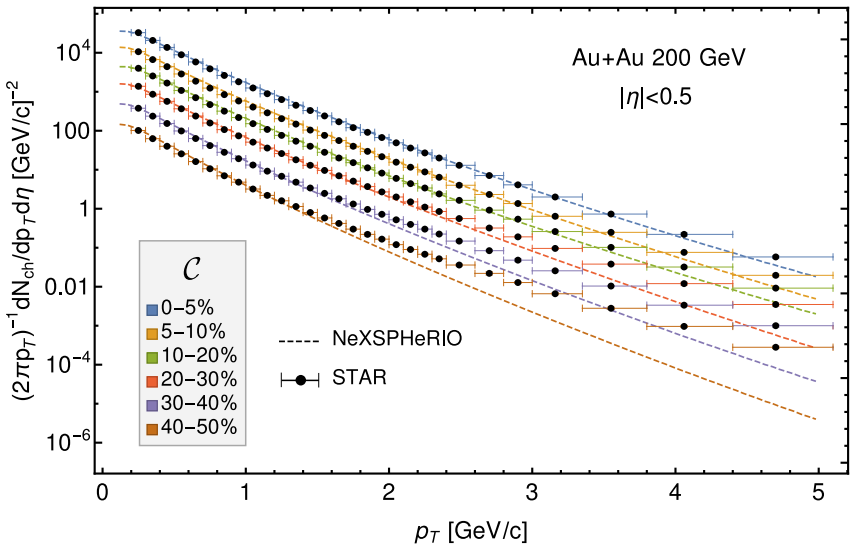

Figure 5.5: The p_T-spectra for charged particles in all centralities, using the appropriate T_{FO} (see table 5.1).

5.2 Proton number

In the following results, the elements described in the past chapters come together: with the calibration described in §5.1 and the *dfer* decay configuration from §4.3.3, I ran 10000 hydro events in NeXSPheRIO that cover the 50% most central events at 200 GeV, each with 5000 freeze-out iterations, as per §4.3.2. Estimating from the runtimes in Table 3.1, this would required a maximum of 24000 computational hours, or 1000 days, or rather 25 days, if using the 40 nodes available in Aguia4. In practice, the more peripherical events are considerably faster, and I estimate that the overall runtime was around 18 days.

In order to account for the spurious fluctuations that arise due to wide centrality classes, STAR uses the *Centrality Bin Width Correction* (CBWC) [29]. It consists in

evaluating the cumulants in smaller centrality bins, and then making an average weighted by the number of events in these smaller bins. I found the CBWC to have the same effect as simply dividing the classes into smaller percentiles, provided there is enough statistics for each class[4]. Therefore, I re-separated the ready events into 2% classes such as 0-2%, 2-4%, and so on, also using the number of participants, and each of these classes contains 400 events.

First of all, it must be noted that the bare NeXSPheRIO code does not have an appropriate baryon stopping, and it does not include baryonic diffusion. Then, the rapidity distributions of protons and antiprotons do not behave correctly. The $\mathrm{d}N\,/\,\mathrm{d}y$ for them is compared to BRAHMS data [88] in Fig. 5.6 and the difference is clear, most notably NeXSPheRIO shows no peak in proton yield at midrapidity[5]. This is likely caused in part by the forced thermalization §3.2, but there may be other contributions, such as a single freeze-out without transport. It would be interesting to study the effect of baryon stopping using other initial conditions, the role of baryonic diffusion (see e.g. [89, 90]), but for now, an ad hoc correction is described in the next section.

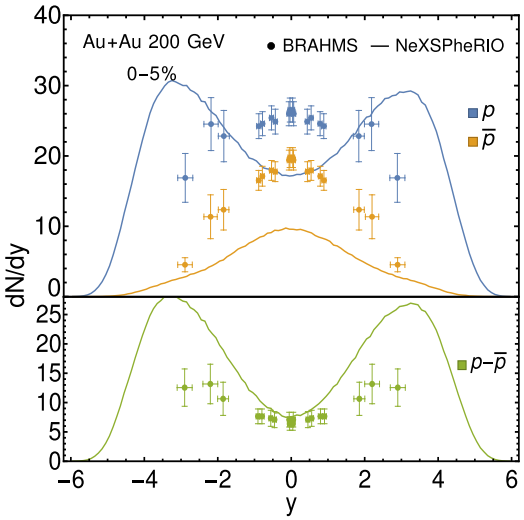

Figure 5.6: (Upper) Proton and antiproton (lower) net-proton rapidity distributions, compared to BRAHMS data, for a central collision.

With that in mind, the cumulants are computed with the method described in Ch. 4. As seen, the method consists in evaluating the inner average in the CGF analytically, assuming some probability of emission at freeze-out. In the case of independent emissions restricted by an acceptance window, I used the binomial distribution, with the parameters M (the number of particles over all space) and p, computed by dividing the mean number λ of particles inside the acceptance window by M. Then, the n^{th} order cumulant of conserved quantities is the n^{th} derivative of the CGF at the origin, dependent on event-by-event averages of λ and p.

[4]This is often not the case in experiments, which is why they use the CBWC in the first place.

[5]The proton and antiproton outputs from NeXus ICs do not show better agreement with experimental data [85], and hydrodynamics do not affect the rapidity distribution significantly.

Therefore, using equations (4.15) through (4.18), I compute the cumulants for the proton (setting $\bar{\lambda} = 0$) and antiproton (setting $\lambda = 0$) in the acceptance window used by STAR ($|y| < 0.5, 0.4 < p_T < 0.8$ GeV/c), and combined them into the skewness S and kurtosis κ defined in (4.3). The results for proton number are shown in Fig. 5.7, and the antiprotons in 5.8, compared to STAR data [76, 91]. The error bars were calculated using jackknife re-sampling[6] [78]. A line joining the experimental points is also plotted for better visualization.

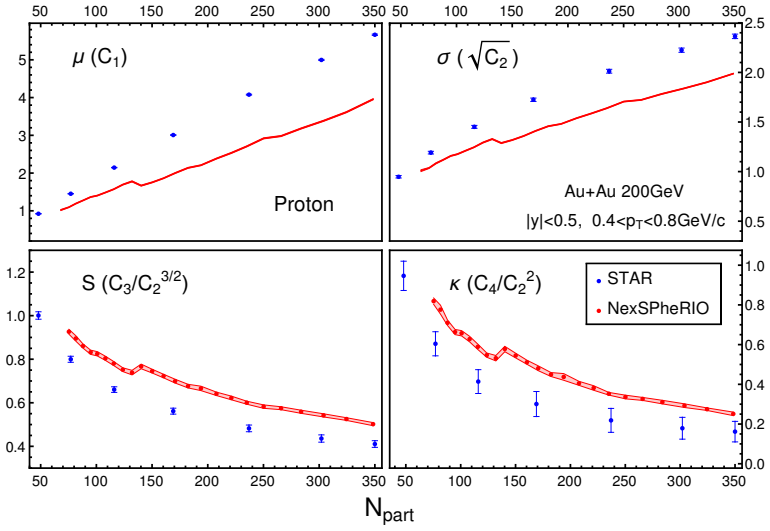

Figure 5.7: The mean μ, standard deviation σ, skewness S and kurtosis κ of event-by-event measurements of proton number in Au+Au collisions at 200 GeV, for 0-50% events. Red dots are NeXSPheRIO results and the blue lines are STAR data [91]. Error bars computed with jackknife re-sampling.

The mean values μ are below experimental points, with too few protons and antiprotons. This can be traced back to the disagreement in the rapidity distributions of Fig. 5.6, and a similar argument can be made for the standard deviations[7] σ.

Another important observation is that, even though they are off, the cumulants follow the correct trend, and with error bars much smaller than the ones computed without the method, as can be checked in Table 4.1. This suggests that the systematic error comes mostly from the wrong values in μ. The way that these quantities are constructed seemingly reduces the impact from the discrepancy in multiplicity, as compared to C_3 and C_4, but does not eliminate it completely.

[6]The jackknife error of a statistical quantity θ consists in removing one data point i from the sample and recomputing, which gives a slightly different value $\hat{\theta}_{(i)}$. Doing so for each data point gives a distribution of $\hat{\theta}$, whose standard deviation is the error in the original θ.

[7]This can also be read directly from (4.16), which for protons is $C_2^p = \langle \lambda^2 \rangle - \langle \lambda \rangle^2 + \langle \lambda(1-p) \rangle$

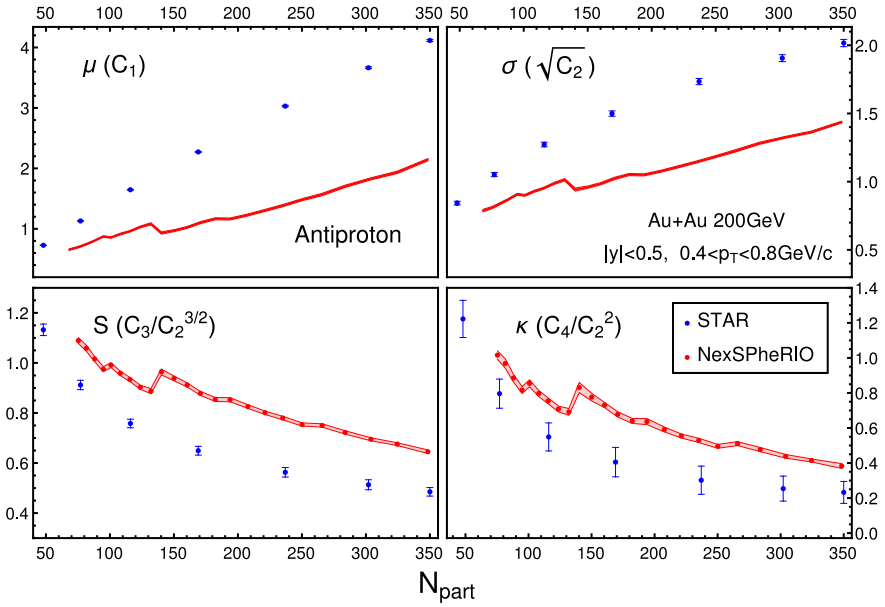

Figure 5.8: Same as Fig. 5.7, for antiproton number

5.2.1 Rescaling

A priori, a correction similar to the R-factor described in §5.1.2 may be possible, but there are some difficulties. First and foremost, the only experimental data on rapidity distribution of protons and antiprotons in literature seems to be for the central events [88]. Furthermore, the shapes of the distributions in Fig. 5.6 are very different, and it is unclear how multiplying the initial *difference* would affect each individually. Lastly, the protons only compose a fraction of the baryons, so a correction on n_B must take it into account. Therefore, a R-factor approach is unachievable, for now at least.

The problem originates in the incorrect $\mathrm{d}N\,/\,\mathrm{d}y$ for protons and antiprotons. A possible ad hoc correction is in changing the values of λ and p (as well as $\bar{\lambda}$ and $\bar{p}$) in a consistent way for all events. I do this as follows:

1. First, I interpolate the data points of μ from STAR with straight lines (in blue), defining a function $\mu_{\mathrm{exp}} \equiv \mu(N_{\mathrm{part}})$;

2. Then, for each centrality class $\mathcal{C}$, I compute the mean value $\mu_{\mathrm{sim}} \equiv \langle\lambda\rangle_{IC}$ and the coefficient $\alpha_{\mathcal{C}} \equiv \dfrac{\mu_{\mathrm{exp}}}{\mu_{\mathrm{sim}}}$;

3. Finally, each event i in $\mathcal{C}$ is shifted by this coefficient: $\lambda'_i = \alpha_{\mathcal{C}}\lambda_i$. This guarantees that the mean values are correct, since $\langle\lambda'\rangle_{IC} = \dfrac{\mu_{\mathrm{exp}}}{\mu_{\mathrm{sim}}}\langle\lambda\rangle_{IC} = \mu_{\mathrm{exp}}$;

A similar process is done for $p = \lambda/M$, the ratio of protons inside the acceptance window[8], but the namely:

4. Using the three-source model proposed in [92], I interpolate the rapidity distribution. This is an union of three Gaussian curves:

$$\frac{\mathrm{d}N}{\mathrm{d}y} = \frac{N_0}{\sqrt{2\pi}}\left[\frac{1-k}{2\sigma_F}e^{-(y+\Delta)^2/2\sigma_F^2} + \frac{k}{\sigma_C}e^{-y^2/2\sigma_C^2} + \frac{1-k}{2\sigma_F}e^{-(y-\Delta)^2/2\sigma_F^2}\right]. \tag{5.2}$$

   For the protons[9], I used $k = 0.866, \sigma_C = 2.255, \sigma_F = 0.5$ and $\Delta = 2.45$. N_0 is an overall normalization irrespective to α_y.

5. Then, I compute the fraction α_y of protons inside the rapidity window by evaluating (5.2) in the range $|y| < 0.5$ and dividing by N_0.

6. Using blast-wave fits [93], I interpolate the p_T-spectra (integrated over y):

$$\frac{\mathrm{d}N}{\mathrm{d}p_T} = R^2 p_T m_T \int_0^1 \mathrm{d}x\, x I_0\left(\frac{p_T \sinh\rho}{T_{FO}}\right) K_1\left(\frac{m_T \cosh\rho}{T_{FO}}\right), \tag{5.3}$$

   where $m_T = \sqrt{m^2 + p_T^2}$ is the transverse mass, $\rho = \tanh^{-1}(\beta_s x)^n$, I_0 and K_1 are Bessel functions, R is an overall normalization, m is the proton mass and n, β_s are parameters of the fit. For the proton, I used $n = 0.7, \beta_s = 0.767$.

7. Then, I integrate (5.3) in the relevant p_T-window, $0.4 < p_T < 0.8$ GeV in this case and divide by the integral over all p_T to find the fraction α_{p_T};

8. Finally, the fraction p_i of each event i in a centrality class is shifted in the same fashion as step 3, fixing $\langle p' \rangle_{IC} = \alpha_y \alpha_{p_T}$. For protons, $\langle p' \rangle_{IC} = 0.041$, and for antiprotons, $\langle p' \rangle_{IC} = 0.056$;

This procedure gives a shifted set of λ's and p's, which are used to compute the CGF (4.14). The resulting cumulants are shown in Figs. 5.9 and 5.10.

[8]Unfortunately, this requires knowledge about $\mathrm{d}N\,/\,\mathrm{d}y$ for all y's, which is only available in the 0-5% class, as stated before. However, under investigation the cumulants do not seem to be strongly affected by small changes in p, when p is small.

[9]For antiprotons, I actually subtracted the net-proton distribution with parameters provided by [92] from the proton distribution.

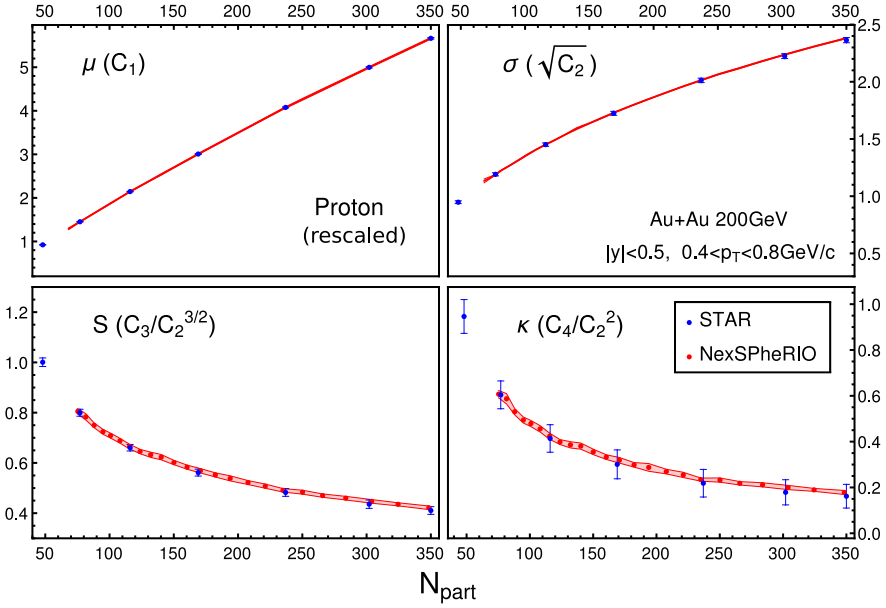

Figure 5.9: The cumulants of proton number, computed by applying the rescaling procedure in the simulated events shown in Fig. 5.7.

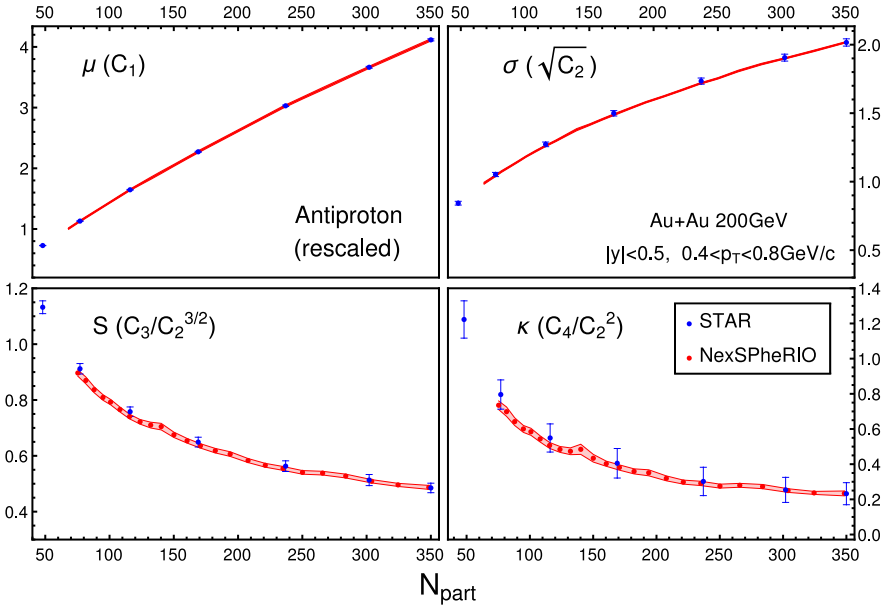

Figure 5.10: Same as Fig. 5.9, for antiprotons.

The correct alignment of μ is trivial by construction after rescaling, but the higher order cumulants are not, being in great agreement with experiment, with small statistical uncertainty. The standard deviation, skewness and kurtosis are very compatible with experiment, matching the data closely.

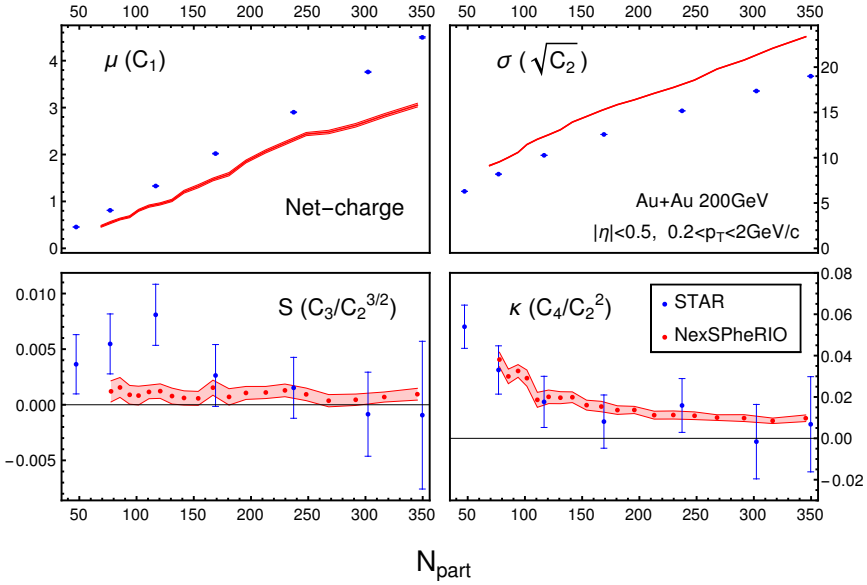

Figure 5.11: The cumulants for net-electric charge in 0-10% Au+Au collisions at 200 GeV, in the acceptance window $|\eta| < 0.5$, $0.2 < p_T < 2$ GeV/c. Red points are NeXSPheRIO events with the method developed, without any correction, and the blue line is STAR data [74].

5.3 Net-charge

The same method can be applied for the net-electric charge, as shown in Fig. 5.11, in comparison to STAR data [74]. Again, μ and σ deviate from experiment, probably due to some inadequacy in the modelling. Even so, S and κ are satisfactory and follow the correct trend. A rescaling procedure such as the one described above may be possible, and I am currently studying the best way to do it, which is not so direct to do because usually experimental groups do not report the data on positive and negative charges separately.

The missing net-charge (~ 1 in central collisions) is most likely in the form of an excess of negative pions in relation to positive pions. It is important to remark that this is a very small difference in comparison to the overall multiplicity (pions compose most of the charged particles in the $\mathrm{d}N_{ch}\,/\,\mathrm{d}\eta$ distributions in Fig. 5.3).

The values of S and κ in Fig. 5.11 are much closer to the experimental data, and with smaller statistical fluctuation, in comparison to the values computed without the method shown in Table 4.1, $S = -0.1 \pm 0.5$ and $\kappa = 0.3 \pm 0.6$ for the 0-5% window.

The error bars in the cumulants are statistical, and their small size can be seen as indicating the efficiency of the method. The impressive part is that each data point is comprised of only 400 events! This suggests that the method developed in this thesis may be a pertinent way to compute cumulants in full $(3+1)$D hydrodynamical simulations.

Chapter 6

Discussion

In this work, I developed a method to compute cumulants of conserved quantities in a hydrodynamic HIC simulation that reduces computational cost. I compared the cumulants obtained with this method to STAR data for proton number, antiproton number, and net-charge in central Au+Au 200 GeV collisions, finding good agreement in the higher-order cumulants even before applying any corrections. These results were obtained using the NeXSPheRIO code, having a small statistical error with only 400 events. Making an ad hoc correction solely on the mean values of proton and antiproton greatly improved the comparison, suggesting that the method is effective.

In the future, I plan to apply the method for collisions at lower energies, where the out-of-equilibrium effects of the QCD CP in the fluid are strong and perceptible, so the net quantities exhibit larger degrees of non-gaussianity. It will also be important to check the consistency of the method by direct comparison to cumulants computed without it, perhaps in a (2+1)D hydro simulation, which would be much less computationally demanding. Moreover, some correction on the rapidity distributions of baryons is necessary, and may be achieved by including baryonic diffusion in NeXSPheRIO; there is already a PhD student in my group starting on this. Another important consideration is the use of a transport model and its implications for the method, since it may introduce correlations between particles, and change the freeze-out distribution.

Even though there is a long road ahead, the results presented in this work point to a useful tool for the analysis of conserved charge fluctuations in the search for the QCD critical point.

Appendix A

Statistical Mechanics

The relativistic nature of the QGP makes possible the creation and annihilation of particles. Therefore, the correct treatment for the thermodynamics of the system must be based on the *grand-canonical ensemble* (GCE). Since a lot of theoretical ingredients in this work rely on it, a brief review about basic statistical mechanics is in place.

In this appendix, I will derive the connection (4.1) between susceptibilities and cumulants, and briefly describe the theoretical equations of state for both hadronic matter and QGP that goes into the matching (2.7).

A.1 Equations of State

In the states i of the GCE, both the number of particles N_i and energy E_i are allowed to fluctuate around the average values $\langle N_i \rangle = N$ and $\langle E_i \rangle = U$ [36]. The grand-canonical potential[1] $\Omega = \Omega(T, V, \mu)$ is a Legendre transformation of the internal energy $U = U(S, V, N)$

$$\Omega = U - TS - \mu N, \tag{A.1}$$

and the macrostate (T, V, μ) that minimizes it denotes thermal and chemical equilibrium, with its possible microstates i distributed with the Gibbs probability

$$p_i = \frac{1}{\mathcal{Z}} e^{(\mu N_i - E_i)/T} = \frac{1}{\mathcal{Z}} e^{(\mu - \epsilon_i) N_i / T}, \tag{A.2}$$

where ϵ_i is the energy per particle in the orbital i and the partition function is

[1] Sometimes referred to as Landau free energy.

$$\mathcal{Z}(T,V,\mu) = e^{-\Omega/T} = \sum_i e^{(\mu-\epsilon_i)N_i/T}, \tag{A.3}$$

with the dependence on volume implicit in the energies ϵ_i. Since the number of particles is not fixed, the sum over all states i can be written as a sum of possible values for the N_i in each state [36], which factorizes onto a product

$$\begin{aligned}\mathcal{Z} &= \sum_{N_0,N_1,\cdots} \exp\left[(\mu-\epsilon_0)\frac{N_0}{T} + (\mu-\epsilon_1)\frac{N_1}{T} + \cdots\right], \\ &= \left\{\sum_{N_0} \exp\left[(\mu-\epsilon_0)\frac{N_0}{T}\right]\right\} \times \left\{\sum_{N_1} \exp\left[(\mu-\epsilon_1)\frac{N_1}{T}\right]\right\} \times \cdots, \\ &= \prod_i \sum_N \exp\left[(\mu-\epsilon_i)\frac{N}{T}\right].\end{aligned} \tag{A.4}$$

The values for N are, of course, determined by the spin-statistics theorem: it can be either 0 or 1, if the particles are fermions, or go up to infinity if they are bosons. Denoting the sum by S_θ, it evaluates to

$$S_\theta = \left\{\begin{array}{ll} 1 + e^{(\mu-\epsilon_i)/T} & \text{if fermions} \\ \dfrac{1}{1-e^{(\mu-\epsilon_i)/T}} & \text{if bosons}\end{array}\right\} = \left[1+\theta e^{(\mu-\epsilon_i)/T}\right]^\theta, \tag{A.5}$$

where $\theta = +1(-1)$ when dealing with fermions(bosons).

In the context of HICs, the volume of the system is hardly – if ever – inferable, then it is necessary to use spatial densities. Conveniently, in a homogeneous system, (A.1) divided by $(-V)$ yields the pressure P. Since the extensivity of $\Omega(T,V,\mu)$ comes solely from the volume, with the temperature and chemical potential being intensive variables, it follows that $P = P(T,\mu)$ only. This is the generic form of the equations of state used here.

From (A.3) and (A.4), the pressure[2] in the GCE can be written as

$$P = \frac{T}{V}\ln\mathcal{Z} = \frac{T}{V}\sum_i \theta \ln\left[1+\theta e^{(\mu-\epsilon_i)/T}\right]. \tag{A.6}$$

If the states are specified in the phase space representation, the pressure is straightforwardly by replacing the sum over i by integrals over position and momentum. If the particles are non-interacting, the energy per particle $\epsilon_i \sim \epsilon(p) = \sqrt{m^2+p^2}$ and the

[2]To be more precise, the pressure field is defined in the limit $V \to 0$.

integrals over positions cancel the volume in the denominator. Then, the pressure is

$$P_\theta(T,\mu) = -\frac{T\theta g}{(2\pi)^3}\int \mathrm{d}^3p \ln\left\{1+\theta\exp\left[\frac{\mu-\epsilon(p)}{T}\right]\right\}, \tag{A.7}$$

where $(2\pi)^3$ comes from the smallest phase space volume element, with $\hbar = 1$, and g is the degeneracy factor of the species considered. Integration by parts in spherical coordinates yields, after some algebra,

$$\boxed{P_\theta(T,\mu) = \frac{g}{6\pi^2}\int_0^\infty \mathrm{d}p\,\frac{p^4}{\epsilon(p)}\left[\exp\left(\frac{\epsilon(p)-\mu}{T}\right)+\theta\right]^{-1}} \tag{A.8}$$

It must be noted that, up to this point, μ is standing for any generic chemical potential. The presence of different conserved quantities would only amount to replacing μ in the previous expressions by a sum of the corresponding potentials.

A.1.1 Hadron Resonance Gas

The strong interaction between composite hadrons is complicated and difficult to describe. However, thermal models [94] suggest that a sum of ideal (quantum) gases reproduces quite well the observed multiplicity ratios when a correction of excluded volume is applied [14], akin to the Van der Waals interaction.

This hadron gas (HG) contains baryons, such as protons and Lambdas, which are fermions composed of three quarks; and mesons, such as pions and kaons, which are bosons composed of a quark-antiquark pair. Using (A.8), the ideal HG pressure in the usual (T,μ_B) will then be split in

$$P_H^{\mathrm{id}} = \sum_{\{\text{mesons } j\}} P_-(T,0) + \sum_{\{\text{baryons } i\}} P_+(T,B_i\mu_B), \tag{A.9}$$

where B_i is the baryon number of the baryon i.

The *excluded-volume correction* consists in subtracting the available volume V in the partition function (A.3) by vN, where v is the size of the hard-core of each particle. Of course, each hadron has a different effective radius, which may be set by particle ratios measurements [95].

Making a Laplace transform, this amounts to changing the μ to $\tilde{\mu} = \mu - vP$, with P being the *total* pressure in the system. Just as the chemical potential can be interpreted as the energetic cost of introducing a new point particle, this correction is simply adding to such cost the internal energy of a bulky particle. Then, (A.9) would be modified to

$$P_H(T, \mu_B) = \sum_{\{\text{mesons } j\}} P_-(T, -v_j P_H) + \sum_{\{\text{baryons } i\}} P_+(T, B_i \mu_B - v_i P_H). \tag{A.10}$$

The other thermodynamic quantities are simply found using derivatives of (A.1). Expression (A.10) constitutes an implicit equation for P_H, that must be solved numerically for each point of the phase diagram. In practice, the equation of state in NexSPheRIO uses the set of particles and resonances with mass smaller than a cutoff – 1.5 GeV for mesons and 2 GeV for baryons – selected from the Particle Data Group [64]; and the radii $r = 0.7$ fm for baryons and $r = 0$ for mesons [14], with $v = \frac{4}{3}\pi r^3$. Solving (A.10) with an iterative numerical method, a table is generated containing the values of the thermodynamic quantities in the desired range of the phase diagram.

A.1.2 MIT Bag Model

One of the well-known features of QCD is the asymptotic freedom, where the strength of the interaction between quarks and gluons becomes weak at very high energies, so they are asymptotically free. Meanwhile, no isolated quark or gluon has been detected, leading to the concept of color confinement: as the energy between two color charges (e.g. a quark-antiquark pair) increases, it becomes more energetically favorable to produce another pair in between, so any detected particle must be colorless. A useful phenomenological description for this behavior is provided by the MIT Bag Model.

In this model, hadrons are modeled as free quarks inside a bag of finite dimension, whose effect is to add a constant $-B$ to the total pressure, which then is just the sum of (A.8) computed for all degrees of freedom. In the energy density range of HICs, these are the gluons and the three lightest quarks.

Since gluons are massless bosons, their mass and baryon charge vanish, thus the integral in (A.8) can be evaluated analytically, yielding $\boxed{P_g = \frac{g_g}{90}\pi^2 T^4,}$ with degeneracy $g_g = 2_{\text{spin}} \times 8_{\text{color}}$. The up and down quarks have a very small mass, neglected here. Then

they contribute to the pressure with

$$\boxed{P_{u,d} = \frac{g_{u,d}}{6\pi^2}\left[\frac{1}{4}\mu_q^4 + \frac{\pi^2}{2}\mu_q^2 T^2 + \frac{7\pi^4}{60}T^4\right],}$$

where $g_{u,d} = 2_{\text{anti}} \times 2_{\text{spin}} \times 3_{\text{color}}$, with the "anti" subscript indicating the inclusion of both quarks and antiquarks (which eliminates the odd-μ powers), and $\mu_q = \mu_B/3$.

The mass of the strange quark is too large to neglect, so P_s must be evaluated numerically. With the bag constant, the total pressure in the QGP phase is

$$\boxed{\begin{aligned} P_{QGP}(T,\mu_B) = \frac{\mu_B^4}{162\pi^2} + \frac{\mu_B^2 T^2}{9} + \frac{37\pi^2 T^4}{90} + \\ + P_+\left(T, \frac{\mu_B}{3}\right) + P_+\left(T, -\frac{\mu_B}{3}\right) - B, \end{aligned}} \tag{A.11}$$

where the P_+ terms represent the contribution from the strange quark and antiquark.

The mass of the strange quark used in this work is $m_s = 120$ MeV and the bag pressure is taken as $B = 380$ MeV/fm^3.

There are more sophisticated equations of state, which use extrapolations of LQCD adding a critical point, but the parametrization (2.7) used in this work allows for changing the position of the CP very easily.

A.2 From χ_n to C_n

The thermodynamical susceptibilities are defined in (1.2) as derivatives of the adimensional pressure P/T^4 with respect to the reduced chemical potential $\hat{\mu} \equiv \mu/T$. Using the first equality of (A.6), the susceptibilities can be written as

$$\chi_n = \frac{1}{VT^3}\frac{\partial^n}{\partial \hat{\mu}^n} \ln \mathcal{Z}. \tag{A.12}$$

Another way to express the partition function is

$$\mathcal{Z}(T, V, \hat{\mu}) = \sum_N e^{\hat{\mu}N} Z_N(T, V), \tag{A.13}$$

where Z_N is the *canonical* partition function containing information about the energy and

interactions of the system when it has N particles. This implies that the probability for the system to have N particles is given by

$$w_N \equiv e^{\hat{\mu}N} \frac{Z_N(T,V)}{\mathcal{Z}(T,V,\hat{\mu})}. \tag{A.14}$$

In (4.2), the cumulant generating function of particle X was introduced as the logarithm of the average of e^{zX}, which is a sum over using the probabilities (A.14):

$$\begin{aligned} \mathrm{CGF}(z) &= \ln \sum_N w_N e^{zN}, \\ &= \ln \sum_N e^{(\hat{\mu}+z)N} \frac{Z_N(T,V)}{\mathcal{Z}(T,V,\hat{\mu})}, \\ &= \ln \left[\frac{\mathcal{Z}(T,V,\hat{\mu}+z)}{\mathcal{Z}(T,V,\hat{\mu})} \right], \\ &= \ln \mathcal{Z}(T,V,\hat{\mu}+z) - \ln \mathcal{Z}(T,V,\hat{\mu}). \end{aligned} \tag{A.15}$$

As discussed in Ch. 4, the cumulants are derivatives of the $\mathrm{CGF}(z)$ computed at $z = 0$. Therefore,

$$\begin{aligned} C_n &\equiv \frac{\partial^n}{\partial z^n} \mathrm{CGF}(z)\Big|_{z=0}, \\ &= \frac{\partial^n}{\partial z^n} \ln \mathcal{Z}(T,V,\hat{\mu}+z)\Big|_{z=0}, \\ &= \frac{\partial^n}{\partial \hat{\mu}^n} \ln \mathcal{Z}(T,V,\hat{\mu}), \\ &= VT^3 \chi_n. \end{aligned} \tag{A.16}$$

This proves the connection (4.1) between susceptibilities of a particle species in the system and the corresponding probability distribution.

Appendix B

Relativistic Hydrodynamics

The dynamics of the thermalized system after a HIC are inherently relativistic, not only because large flow velocities are involved, but a substantial amount of energy is deposited in a confined space as well. This energy density also creates an environment where the individual particles interact a lot, so that a hydrodynamic description applies.

This appendix explicits the equations of motion of both ideal hydrodynamics and their SPH representation, through minimization of an action.

B.1 Ideal equations of motion

To start, the energy-momentum tensor must be defined, recalling that T^{00} is the energy density denoted by ϵ, T^{ij} is the flux along the i axis of the j^{th} momentum component, T^{0i} is the i^{th} momentum density component and T^{i0} the energy flux along the i axis [96]. Considering a small element of fluid in its local rest frame, the momentum component is 0 and so is the energy flux. The momentum flux through a surface $\mathrm{d}A^j$ of the fluid element is simply the force acting on this element. At rest, Pascal's Law states that the pressure P exerted by a portion of fluid is isotropic and radial, perpendicular to the surface on which it acts. Hence $T^{ij}\,\mathrm{d}A^j = P\,\mathrm{d}A^i$ and therefore $T^{ij} = P\delta^{ij}$ in this frame. In summary, the energy-momentum tensor in the local rest frame can be represented by $T^{\mu\nu}_R = \mathrm{diag}(\epsilon, P, P, P)$.

To determine the general form of $T^{\mu\nu}$ in any frame, it's useful to note the following properties of a Lorentz transformation Λ^μ_ν:

(I) The 4-velocity of the fluid is a vector, and at rest it is $u^\mu_R = (1,0,0,0)$. This means that

$$u^\mu = \Lambda^\mu_\nu u^\nu_R = \Lambda^\mu_0; \tag{B.1}$$

(II) The Minkowski metric $g^{\mu\nu}$ is diagonal, and in this work we use the signature $(+,-,-,-)$. Then, since the Lorentz transformation is orthogonal $\Lambda^{-1} = \Lambda^T$, it follows that $g^{\mu\nu} = \Lambda^\mu_\alpha \Lambda^\nu_\beta g^{\alpha\beta} = \Lambda^\mu_0 \Lambda^\nu_0 - \Lambda^\mu_i \Lambda^\nu_i$. Using the previous point results in

$$\Lambda^\mu_i \Lambda^\nu_i = u^\mu u^\nu - g^{\mu\nu}. \tag{B.2}$$

With these properties in mind, the energy-momentum tensor for a fluid with the velocity *field* u^μ is

$$T^{\mu\nu} = \Lambda^\mu_\alpha \Lambda^\nu_\beta T^{\alpha\beta}_R = (\epsilon + P) u^\mu u^\nu - P g^{\mu\nu}. \tag{B.3}$$

The very concept of an ideal motion is that the energy, momentum and particle number are all conserved. The first two are expressed by (2.3), and the last by (2.4), as discussed in the main text. Using that $u_\mu u^\mu = 1$ which leads to $u_\mu \partial_\nu u^\mu = 0$, the projection of (2.3) in the direction of the fluid velocity yields

$$\begin{aligned} u_\mu \partial_\nu T^{\mu\nu} &= u^\nu \partial_\nu (\epsilon + P) + (\epsilon + P) \partial_\nu u^\nu - u^\nu \partial_\nu P, \\ 0 &= u^\nu \partial_\nu \epsilon + (\epsilon + P) \partial_\nu u^\nu. \end{aligned}$$

Invoking the first law of thermodynamics and the Euler homogeneity condition,

$$\mathrm{d}U = T\,\mathrm{d}S - P\,\mathrm{d}V + \mu\,\mathrm{d}N\,, \tag{B.4}$$

$$U = TS - PV + \mu N, \tag{B.5}$$

respectively, with the volume densities given by $\epsilon \equiv \dfrac{U}{V}$, $\sigma \equiv \dfrac{S}{V}$ and $n = \dfrac{N}{V}$, the relations $\mathrm{d}\epsilon = T\,\mathrm{d}\sigma + \mu\,\mathrm{d}n$ and $\epsilon + P = T\sigma + \mu n$ appear and can be used to find the entropy conservation, assuming particle conservation (2.4):

$$\begin{aligned} u_\mu \partial_\nu T^{\mu\nu} &= u^\nu \left(T\partial_\nu \sigma + \mu \partial_\nu n\right) + (T\sigma + \mu n)\partial_\nu u^\nu, \\ 0 &= T\partial_\nu(\sigma u^\nu) + \mu \partial_\nu (n u^\nu), \\ \boxed{0 &= \partial_\nu (\sigma u^\nu).} \end{aligned} \tag{B.6}$$

The trajectories of constant baryon asymmetry are also found:

$$\frac{\mathrm{d}}{\mathrm{d}\tau}\left(\frac{\sigma}{n}\right) = u^\mu \partial_\mu \left(\frac{\sigma}{n}\right) = \frac{u^\mu}{n}\partial_\mu \sigma - \frac{\sigma u^\mu}{n^2}\partial_\mu n,$$

and using (2.4) and (B.6) to substitute the derivatives results in

$$-\frac{\sigma}{n}\partial_\mu u^\mu + \frac{\sigma n}{n^2}\partial_\mu u^\mu = \boxed{\frac{\mathrm{d}}{\mathrm{d}\tau}\left(\frac{\sigma}{n}\right) = 0,} \tag{B.7}$$

as discussed within the main text. Heuristically, one can say that since both entropy and particle number are conserved, so is their ratio, and the system is then bound to constant σ/n lines in the phase diagram.

A more instructive way to write the equations of motion comes from

$$0 = \partial_\alpha T^{\alpha\beta} = \partial_\alpha \left[(\epsilon + P)u^\alpha u^\beta\right] - g^{\alpha\beta}\partial_\alpha P. \tag{B.8}$$

With a conserved density ρ, the first term can be rewritten

$$\partial_\alpha \left[\frac{(\epsilon+P)u^\beta}{\rho}\rho u^\alpha\right] = \rho u^\alpha \partial_\alpha \left[\frac{(\epsilon+P)u^\beta}{\rho}\right] + \left[\frac{(\epsilon+P)u^\beta}{\rho}\right] \underbrace{\partial_\alpha(\rho u^\alpha)}_{=0},$$

so that, dividing (B.8) by ρ and contracting with $g_{\mu\beta}$, the equations of motion become

$$\boxed{\frac{\mathrm{d}}{\mathrm{d}\tau}\left[u_\mu \frac{(\epsilon+P)}{\rho}\right] = \frac{\partial_\mu P}{\rho}.} \tag{B.9}$$

Here, ρ stands for the density of entropy, particle number, or any locally conserved extensive quantity. These calculations are valid in any coordinate system, if the partial derivative ∂_μ is replaced by the covariant derivative ∇_μ.

B.2 The Action principle

In order to determine the equations of motion in SPH form, the variational principle can be applied. Even though the SPH representation could be heuristically determined using (B.9), the variational approach guarantees that the SPH particle coordinates and momenta $\{\vec{r}_j, \dot{\vec{r}}_j\}$ are the optimal dynamical parameters [68]. Then it is necessary to find a Lagrangian density that reproduces (B.8). A suitable candidate, upon convenient parametrizations of n and u^α, is the proper energy density ϵ [71]. Then, in generalized coordinates with metric determinant g , the action principle is

$$\delta I = -\delta \int \mathrm{d}^4x \, \sqrt{-g}\epsilon = 0, \tag{B.10}$$

and the conservation of entropy in the proper frame is

$$\nabla_\alpha(\sigma u^\alpha) = \frac{1}{\sqrt{-g}}\partial_\alpha(\sqrt{-g}\sigma u^\alpha) = 0. \tag{B.11}$$

Separating the time and space components and denoting $u^\alpha = (\gamma, \gamma\vec{v})$, (B.11) gives

$$\partial_0\left(\sqrt{-g}\sigma\gamma\right) = -\vec{\nabla}\cdot\left(\sqrt{-g}\sigma\gamma\vec{v}\right), \tag{B.12}$$

with the generalized Lorentz factor γ depending on $\vec{v}$ via $u^\alpha u_\alpha = 1$, which gives

$$\gamma = \frac{1}{\sqrt{g_{00} - \vec{v}^T\mathbf{g}\vec{v}}}, \tag{B.13}$$

where $-\mathbf{g}$ is the 3×3 matrix part of $g_{\mu\nu}$ with spatial components. Relation (B.12) is a continuity equation, so a spatial integration shows that the total entropy is expressed as

$$S = \int \mathrm{d}^3x \, \sqrt{-g}\sigma\gamma, \tag{B.14}$$

which provides the SPH reference density in the space-fixed frame, defined as

$$\sigma^* = \sqrt{-g}\sigma\gamma \approx \sum_{j=1}^{N} \nu_j W(\vec{r} - \vec{r}_j; h). \tag{B.15}$$

Following (3.7), the SPH representation of the action I in (B.10) is written

$$\begin{aligned} I &= -\int \mathrm{d}\tau \int \mathrm{d}^3x \sum_{j=1}^{N} \sqrt{-g_j}\nu_j \frac{\epsilon_j}{\sigma_j^*} W(\vec{r}-\vec{r}_j;h), \\ &= -\int \mathrm{d}\tau \sum_{j=1}^{N} \nu_j \frac{\epsilon_j}{\gamma_j \sigma_j} \int \mathrm{d}^3x\, W(\vec{r}-\vec{r}_j;h), \\ \boxed{I &= -\int \mathrm{d}\tau \sum_{j=1}^{N} \frac{E_j}{\gamma_j},} \end{aligned} \tag{B.16}$$

where $E_j = \epsilon_j(\nu_j/\sigma_j) = \epsilon_j V_j$ is the rest energy of particle j, with the proper volume V_j, and the normalization of the kernel was used, along with (B.15).

B.2.1 Minimization

The action (B.16) is minimized by some trajectory of the SPH particles, therefore the variations, denoted by δ, are to be taken with respect to virtual changes in the configuration $\{\vec{r}_i, \dot{\vec{r}}_i\}$. In the r.h.s. of the First Law (B.4), the only thermodynamical variable dependent on the spatial configuration is the volume occupied by each particle, while entropy and particle number are blind to virtual changes in positions [68]. Consequently, if no dissipation is present, a virtual variation in the energy is $\delta E = -P\delta V$. Then, the variation of (B.16) yields

$$\delta I = -\int \mathrm{d}\tau \sum_{j=1}^{N} \left(\frac{\delta E_j}{\gamma_j} - E_j \frac{\delta\gamma_j}{\gamma_j^2} \right) = \int \mathrm{d}\tau \sum_{j=1}^{N} \frac{1}{\gamma_j} \left(P_j \delta V_j + \epsilon_j V_j \frac{\delta\gamma_j}{\gamma_j} \right). \tag{B.17}$$

As mentioned before, the volume of a SPH particle j is the reference charge ν_j it carries divided by its density σ_j in its proper frame, so using (B.15),

$$V_j = \frac{\nu_j}{\sigma_j} = \frac{\nu_j \gamma_j \sqrt{-g_j}}{\sigma_j^*}.$$

Then, a variation in volume is

$$\begin{aligned}\delta V_j &= \frac{\nu_j\sqrt{-g_j}}{\sigma_j^*}\delta\gamma_j - \frac{\nu_j\gamma_j\sqrt{-g_j}}{(\sigma_j^*)^2}\delta\sigma_j^* + \frac{\nu_j\gamma_j}{\sigma_j^*}\delta\sqrt{-g_j},\\ &= V_j\left(\frac{\delta\gamma_j}{\gamma_j} - \frac{\delta\sigma_j^*}{\sigma_j^*} + \frac{\delta\sqrt{-g_j}}{\sqrt{-g_j}}\right),\end{aligned} \tag{B.18}$$

which leads to

$$\boxed{\delta I = \int \mathrm{d}\tau \sum_{j=1}^{N} \frac{V_j}{\gamma_j}\left[(P_j+\epsilon_j)\frac{\delta\gamma_j}{\gamma_j} - P_j\frac{\delta\sigma_j^*}{\sigma_j^*} + P_j\frac{\delta\sqrt{-g_j}}{\sqrt{-g_j}}\right].} \tag{B.19}$$

I will tackle each of these variations individually, the goal is to express them as variations in $\vec{r}$. From the definition (B.13),

$$\delta\gamma = -\frac{\gamma^3}{2}\left[\delta g_{00} - 2\delta\vec{v}\cdot(\mathbf{g}\vec{v}) - \vec{v}^T(\delta\mathbf{g})\vec{v}\right], \tag{B.20}$$

where the particle label is omitted and I used the fact that $(\delta\vec{v}^T)\mathbf{g}\vec{v} = [(\delta\vec{v}^T)\mathbf{g}\vec{v}]^T = \vec{v}^T\mathbf{g}(\delta\vec{v})$, since the metric is symmetric. The first and third terms are simply the derivatives of the metric with respect to the spatial coordinates. For the second term, a chain rule provides

$$\delta\vec{v}\cdot(\mathbf{g}\vec{v}) = \delta\left(\frac{\mathrm{d}\vec{r}}{\mathrm{d}\tau}\right)\cdot(\mathbf{g}\vec{v}) = \frac{\mathrm{d}(\delta\vec{r})}{\mathrm{d}\tau}\cdot(\mathbf{g}\vec{v}) = \frac{\mathrm{d}}{\mathrm{d}\tau}\left[\delta\vec{r}\cdot(\mathbf{g}\vec{v})\right] - \delta\vec{r}\cdot\frac{\mathrm{d}(\mathbf{g}\vec{v})}{\mathrm{d}\tau},$$

whose first term is a total derivative in proper time, so upon the integration in (B.10) it vanishes. Then, the important part of the variation of the Lorentz factor in (B.19) reads[1]

$$\boxed{\delta\gamma = -\gamma^3\delta\vec{r}\cdot\left[\frac{\mathrm{d}(\mathbf{g}\vec{v})}{\mathrm{d}\tau} + \frac{1}{2}\left(\vec{\nabla}g_{00} - \vec{v}^T\vec{\nabla}\mathbf{g}\vec{v}\right)\right].} \tag{B.21}$$

Next, the variation of the reference density can be determined with the SPH representation (B.15),

$$\delta\sigma_j^* = \sum_{k=0}^{N}\nu_k\left(\delta\vec{r}_j - \delta\vec{r}_k\right)\cdot\vec{\nabla}W(\vec{r}_j - \vec{r}_k; h). \tag{B.22}$$

The kernel is symmetric in a parity inversion $\vec{r}\to-\vec{r}$, so its gradient is anti-symmetric

[1]The last term may be a little confusing. To clarify, in the Einstein summation notation it is equivalent to $v^a v^b(\partial_c\mathbf{g}_{ab})\hat{e}^c$, with the indices over space components.

and $\vec{\nabla}W_{ij} = -\vec{\nabla}W_{jk}$, using the shorthand $W_{jk} \equiv W(\vec{r}_j - \vec{r}_k; h)$. Since both k and j labels are being summed over in the action (B.16), they are dummy indices. Swapping $j \leftrightarrow k$ only in the $\delta\vec{r}_k$ term in (B.22), the contribution of $\delta\sigma^*$ to the second term of (B.19) is

$$\sum_{j=1}^{N} \frac{P_j}{\gamma_j} \frac{\nu_j \gamma_j \sqrt{-g_j}}{(\sigma_j^*)^2} \delta\sigma_j^* = \boxed{\sum_{j,k=0}^{N} \nu_j \nu_k \left[\frac{P_j \sqrt{-g_j}}{(\sigma_j^*)^2} + \frac{P_k \sqrt{-g_k}}{(\sigma_k^*)^2} \right] \delta\vec{r}_j \cdot \vec{\nabla} W_{jk}.} \tag{B.23}$$

Lastly, as stated before (B.21), variations of the metric simply become space derivatives multiplied by $\delta\vec{r}$, vanishing if the metric is independent of $\vec{r}$:

$$\boxed{\delta\sqrt{-g} = \left(\vec{\nabla}\sqrt{-g}\right) \cdot \delta\vec{r}.} \tag{B.24}$$

The action principle (B.10) applies for a generic variation $\delta\vec{r}_j$ in the positions of the SPH particles, so the coefficients multiplying each variation sum up to zero for every j. Putting the contributions (B.21), (B.23) and (B.24) in (B.19) this means that

$$\begin{aligned} \frac{\mathrm{d}\vec{\pi}_j}{\mathrm{d}\tau} = &- \sum_{k=0}^{N} \nu_j \nu_k \left[\frac{P_j \sqrt{-g_j}}{(\sigma_j^*)^2} + \frac{P_k \sqrt{-g_k}}{(\sigma_k^*)^2} \right] \vec{\nabla} W(\vec{r}_i - \vec{r}_j) + \\ &+ \frac{\nu_j \gamma_j^2}{2} \left(\frac{P_j + \epsilon_j}{\sigma_j^*} \right) (\vec{\nabla} g_{00} - \vec{v}^T \vec{\nabla} \mathbf{g} \vec{v})_j + \\ &+ \frac{\nu_j P_j}{\sigma_j^*} \left(\vec{\nabla} \sqrt{-g_j} \right), \end{aligned} \tag{B.25}$$

where $\vec{\pi}_j$ can be thought of as the 3-momentum of particle j, written as

$$\vec{\pi}_j = \nu_j \gamma_j^2 \left(\frac{P_j + \epsilon_j}{\sigma_j^*} \right) \mathbf{g}_j \vec{v}_j. \tag{B.26}$$

In Milne coordinates $\left\{\tau = \sqrt{t^2 - z^2},\ \eta = \operatorname{arctanh}\frac{z}{t}\right\}$, the metric is $\mathrm{diag}(1, -1, -1, -\tau^2)$, so $\sqrt{-g} = \tau$ and the space derivatives of the metric vanish, so only the first line in (B.25) is non-zero. In these coordinates, the SPH equations of motion reduce to the ones described in §3.3.1.

The equations of motion (B.25) are found in literature [14, 68], but the derivation is usually omitted or simplified, so I considered useful to detail it here.

Bibliography

[1] F. Wilczek, "QCD made simple", *Phys. Today*, vol. 53, no. 8, pp. 22–28, 2000.

[2] F. Wilczek, "Nobel Lecture: Asymptotic freedom: From paradox to paradigm", *Rev. Mod. Phys.*, vol. 77, no. 3, p. 857, 2005.

[3] J. Greensite, *An introduction to the confinement problem*, vol. 821. Springer, 2011.

[4] W. Florkowski, *Phenomenology of ultra-relativistic heavy-ion collisions*. World Scientific Publishing Company, 2010.

[5] D. J. Gross and F. Wilczek, "Ultraviolet behavior of non-abelian gauge theories", *Phys. Revi. Lett.*, vol. 30, no. 26, p. 1343, 1973.

[6] H. D. Politzer, "Reliable perturbative results for strong interactions?", *Phys. Rev. Lett.*, vol. 30, no. 26, p. 1346, 1973.

[7] M. Strickland, "Anisotropic hydrodynamics: Three lectures", *Acta Phys. Pol. B*, vol. 45, no. 12, p. 2355, 2014.

[8] W. Busza, K. Rajagopal, and W. Van Der Schee, "Heavy ion collisions: the big picture and the big questions", *Annu. Rev. Nucl. Part. S.*, vol. 68, pp. 339–376, 2018.

[9] R. Vogt, *Ultrarelativistic heavy-ion collisions*. Elsevier, 2007.

[10] J. Ellis, "The discovery of the gluon", in *50 Years Of Quarks*, pp. 189–198, World Scientific, 2015.

[11] W. Broniowski, W. Florkowski, M. Chojnacki, and A. Kisiel, "Free-streaming approximation in early dynamics of relativistic heavy-ion collisions", *Phys. Rev. C*, vol. 80, no. 3, p. 034902, 2009.

[12] A. Kurkela, A. Mazeliauskas, J.-F. Paquet, S. Schlichting, and D. Teaney, "Effective kinetic description of event-by-event pre-equilibrium dynamics in high-energy heavy-ion collisions", *Phys. Rev. C*, vol. 99, no. 3, p. 034910, 2019.

[13] A. Bazavov, H. Collaboration, *et al.*, "The QCD equation of state", *Nucl. Phys. A*, vol. 931, pp. 867–871, 2014.

[14] Y. Hama, T. Kodama, and O. Socolowski Jr, "Topics on hydrodynamic model of nucleus-nucleus collisions", *Braz. J. Phys.*, vol. 35, no. 1, pp. 24–51, 2005.

[15] J. Cleymans and H. Satz, "Thermal hadron production in high energy heavy ion collisions", *Z. Phys.*, vol. 57, no. 1, pp. 135–147, 1993.

[16] G. Odyniec, "The RHIC Beam Energy Scan program in STAR and what's next...", in *Jo. Phys: Conf. Ser.*, vol. 455, p. 012037, IOP Publishing, 2013.

[17] M. Alford, K. Rajagopal, and F. Wilczek, "Color-flavor locking and chiral symmetry breaking in high density QCD", *Nucl. Phys. B*, vol. 537, no. 1-3, pp. 443–458, 1999.

[18] M. G. Alford, A. Schmitt, K. Rajagopal, and T. Schäfer, "Color superconductivity in dense quark matter", *Rev. Mod. Phys.*, vol. 80, no. 4, p. 1455, 2008.

[19] M. Baldo, M. Buballa, G. Burgio, F. Neumann, M. Oertel, and H.-J. Schulze, "Neutron stars and the transition to color superconducting quark matter", *Phys. Lett. B*, vol. 562, no. 3-4, pp. 153–160, 2003.

[20] N. K. Glendenning, *Compact stars: Nuclear physics, particle physics and general relativity*. Springer Science & Business Media, 2012.

[21] A. Bauswein, N.-U. F. Bastian, D. Blaschke, K. Chatziioannou, J. A. Clark, T. Fischer, H.-T. Janka, O. Just, M. Oertel, and N. Stergioulas, "Equation-of-state constraints and the QCD phase transition in the era of gravitational-wave astronomy", in *AIP Conference Proceedings*, vol. 2127, p. 020013, AIP Publishing LLC, 2019.

[22] J. Berges and K. Rajagopal, "Color superconductivity and chiral symmetry restoration at non-zero baryon density and temperature", *Nucl. Phys. B*, vol. 538, no. 1-2, pp. 215–232, 1999.

[23] C. Ratti, "Lattice QCD and heavy ion collisions: a review of recent progress", *Rep. Prog. Phys.*, vol. 81, no. 8, p. 084301, 2018.

[24] M. Stephanov, "QCD phase diagram: an overview", in *XXIVth International Symposium on Lattice Field Theory*, pp. 24–1, 2006.

[25] F. R. Brown, F. P. Butler, H. Chen, N. H. Christ, Z. Dong, W. Schaffer, L. I. Unger, and A. Vaccarino, "On the existence of a phase transition for QCD with three light quarks", *Phys. Rev. Lett.*, vol. 65, no. 20, p. 2491, 1990.

[26] Y. Aoki, G. Endrődi, Z. Fodor, S. Katz, and K. Szabo, "The order of the quantum chromodynamics transition predicted by the standard model of particle physics", *Nature*, vol. 443, no. 7112, pp. 675–678, 2006.

[27] Y. A. Çengel, R. H. Turner, J. M. Cimbala, and M. Kanoglu, *Fundamentals of thermal-fluid sciences*, vol. 703. McGraw-Hill New York, 2008.

[28] M. A. Stephanov, "QCD phase diagram and the critical point", *Prog. Theor. Phys., Suppl.*, vol. 153, no. hep-ph/0402115, pp. 139–156, 2004.

[29] X. Luo and N. Xu, "Search for the QCD critical point with fluctuations of conserved quantities in relativistic heavy-ion collisions at RHIC: an overview", *Nucl. Sci. Tech.*, vol. 28, no. 8, p. 112, 2017.

[30] L. D. Landau, E. M. Lifshitz, and L. P. Pitaevskii, *Course of theoretical physics: statistical physics*. Elsevier Butterworth Heinemann, 1980.

[31] B. Berdnikov and K. Rajagopal, "Slowing out of equilibrium near the QCD critical point", *Phys. Rev. D*, vol. 61, no. 10, p. 105017, 2000.

[32] M. Stephanov, "Non-Gaussian fluctuations near the QCD critical point", *Phys. Rev. Lett.*, vol. 102, no. 3, p. 032301, 2009.

[33] M. Stephanov, "Sign of kurtosis near the QCD critical point", *Phys. Rev. Lett.*, vol. 107, no. 5, p. 052301, 2011.

[34] M. Stephanov, K. Rajagopal, and E. Shuryak, "Signatures of the tricritical point in QCD", *Phys. Rev. Lett.*, vol. 81, no. 22, p. 4816, 1998.

[35] Z. Li, Y. Chen, D. Li, and M. Huang, "Locating the QCD critical end point through peaked baryon number susceptibilities along the freeze-out line", *Chinese Phys. C*, vol. 42, no. 1, p. 013103, 2018.

[36] S. Salinas, *Introduction to statistical physics*. Springer Science & Business Media, 2001.

[37] F. Rennecke, "Review of Critical Point Searches and Beam-Energy Studies", in *Multidisciplinary Digital Publishing Institute Proceedings*, vol. 10, p. 8, 2019.

[38] P. Parotto, M. Bluhm, D. Mroczek, M. Nahrgang, J. Noronha-Hostler, K. Rajagopal, C. Ratti, T. Schäfer, and M. Stephanov, "QCD equation of state matched to lattice data and exhibiting a critical point singularity", *Phys. Rev. C*, vol. 101, no. 3, p. 034901, 2020.

[39] H. J. Drescher, M. Hladik, S. Ostapchenko, T. Pierog, and K. Werner, "Parton-based Gribov–Regge theory", *Phys. Rep.*, vol. 350, no. 2-4, pp. 93–289, 2001.

[40] H. Drescher, F. Liu, S. Ostapchenko, T. Pierog, and K. Werner, "Initial condition for QGP evolution from NEXUS", *Phys. Rev. C*, vol. 65, p. 054902, 2002.

[41] P. Romatschke and U. Romatschke, *Relativistic fluid dynamics in and out of equilibrium and applications to relativistic nuclear collisions*. Cambridge University Press, 2019.

[42] J. Berges, M. P. Heller, A. Mazeliauskas, and R. Venugopalan, "Thermalization in QCD: theoretical approaches, phenomenological applications, and interdisciplinary connections", *B. Am. Phys. Soc.*, 2020.

[43] K. Werner, I. Karpenko, T. Pierog, M. Bleicher, and K. Mikhailov, "Event-by-event simulation of the three-dimensional hydrodynamic evolution from flux tube initial conditions in ultrarelativistic heavy ion collisions", *Phys. Rev. C*, vol. 82, no. 4, p. 044904, 2010.

[44] V. Abramowsky, V. Gribov, and O. Kancheli, "AGK cutting rules", *Sov. J. Nucl. Phys*, vol. 18, no. 308, p. 21, 1974.

[45] Y. B. Ivanov, "Baryon stopping as a probe of deconfinement onset in relativistic heavy-ion collisions", *Phys. Lett. B*, vol. 721, no. 1-3, pp. 123–130, 2013.

[46] E. Fermi, "High energy nuclear events", *Prog. Theor. Phys.*, vol. 5, no. 4, pp. 570–583, 1950.

[47] E. Fermi, "Angular distribution of the pions produced in high energy nuclear collisions", *Phys. Rev.*, vol. 81, no. 5, p. 683, 1951.

[48] L. D. Landau, "On multiple production of particles during collision of fast particles", *Izv. Akad. Nauk. SSSR*, vol. 17, p. 51, 1953.

[49] S. Z. Belen'kji and L. D. Landau, "Hydrodynamic theory of multiple production of particles", *Il Nuovo Cimento*, vol. 3, no. 1, pp. 15–31, 1956.

[50] U. Heinz, "'RHIC serves the perfect fluid' – Hydrodynamic flow of the QGP", tech. rep., 2005.

[51] G. S. Denicol, *Efeitos da viscosidade no escoamento da matéria em processos nucleares relativísticos*. Master's thesis, Universidade Federal do Rio de Janeiro (UFRJ), 2009.

[52] U. H. Gerlach, "Equation of state at supranuclear densities and the existence of a third family of superdense stars", *Phys. Rev.*, vol. 172, no. 5, p. 1325, 1968.

[53] Y. Hama, R. P. Andrade, F. Grassi, O. Socolowski Jr, T. Kodama, B. Tavares, and S. S. Padula, "3D relativistic hydrodynamic computations using lattice-QCD-inspired equations of state", *Nucl. Phys. A*, vol. 774, pp. 169–178, 2006.

[54] Y. Hama, R. Andrade, F. Grassi, O. Socolowski, T. Kodama, B. Tavares, and S. Padula, "Effects of LatticeQCD EoS and continuous emission on some observables", in *AIP Conf. Proc.*, vol. 828, pp. 485–490, AIP, 2006.

[55] S. Ahmad, H. Holopainen, and P. Huovinen, "Dynamical freeze-out criterion in a hydrodynamical description of Au+Au collisions at $\sqrt{s_{NN}} = 200$GeV and Pb+Pb collisions at $\sqrt{s_{NN}} = 2760$GeV", *Phys. Rev. C*, vol. 95, no. 5, p. 054911, 2017.

[56] F. Cooper and G. Frye, "Single-particle distribution in the hydrodynamic and statistical thermodynamic models of multiparticle production", *Phys. Rev. D*, vol. 10, no. 1, p. 186, 1974.

[57] C. Schwarz, D. Oliinychenko, L. Pang, S. Ryu, and H. Petersen, "Different realizations of Cooper-Frye sampling with conservation laws", *J. Phys. G: Nucl. Part.*, vol. 45, no. 1, p. 015001, 2017.

[58] D. M. Dudek, *Efeitos da equação de estado em hidrodinâmica relativística através de alguns observáveis*. PhD thesis, Universidade Estadual Paulista (UNESP), 2014.

[59] R. P. G. de Andrade, *Sobre a evolução hidrodinâmica da matéria nuclear criada em colisões de íons pesados relativísticos-um estudo com condições iniciais flutuantes*. PhD thesis, Universidade de São Paulo (USP), 2011.

[60] F. Grassi, "Particle emission in hydrodynamics: a problem needing a solution", *Brazilian journal of physics*, vol. 35, no. 1, pp. 52–59, 2005.

[61] P. Huovinen and H. Petersen, "Particlization in hybrid models", *Eur. Phys. J. A*, vol. 48, no. 11, p. 171, 2012.

[62] F. G. Gardim, F. Grassi, M. Luzum, and J.-Y. Ollitrault, "Anisotropic flow in event-by-event ideal hydrodynamic simulations of $\sqrt{s_{NN}}$= 200 GeV Au+Au collisions", *Phys. Rev. Lett.*, vol. 109, no. 20, p. 202302, 2012.

[63] M. V. Machado, *Event-by-event Hydrodynamics for LHC*. Master's thesis, Universidade de São Paulo (USP), 2015.

[64] Particle Data Group, "Review of particle physics", *Phys. Rev. D*, vol. 98, p. 030001, Aug 2018.

[65] D. Oliinychenko and H. Petersen, "Deviations of the energy-momentum tensor from equilibrium in the initial state for hydrodynamics from transport approaches", *Phys. Rev. C*, vol. 93, no. 3, p. 034905, 2016.

[66] R. A. Gingold and J. J. Monaghan, "Smoothed particle hydrodynamics: Theory and application to non-spherical stars", *Mon. Not. Roy. Astron. Soc.*, vol. 181, p. 375, 1977.

[67] L. B. Lucy, "A numerical approach to the testing of the fission hypothesis", *Astron. J.*, vol. 82, p. 1013, 1977.

[68] C. Aguiar, T. Kodama, T. Osada, and Y. Hama, "Smoothed particle hydrodynamics for relativistic heavy ion collisions", *J. Phys. G: Nucl. Part.*, vol. 27, no. 1, p. 75, 2001.

[69] E. Parzen, "On estimation of a probability density function and mode", *Ann. Math. Stat.*, vol. 33, no. 3, p. 1065, 1962.

[70] Wikimedia Commons, the free media repository. file:SPHInterpolationColors.svg [Online; accessed 15-January-2021].

[71] H.-T. Elze, Y. Hama, T. Kodama, M. Makler, and J. Rafelski, "Variational principle for relativistic fluid dynamics", *J. Phys. G: Nucl. Part.*, vol. 25, no. 9, p. 1935, 1999.

[72] J. R. Dormand, *Numerical methods for differential equations: a computational approach*, vol. 3. CRC press, 1996.

[73] J. Adams *et al.*, "Measurements of identified particles at intermediate transverse momentum in the STAR experiment from Au+Au collisions at $\sqrt{s_{NN}} = 200$GeV", tech. rep., 2006.

[74] L. Adamczyk *et al.*, "Beam energy dependence of moments of the net-charge multiplicity distributions in Au+Au collisions at RHIC", *Phys. Rev. Lett.*, vol. 113, no. 9, p. 092301, 2014.

[75] A. Pandav, D. Mallick, and B. Mohanty, "Effect of limited statistics on higher order cumulants measurement in heavy-ion collision experiments", *Nucl. Phys. A*, vol. 991, p. 121608, 2019.

[76] M. Aggarwal *et al.*, "Higher moments of net proton multiplicity distributions at RHIC", *Phys. Rev. Lett.*, vol. 105, no. 2, p. 022302, 2010.

[77] B. Abelev *et al.*, "Systematic measurements of identified particle spectra in pp, d+Au, and Au+Au collisions at the STAR detector", *Phys. Rev. C*, vol. 79, no. 3, p. 034909, 2009.

[78] B. Efron and R. J. Tibshirani, *Monographs on Statistics and Applied Probability*. Chapman & Hall/CRC, 1994.

[79] J. Kapusta, B. Müller, and M. Stephanov, "Relativistic theory of hydrodynamic fluctuations with applications to heavy-ion collisions", *Phys. Rev. C*, vol. 85, no. 5, p. 054906, 2012.

[80] K. Murase and T. Hirano, "Relativistic fluctuating hydrodynamics with memory functions and colored noises", *arXiv preprint arXiv:1304.3243*, 2013.

[81] C. Young, J. Kapusta, C. Gale, S. Jeon, and B. Schenke, "Thermally fluctuating second-order viscous hydrodynamics and heavy-ion collisions", *Phys. Rev. C*, vol. 91, no. 4, p. 044901, 2015.

[82] L. Adamczyk *et al.*, "Energy dependence of moments of net-proton multiplicity distributions at rhic", *Phys. Rev. Lett.*, vol. 112, no. 3, p. 032302, 2014.

[83] K. Reygers, "Glauber Monte-Carlo calculation for Au+ Au collisions at $\sqrt{s_{NN}} = 200gev$", *PHENIX internal Analysis Note*, 2003.

[84] M. L. Miller, K. Reygers, S. J. Sanders, and P. Steinberg, "Glauber modeling in high-energy nuclear collisions", *Annu. Rev. Nucl. Part. Sci.*, vol. 57, pp. 205–243, 2007.

[85] P. Ishida. Personal communication, December 2020.

[86] I. Bearden *et al.*, "Pseudorapidity distributions of charged particles from Au+Au collisions at the maximum RHIC energy, $\sqrt{s_{NN}} = 200$ GeV", *Phys. Rev. Lett.*, vol. 88, no. 20, p. 202301, 2002.

[87] J. Adams *et al.*, "Transverse-momentum and collision-energy dependence of high-p_t hadron suppression in Au+Au collisions at ultrarelativistic energies", *Phys. Rev. Lett.*, vol. 91, no. 17, p. 172302, 2003.

[88] I. Bearden *et al.*, "Nuclear stopping in Au+Au collisions at $\sqrt{s_{NN}} = 200$ GeV", *Phys. Rev. Lett.*, vol. 93, no. 10, p. 102301, 2004.

[89] G. S. Denicol, C. Gale, S. Jeon, A. Monnai, B. Schenke, and C. Shen, "Net-baryon diffusion in fluid-dynamic simulations of relativistic heavy-ion collisions", *Phys. Rev. C*, vol. 98, no. 3, p. 034916, 2018.

[90] L. Du, U. Heinz, and G. Vujanovic, "Hybrid model with dynamical sources for heavy-ion collisions at BES energies", *Nucl. Phys. A*, vol. 982, pp. 407–410, 2019.

[91] The STAR public webpage with data tables: `https://drupal.star.bnl.gov/STAR/files/starpublications/205/data.html`.

[92] L.-N. Gao, F.-H. Liu, Y. Sun, Z. Sun, and R. A. Lacey, "Excitation functions of parameters extracted from three-source (net-) proton rapidity distributions in Au-Au and Pb-Pb collisions over an energy range from AGS to RHIC", *Eur. Phys. J. A*, vol. 53, no. 3, pp. 1–11, 2017.

[93] E. Schnedermann, J. Sollfrank, and U. Heinz, "Thermal phenomenology of hadrons from 200A GeV S+S collisions", *Phys. Rev. C*, vol. 48, no. 5, p. 2462, 1993.

[94] P. Braun-Munzinger, K. Redlich, and J. Stachel, "Particle production in heavy ion collisions", in *Quark–Gluon Plasma 3*, pp. 491–599, World Scientific, 2004.

[95] G. D. Yen, M. I. Gorenstein, W. Greiner, and S. N. Yang, "Excluded volume hadron gas model for particle number ratios in A+A collisions", *Phys. Rev. C*, vol. 56, no. 4, p. 2210, 1997.

[96] L. D. Landau and E. M. Lifshitz, *Course of theoretical physics: fluid mechanics*. Elsevier, 2013.